NEW PLASMON-EXCITON COUPLING INDUCED OPTICAL PHENOMENA IN MONOLAYERED WS_2 SANDWICHED IN A METAL-FILM-COUPLED NANOCAVITY

LIU JIN

MPhil

The Hong Kong Polytechnic University

2019

The Hong Kong Polytechnic University
Department of Applied Physics

New Plasmon-exciton Coupling Induced Optical Phenomena in monolayered WS_2 Sandwiched in a Metal-film-coupled Nanocavity

LIU JIN

A thesis submitted in partial fulfillment of the requirements for the degree of Master of Philosophy

July 2018

CERTIFICATE OF ORIGINALITY

I hereby declare that this thesis is my own work and that, to the best of my knowledge and belief, it reproduces no material previously published or written, nor material that has been accepted for the award of any other degree or diploma, except where due acknowledgement has been made in the text.

_____ (Signed)

LIU Jin (Name of student)

Abstract

Recently, the study of two-dimensional (2D) materials such as graphene and transition metal dichalcogenides (TMDs) has become one of the most interesting research topics due to their unique electrical and optical properties and their great potential for applications in optoelectronics devices. For example, the bandgap of Tungsten disulphide (WS_2) is typically layer-sensitive. It exhibits an indirect band gap in multilayer form while it changes to a direct bang gap in monolayer form. Such flexible photoelectric characteristics allow a wide range of applications of 2D-WS_2 in transistors, photodetectors and electroluminescent devices. However, the optical and vibrational properties of WS_2 strongly depend on their fabrication methods, such as mechanical exfoliation (ME) and chemical vapour deposition (CVD). It is generally believed that ME prepared samples have higher quality than CVD prepared samples, but a comprehensive comparison between the two methods remains to be explored.

The thesis provides a comparative study on the vibrational and optical properties of CVD-grown and ME-prepared monolayered and few-layered WS_2 by using several optical spectroscopic techniques. Dramatic differences are observed in the Raman response, differential reflectance, photoluminescence (PL) efficiency and second-harmonic generation (SHG), which are all suggested to be related to the structural defects. Surprisingly, it is found that the PL of the CVD-grown WS_2 bilayer shows almost no linear polarization dependence and exhibits no significant difference under the two different circularly polarized excitations, while these polarization

dependences are much stronger for the ME-prepared WS_2 bilayer. However, it can be observed that the CVD-grown WS_2 bilayer has an unprecedentedly stronger SHG signal than the signal of both the CVD-grown and ME-prepared monolayers. The results not only point out the importance of improving current CVD-based growth methods to achieve large-area TMD materials with optical, electrical and structural properties comparable to small flakes prepared by ME methods, but also demonstrate the promise of using CVD-grown bilayer TMDs in general for nonlinear optoelectronics applications.

In addition, the properties of the bright and dark excitons in monolayer WS_2 have also been explored. Two respective states of the splitting conduction band, which are caused by the broken inversion symmetry and strong spin-orbital coupling, give rise to the bright and dark excitons by coupling with holes in the valence band. Normally, due to the selection rules, the radiative relaxation of dark excitons are generally forbidden, which means that the dark excitons are optically dark. Because the dark excitons have a longer lifetime, they can have potential applications in quantum communication and play an important role in fundamental research, such as Bose-Einstein condensation. To induce radiative emission of dark excitons in atomically thin TMDs, different approaches have been demonstrated in recent low temperature photoluminescence (PL) studies. However, the control of dark excitons and the observation of dark excitons at room temperature can be the remaining challenges. The second part of this thesis presents a way to observe the dark excitons under room temperature by metal-film-coupled nanocavities through

polarization-resolved PL measurements. Firstly, the mechanically exfoliated WS_2 monolayers are sandwiched into the metal-film-coupled nanocavities. Then, the polarization-resolved PL measurements are conducted to detect the dark excitons. A blue shift of the peak from the PL spectra can be observed when the detected polarization angle changes from 0 to 90 degree. To further examine the origin of this phenomenon, a fitting model is established to predict and fit all the experimental PL spectra. The fits are satisfactory in different dimensions and different characteristics of bright and dark excitons, such as peak width, peak intensity and polarization dependence can be directly observed. This part provides a simple method to observe the optical effects of dark exciton in room temperature. By controlling the detected polarization angle, the proportion of the bright and dark excitons can be changed. Compared with other works about brightening of dark excitons, this work has advantages in the simplification of the experimental condition (i.e. room temperature, simple set-up) and abundance of extracted information.

List of Publications and Conference Presentations

Journal publications based on this thesis work:

(# equally contributed, * corresponding author)

1. **J. Liu**, T. W. Lo, J. H. Sun, C. T. Yip, C. H. Lam, D. Y. Lei*, "A comprehensive comparison study on the vibrational and optical properties of CVD-grown and mechanically exfoliated few-layered WS_2", Journal of Materials Chemistry C 5, 11239-11245 (2017)

2. **Jin Liu** #, Meng Qiu#, Tsz Wing Lo#, Qiang Zhang, Chi Hang Lam, Wei Jin and Dang yuan Lei*, "Probing dark excitons in atomically thin TMDs through plasmonic gap modes in metal film-coupled nanostructures by polarization resolved Photoluminescence spectroscopy", under preparation.

Journal publications during my MPhil study but not included in this thesis:

3. F. F. Qin, C. X. Xu, D. Y. Lei, S. Q. Li, **J. Liu**, Q. X. Zhu, Q. N. Cui, D. T. You, A. G. Manohari, Z. Zhu, F. Chen, "Interfacial control of ZnO microrod for whispering gallery mode lasing", accepted by ACS Photonics (2018)

4. Guoqiang Liu, Lina Chen, **Jin Liu**, Meng Qiu, Zhuang Xie, Jian Chang, Yaokang Zhang, Yu Yang, Peng Li, Qi Gan, Jian Shang, Dangyuan Lei and Zijian Zheng*, "Scanning Nanowelding Lithography for Rewritable One-step Patterning of sub-50 nm High-aspect-ratio Metal Nanostructures", accepted by Advanced Materials (2018).

Conference presentations

1. **J. Liu**, T. W. Lo, J. H. Sun, C. H. Lam, D. Y. Lei, "A comprehensive comparison study of CVD-grown and mechanically exfoliated few-layered WS_2: vibrational and optical properties", Poster presentation, best poster awards 2nd runner-up, PSHK 17th, Hong Kong, 2017.

2. **J. Liu**, T. W. Lo, J. H. Sun, C. T. Yip, C. H. Lam, D. Y. Lei, "A comprehensive comparison study on the vibrational and optical properties of CVD-grown and mechanically exfoliated few-layered WS_2", Poster presentation, XIV International Conference on Nanostructured Materials, Hong Kong, 2018.

Acknowledgments

There are many people I want to thank for their help during my two years' MPhil study.

Firstly, I would like to express my sincere gratitude to my chief supervisor Dr. LAM Chi-Hang for providing an opportunity for me to pursue my MPhil study here. Without his professional guidance and unconditional supports, the completion of this thesis would not be possible, and I could not finish my study. I also thank my co-supervisor Dr. LEI Dangyuan for his valuable guidance. Without his supports, I could not finish my project. All the works finished in this thesis benefit substantially from the assistance of my collaborators. Therefore, I want to express my thanks to Mr. LO Tsz Wing (Billy) and Dr. QIU Meng for their supports.

Furthermore, I want to say thank you to my groupmates and former groupmates, Dr. SUN Jianhui, Dr. BAO Zhiyong, Dr. LI Guangcan, Dr. DUAN Jinglai, Mr. LI Siqi, Mr. MENG Yongjun, Mr. LIU Danjun, Mr. HO Willis for their generous help. I will never forget all the happy times I have enjoyed together.

Finally, I am deeply and forever indebted to my parents for their love, support, and encouragement throughout my entire life.

Table of Contents

Chapter 1 Introduction and Literature Review

1.1 Introduction of Transition Metal Dichalcognides (TMDs)

Atomically thin two-dimensional (2D) materials have recently attracted extraordinary research interest.[1–3] Transition metal dichalcognides (TMDs), as a typical type of 2D materials, have attracted increasing attention due to their good optical and electronic properties which can be applied to optoelectronic devices.[4,5] The chemical composition of these TMDs is MX_2, where M represents the transition metal elements (e.g. Tungsten (W), Molybdenum (Mo)) and X the chalcogens (e.g. oxygen (O), sulphur (S), selenium (Se), tellurium (Te)).[6] The properties of these materials are different from each other. For example, the bulk form of NbS_2, $NbSe_2$, TaS_2 et. al are metals while materials such as MoS_2, WS_2, $MoSe_2$, WSe_2 are semiconductors.[7–9] In contrast to the most well-known 2D material – graphene, which have a zero-energy band gap, monolayer TMDs are direct band gap semiconductors.[10] With this property, many 2D TMDs are holding huge potential to become good candidates for making ultra-small transistors which are more efficient than traditional silicon based transistors.[11] Besides, 2D TMDs can be used as an active layer in making light emitting diodes and photo detectors for their good optical properties.[12,13]

Atomically thin TMDs have similar structures and unique optical and electrical properties. Here I will introduce the structure and some typical characteristics about TMDs and focus on one of the representative materials of TMDs.

1.1.1 TMD Crystal Structure

Bulk TMDs can be taken as the stacking of monolayer TMDs by weak van der Waals like forces and the in-plane forces are provided by the strong covalent bonds between different atoms. Bulk TMDs have been studied for a long time [3,14] and the main crystal structures of them can be divided into three types, i.e. 1T, 2H and 3R, which have been demonstrated in figure 1.1.

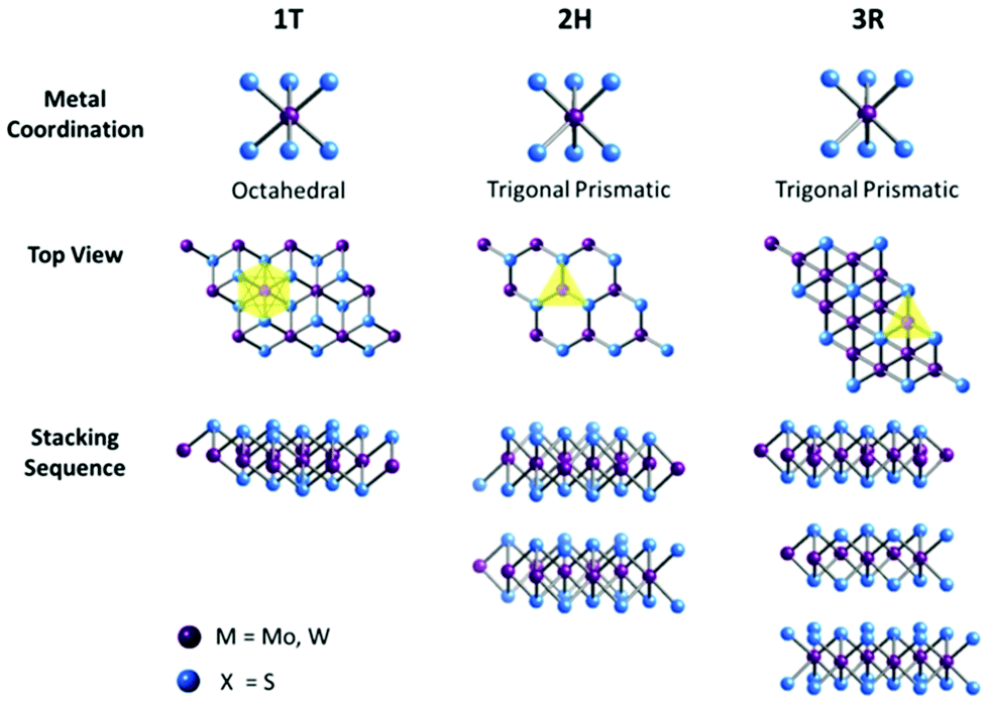

Figure 1.1 Different metallic crystalline structures of TMDs unit cells. The atomic metal coordination can be either octahedral or trigonal prismatic. Based on different coordinations and different stacking sequences, the crystal structure

of the TMDs will be different, i.e. the Octahedral coordination forms the 1T structure while the trigonal prismatic coordination with different stacking sequences can give rise to the 2H and 3R structures .[15]

1T crystal structure is not quite stable comparing with the 2H and 3R structures for the TMDs this thesis has focused on (especially WS_2). For the 2H and 3R structures, each monolayer has an identical structure but differences arise from the stacking order of the monolayers in the crystal structures. Each monolayer consists of three atomic planes, which can be taken as the fundamental building blocks of the bulk crystal. The top and bottom planes consist of chalcogen atoms while the middle plane consists of metal atoms. All three atomic layers form a 2D hexagonal lattice with one metal atom and two chalcogen atoms per sublattice site. The 2H bulk crystal structure has the hexagonal symmetry, which have two layers in the repeated unit and the neighboring monolayers can be taken as the rotation of 180° degrees of each other. Therefore, the 2H crystal structure is a central-symmetric structure when the layer number is even. However, different from the 2H structure, the 3R crystal structure has the rhombohedral symmetry, which have three layers in the repeated unit and the neighboring monolayers can be taken as the translation of each other without any rotations. Previous work about the first-principles calculations of TMDs show that those multilayer crystals in 2H structures are more stable than those in 3R structures.[16] Therefore, the TMD thin films

prepared by mechanical exfoliation from the natural bulk crystals are normally in 2H crystal structures. Even though the 3R crystal structure is possible, it is not frequently observed in existing works.[17,18]

1.1.2 Raman scattering

Raman scattering is one of the most common methods to observe the lattice vibrational properties of a crystal. When an incident photon from the laser interacting with the atoms in the crystals and then scattered into the environments in all directions, the energy of the scattered photon and of the incident photon can be either the same or different. For the process in which the energy of the photon does not change, we call it Rayleigh scattering and the process in which the energy of photon changed after scattering is called Raman scattering.[19] Depending on whether the energy of the photon increases or not after the scattering process, the photon can experience either an energy loss (stokes shift) or an energy gain (anti-stokes shift). Such kind of process in which only one photon is involved is called first-order Raman process. On the contrary, if two photons are involved, the process will be called a second-order Raman process. Since the intensity of a second-order Raman scattering is normally much weaker than the intensity of a first-order Raman scattering, I only focus on the first-order Raman scattering process in this work.

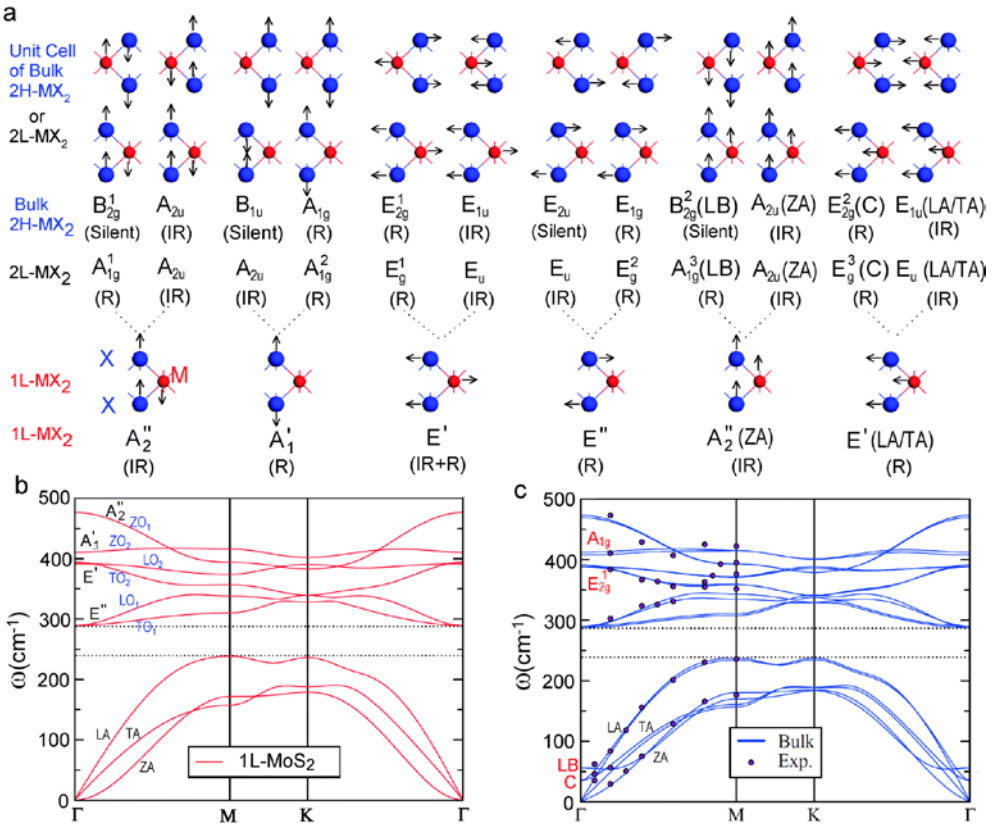

Figure 1.2 (a) Different symmetry types and normal displacements of each type of optical vibration modes for bulk MX_2, bilayer MX_2 and monolayer MX_2. R, IR and silent represent Raman-active, infrared-active and both R and IR inactive modes, respectively. The dotted lines show that each mode in monolayer MX_2 can be split into two modes in both bilayer MX_2 and bulk MX_2, either vibrating in-phase or out-of-phase. (b, c) Calculated phonon dispersion curves of (b) monolayer MX_2 and (c) bulk MX_2 for MoS_2, respectively. The points in (c) are measured experimental data.[20–22]

Raman scattering mode is closely related to lattice vibrations. Lattice vibrations can be classified based on the symmetry groups in the crystals.[23] As previously mentioned, the unit cell of bulk TMDs consists of two X–M–X units,

which means there are six atoms in a single unit cell. This crystal structure suggests that there are 18 phonon modes (3 acoustic and 15 optical modes). Bulk TMDs has the D_{6h} point group symmetry, in which the lattice vibrations of TMDs at the Γ point in the Brillouin zone can be expressed as: $\Gamma = A_{1g} + 2A_{2u} + 2B_{2g} + B_{1u} + E_{1g} + 2E_{1u} + 2E_{2g} + E_{2u}$, where A_{2u} and E_{1u} represent the acoustic modes, A_{1g}, E_{1g} and E_{2g} are Raman active modes, A_{2u} and E_{1u} are infrared (IR) active modes, and B_{2g}, B_{1u} and E_{2u} are related to the optically inactive modes (silent).[24,25] When the layer number decreases, the symmetry in multi-layer TMDs will reduce. For monolayer TMDs, the unit cell consists of only three atoms and thus the vibrational modes can be simplified. The vibrations of different vibrational modes are shown in figure 1.2.

Raman scattering measurements is a good method to identify the thickness of TMDs, especially WS_2. As the layer number increases, the intensity ratio of the different two typical Raman active modes (E_{2g}^1 and A_{1g}) changes and the wave number difference between these two modes also changes. Details are shown in figure 1.3 and table 1.1.

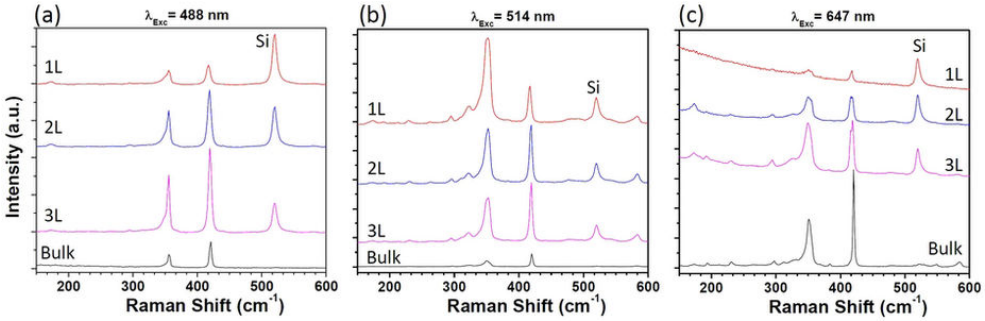

Figure 1.3 Raman spectra collected from thin WS_2 films with different thicknesses (1L, 2L 3L and bulk) using three different excitation wavelengths: (a)

488 nm, (b) 514.5 nm and (c) 647 nm.[26]

λ_{Exc}	Photon Modes	1-layer	2-layers	3-layers	Bulk
488nm	$A_{1g}(\Gamma)(cm^{-1})$	417.5	418.9	419.5	420.2
	$E^1_{2g}(\Gamma)(cm^{-1})$	355.9	355.3	355	355.8
	$I_{E^1_{2g}}/I_{A_{1g}}(Intensity\ ratio)$	0.78	0.62	0.59	0.53
514.5nm	$A_{1g}(\Gamma)(cm^{-1})$	417.2	418.4	419	420.1
	$E^1_{2g}(\Gamma)(cm^{-1})$	355.2	355	354.4	355.3
	$I_{E^1_{2g}}/I_{A_{1g}}(Intensity\ ratio)$	2.2	1.01	0.72	0.47
643nm	$A_{1g}(\Gamma)(cm^{-1})$	417.2	418.7	419.2	420.5
	$E^1_{2g}(\Gamma)(cm^{-1})$	355.3	354.2	354	354.7
	$I_{E^1_{2g}}/I_{A_{1g}}(Intensity\ ratio)$	0.5	0.8	0.8	0.4

Table 1.1 Summary of the wave numbers (cm^{-1}) for the main Raman modes together with the intensity ratio for the intensity of peaks, as a dependence of the

layer number and the excitation wavelength.

The E_{2g}^1 mode is related to the vibration within the same layer and the A_{1g} mode is related to the vibration involving different layers. As the layer number increases, the intensity of A_{1g} mode will increase while the intensity of E_{2g}^1 mode almost has no change. Besides, the wave number difference between the E_{2g}^1 mode and A_{1g} mode increases as the layer number increases. Therefore, the Raman scattering spectra can be a rough reference for the thickness of thin WS_2 films.

1.1.3 Electronic structures of TMDs

As previously mentioned, the electronic structures of 2D TMDs are largely depending on their crystal structures. When the thickness reduces to monolayer, a significant change is the transformation of indirect band gap in the bulk form to the direct band gap in the monolayered form. Theoretical simulations using density function theory (DFT) calculations firstly examined the existence of direct band gap in monolayer WSe_2 and MoS_2 at the corners of the hexagonal Brillouin zone (i.e. the $\pm$K points).[27,28] In addition, the first experimental evidence for the existence of direct band gap is achieved by PL measurements. The result shows the PL intensity from a monolayer exhibit a significant (orders of magnitude) increase compared to their multilayer or bulk forms.[29,30]

To simplify the theoretical model, only critical points will be considered in

analysis of the electronic structures of TMDs. Critical points mean the extreme or saddle points of the energy bands. They play important roles in the determination of the optical and transport phenomena in TMDs. For monolayer TMDs, only the active bands (i.e. the top valence band (VB) and the lowest conduction band (CB)) need to be considered. In monolayer TMDs, the conduction band minimum (CBM) and the valence band maximum (VBM) are both located at the corners of the first Brillouin Zone (BZ). The six corners of the BZ belong to two different groups denoted by K and –K points which are inequivalent to each other. Each group has three corners which are equivalent to each other. The details of reciprocal lattice and the first BZ are shown in figure 1.5.[6]

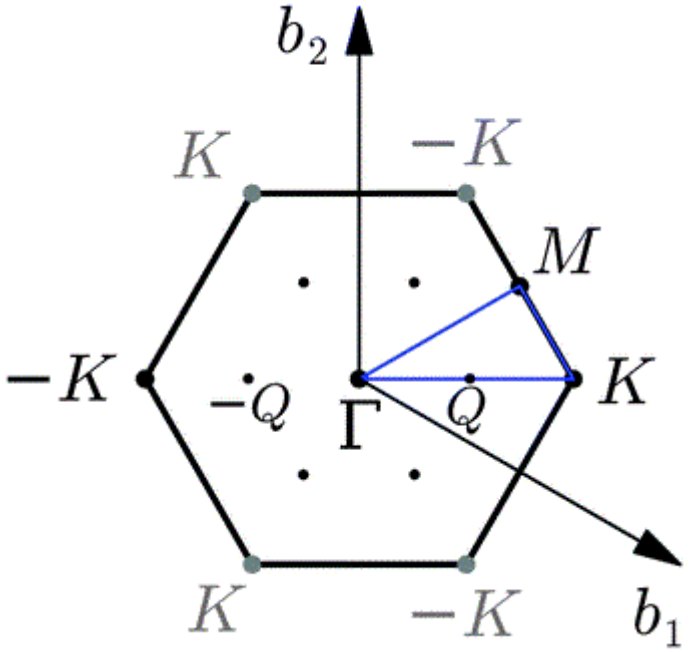

Figure 1.4 The first Brillouin zone. $\mathbf{b}_1$ and $\mathbf{b}_2$ are the reciprocal lattice vectors, respectively.[6]

Generally, the band gap refers to the energy difference between the CBM

and VBM. The band gap can be determined by either transport or optical measurements. However, the energy of band gap determined from these two methods is different. This difference may arise from the existence of excitonic effects in optical process. The band gap determined by transport measurement is commonly taken as the electronic band gap. The electronic band gap characterizes single-particle excitation process. It is defined as the total energy needed to separately tunnel a hole and an electron into the system.[31] Different from the electronic band gap, the optical band gap is defined as the total energy needed to create an exciton. During the optical process, the system absorbs a photon and then creates an electron in the CB together with a hole in the VB. The electron and the hole will bind together by Coulomb interaction and then forms an exciton. It is obvious that the energy difference between the electronic and optical band gap is closely related to the binding energy of the excitons. Therefore, this energy difference could show the strength of the Coulomb interaction.

TMDs	**Optical Band gaps**
MoS_2	1.83, 1.90
WS_2	1.95
$MoSe_2$	1.66
WSe_2	1.64

Table 1.2 Optical band gaps in monolayer TMDs determined by photoluminescence (PL) measurements. The unit of the energy is eV.[6,10]

Optical band gaps of TMD monolayers can be determined by optical measurements, such as PL and reflectance measurements. The results from previous works about optical band gaps in PL measurements are listed in table 1.2. It can be easily found that all four types of TMDs have the optical band gaps in the visible range, which makes them good candidates for applications in semiconductor optics and optoelectronic applications. However, the substrate and dielectric environments could affect the size of the optical band gap by a few percent.[32–36] The band structures of WS_2 from monolayer to quadlayer calculated by DFT calculations is shown in figure 1.5.

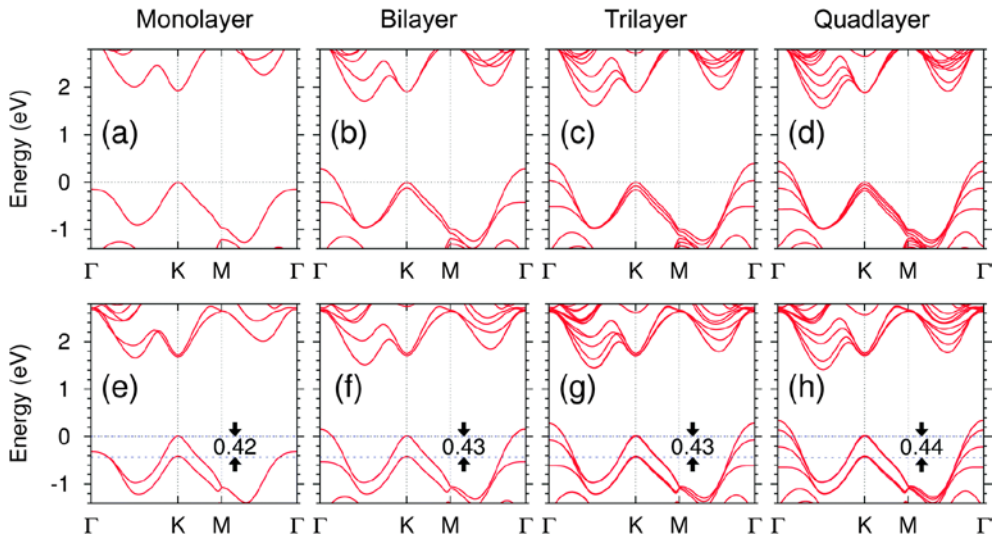

Figure 1.5 Band structures for WS_2 from monolayer to quadlayer without spin-orbital coupling [(a)–(d)] and with spin orbital coupling [(e)–(h)]. The splitting of the valence band at K point arise from spin-orbital coupling which is nearly independent of the number of layers.[6]

1.1.4 Second harmonic generation (SHG)

Second harmonic generation (SHG) is a typical type of second-order nonlinear optical process. Different from two-photon photoluminescence (TPL), the SHG is a process in which two photons with the same frequency interacting with a typical nonlinear material will be "combined" together to generate new photons with twice the original energy, which means the frequency will be doubled and the wavelength will be half of the initial one (Figure 1.6).[37–39] Therefore, SHG can be taken as a special case of sum frequency generation.

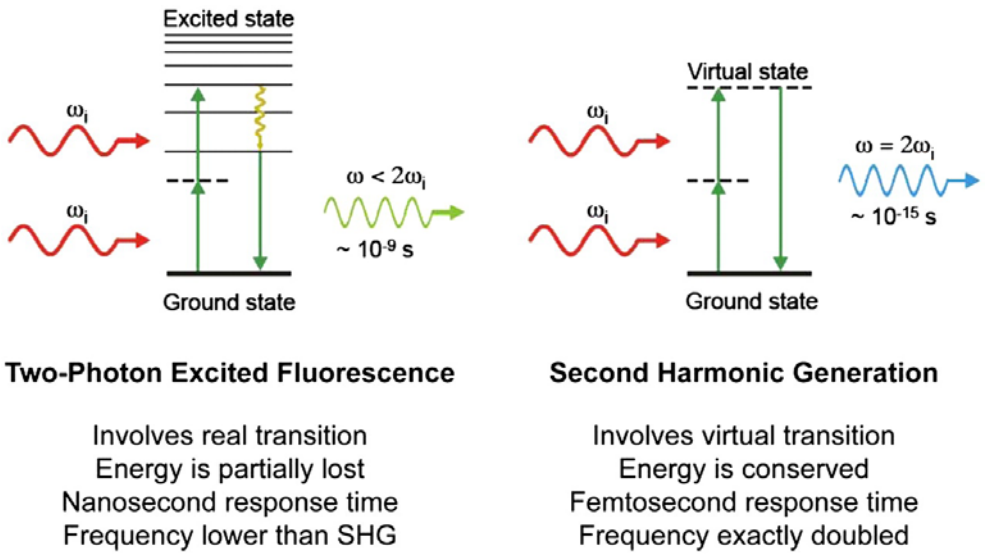

Figure 1.6 Comparison between two typical types of nonlinear optical process: Two-photon excited fluorescence and SHG.[40]

The optical response of the nonlinear materials can be described by expressing the produced polarization P(ω) as a function of the optical field strength E(ω) of the incident light:

$$P(\omega) = \chi^{(1)} \cdot E(\omega) + \chi^{(2)} \cdot E(\omega)^2 + \chi^{(3)} \cdot E(\omega)^3 + \cdots$$

In that function, the coefficient $\chi^{(n)}$ means the *n*th-order susceptibility of the material. For example, $\chi^{(1)}$ corresponding to linear optical process such as absorption or reflection, $\chi^{(2)}$ corresponding to second-order nonlinear optical process such as SHG and $\chi^{(3)}$ corresponding to third-order nonlinear optical process such as third harmonic generation. However, due to the limitation of the optical selection rules, the optical transition of SHG in central-symmetric structure is forbidden. Therefore, materials without inversion symmetry could have SHG response.

Second harmonic generation was first studied by Peter Franken, A. E. Hill, C. W. Peters, and G. Weinreich at the University of Michigan, Ann Arbor, in 1961.[41] Before that time, the SHG study suffered from low concentration and incoherence of the light source. After the invention of laser, which can provide a good coherent light source, this demonstration was made possible. After this phenomenon has been observed, the formulation of SHG, was initially described by N. Bloembergen and P. S. Pershan at Harvard in 1962.[42] The formulation was based on Maxwell's equation and many rules of light in linear and non-linear optics.

Second harmonic generation includes three types, which are named as 0, I and II. In Type 0 SHG, two photons, which have extraordinary polarization with regard to the crystal will be combined together to form a single photon which has twice the frequency and energy of the original one. In Type I SHG, two photons having ordinary polarization with respect to the crystal will be combined together

to form one photon which has twice the frequency and energy of the original one. In Type II SHG, two photons having orthogonal polarizations will be banded together to form one photon which has twice the frequency and energy of the original one. However, for a given crystal orientation, only one type of SHG can exist. And the type is determined by the structure and characteristic of the crystal.

SHG microscopy based on the principles of SHG has a wide range of applications in biological and medical imaging because some endogenic proteins, such as collagen fibrils in connective tissues or the actomyosin lattice of muscle cells, have good structures and characteristics to generate detectable SHG.[43] Therefore, those materials with good SHG response always have potential applications in bio-imaging and bio-medical applications.[44]

1.1.5 Applications of TMDs

Recent studies on thin flakes of 2D-TMDs have shown their unique optical and electronic properties which allowed their potential applications in electronic devices (i.e. atomically thin transistors,[45] vertical tunnelling transistors[46] and vertical field-effect transistors (vFETs)[47] which is the key point for building 3D integrating circuit) and new types of optoelectronic devices (i.e. tunable photovoltaic devices and light emitting devices).[48–52] The 2D-TMDs can exhibit a great number of physical properties and play important roles in metallic, superconducting, semiconducting or charge density wave (CDW) subjects. This part will focus mostly on the applications of 2D-TMDs in semiconductor

devices.

Most of the 2D-TMDs have similar band structures and the most unique feature is the change from indirect band gap in bulk materials to direct band gap in monolayer thin films. This feature was firstly be examined by the PL measurements of atomically thin MoS_2, in which the PL intensity of monolayer films was more than 10^4 times compared with the bulk crystals. This result could be taken as a direct evidence for the transition to a direct band gap semiconductor in monolayer MoS_2.[35,53] In addition, similar results can also be observed in WS_2 and WSe_2.[10] Normally, most of the TMDs have their intrinsic band gap within the range 1–2 eV. Therefore, the 2D-TMDs can break the major limitations of graphene for electronic applications, which are the lack of band gap (graphene has a zero band gap), unsatisfied on/off current ratio and the properties of current saturation. For example, using the MoS_2 flakes prepared by mechanical exfoliation method as the semiconductor channels, the current on/off ratio of the field-effect transistor (FET) can be enlarged by more than eight orders of magnitude.[45,54]

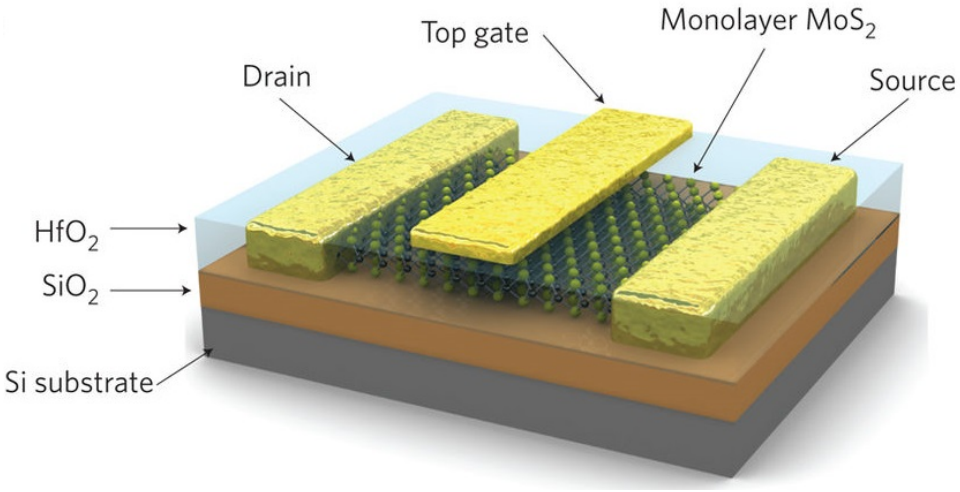

Figure 1.7 3D schematic view of the transistor using MoS2 as the semiconducting layer.[45]

Apart from the transistor using one single type of TMD monolayer as the semiconducting layer, those using TMD heterostructures also attracts many research interests. In general, TMD heterostructures represents for the vertical stacking of several TMD monolayers through Van der Waals forces. The heterostructures formed by atomically thin 2D TMDs can allow rapid modification of the electronic band structures thus forming atomically thin heterojunctions.[55] With so many types of 2D TMDs available, a great deal of different complicated heterostructures can be built and created by nearly randomly assembling several 2D-TMD monolayers into heterostructures or superlattices due to the breaking of the limitations in lattice matching. These heterostructures have unique properties, such as sharp interfaced, almost no inter-diffusion of atoms and manually controlled components. The creation of these TMD heterostructures can provide a new method for manufacturing the electronic and optical properties at the atomic level. Therefore, it can provide potential applications in atomically thin electronic and optoelectronic devices. For example, recent studies about the heterostructure formed by MoS_2 and WSe_2 monolayers have demonstrated unique properties of this heterostructure, which are the spatially direct absorption and indirect emission.[56] The PL intensity of this indirect emission is quite strong, which indicates a strong interlayer coupling of the charge carriers. In addition, they also found this coupling strength can be

tuned by changing the thickness of the inserting dielectric layer between WSe_2 and MoS_2. Therefore, those findings make it possible for tuning optoelectronic properties of the heterostructures thus provide the potential applications in tunable optoelectronic devices.

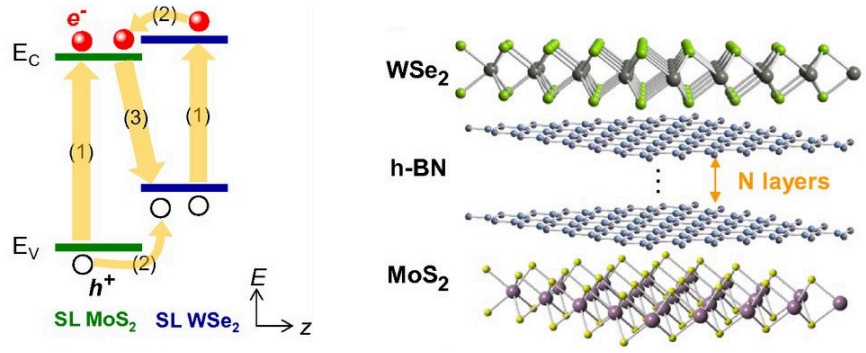

Figure 1.8 Schematic diagrams of (left) the band structures of WSe_2/MoS_2 hetetrostructure under photo-excitation (right) the heterostructure consists of WSe_2 and MoS_2 monolayers with the h-BN spacer as the dielectric layer. The thickness of the dielectric layer can be controlled by changing the layer number of the h-BN spacer.[57]

1.2 Introduction of plasmons and plasmonic effects

Plasmonics is a favorable field of science and technology which aims to explore the interaction between light and matter. With the surface plasmon resonance (SPR), a great deal of properties and functions can be established.[58] The SPR can be taken as a kind of oscillation of charge carriers induced by the electromagnetic wave at the interface between materials with positive and negative permittivities, especially for dielectric or metal materials. Depending on

whether the oscillation propagate along a planar surface or confined on a localized structure, the surface plasmon polaritons (SPPs) or localized surface plasmon reasonances (LSPRs) can be achieved. Once excited, both types of SPR can confine the incident electromagnetic field into an ultra-small space, which leads to a strong enhancement of the local field. Based on those unique properties, the plasmonic materials can have wide range of applications in photonics, chemistry, energy and even life science.[59–66]

1.2.1 Optical diffraction limit and strong light-matter interaction

It is generally agreed that light-matter interaction can be one of the most important physical process in fundamental science. From atomic transition to photo-synthesis, most of the processes are closely related to the light-matter interactions. By controlling this interaction, many different kinds of advanced technologies including global telecommunication and signal detection in atomic scale can be enabled. However, the main limitation of light-matter interaction at subwavelength scale is the so called optical diffraction limit. This limit is demonstrated and examined by the weakness of the light transmitting through a single ultra-small hole.[67,68] The theory about optical diffraction limit was firstly established by German physicist Ernst Abbe in 1873. According to his theory, two objects with their distance smaller than $\lambda/2n$ could not be resolved better whatever attempts tried to improve the resolution of the microscope by optical lens fabrication, where λ is the wavelength of the incident light and n is the

refractive index. Therefore, the smallest size of the optical which can be observed by optical microscope can be written as $a = \frac{1.22\lambda}{NA}$ where NA is the numerical aperture of the objective in microscope. This limit strongly affects the ability to observe the optical phenomena in the ultra-small scale.

Generally, strong light-matter interactions are key points in optical applications, including surface-enhanced Raman scattering (SERS), photoluminescence and nonlinear optics.[37,69,70] However, most of those processes suffer from the ultra-low transmission and conversion efficiency. Therefore, to achieve a strong emission intensity, the excitation light should have high optical intensity. With the invention of laser, this problem has been partially solved. Laser can provide a coherent light source with strong optical power and critically enhanced optical density by focusing the light into the spot size close to the theoretical value of diffraction limit. However, the limitation of optical diffraction limit is still left unsolved. Recent study about the physical phenomena which are related to the surface plasmon resonances (SPRs) have opened a new way to break this limitation.

1.2.2 Surface plasmon polaritons and localized surface plasmons

Surface plasmon is a kind of the electron oscillation which takes place at the interface between the metal and dielectric.[71] It has attracted huge research interests recently and it can take place at any type of metal-dielectric interface which can provide many potential applications. There are two main types of the

surface plasmon modes, which are named as surface plasmon polaritons (SPPs) and localized surface plasmons (LSPs), respectively (figure 1.9).

SPP occurs on the large area of planar interfaces and the transition direction of the SPP wave is parallel to the metal-dielectric interface. At optical frequencies, plasmons can couple with a photon to create another quasiparticle which is called plasmon polariton. Wavelength of SPPs is always smaller than wavelength of the plane waves in the corresponding dielectric material and the wavelength of SPPs can be modified by choosing certain type of metal and dielectric. Therefore, the SPPs can break the limitation of diffraction.

In comparison, LSPs are sustained by the metallic nanoparticles. LSP refers to the result by restricting the surface plasmon into a nanoparticle with the size close or smaller to the wavelength of the light which is used to excite the plasmon. In addition, those metallic nanoparticles can act as optical antennas, which can trap the incident light into a small space with subwavelength scale. Through this process, the LSPs can be used to break the optical diffraction limit. Therefore, with those properties, LSPs can permit various kinds of applications in SERS[72–74], photo-thermal extraction in tumor therapy[75–77] and some novel types of high efficient photovoltaic devices[78–80].

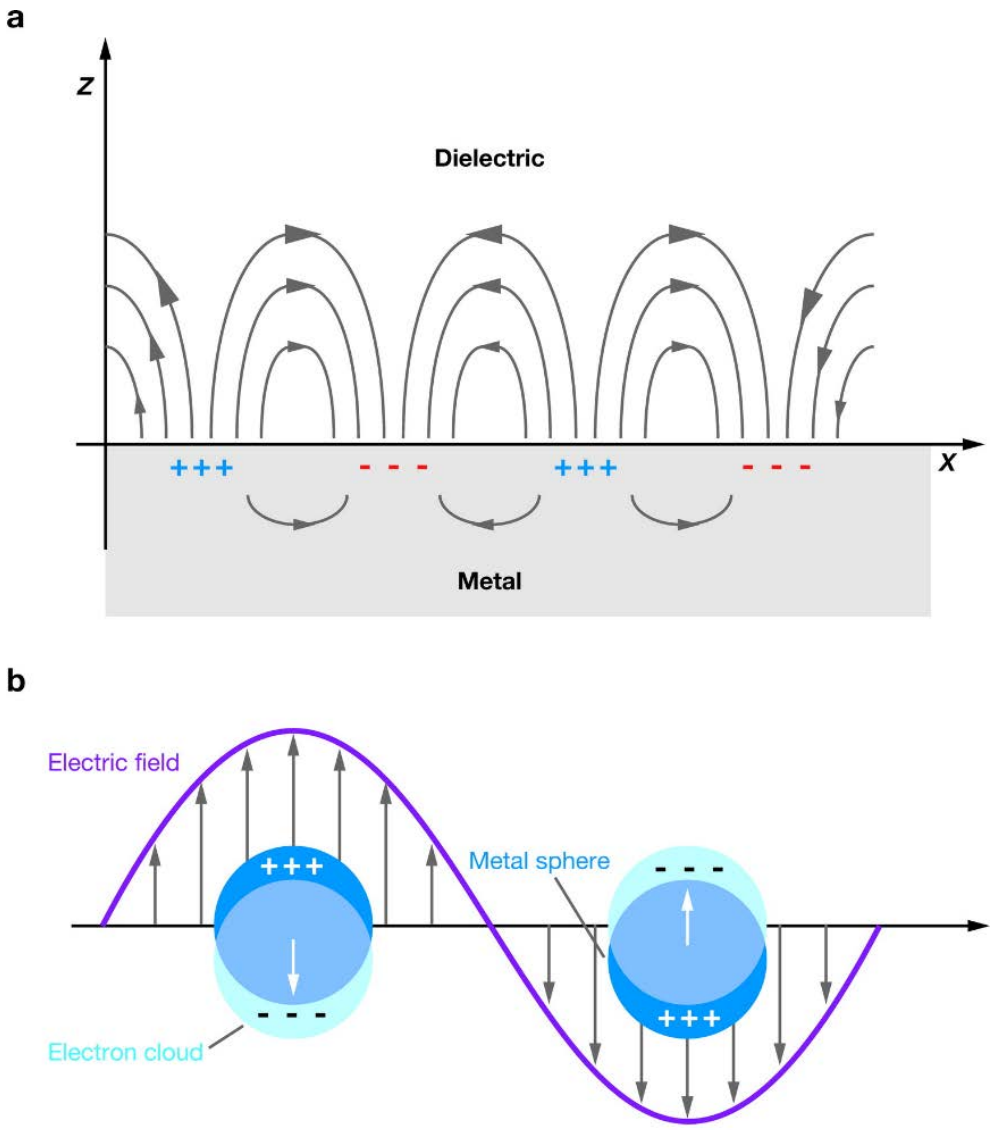

Figure 1.9 Schematic diagrams demonstrating (a) a surface plasmon polariton and (b) a localized surface plasmon, respectively.[81]

There are two ways to excite SPPs, which are through electrons and photons, respectively. There is almost no limitation for the excitation process by electrons, but for the process by photons, the limitation is strong. To excite an SPP, the incident photon should have the same frequency and momentum along the surface with the SPP. However, a photon in the free-space always has less

momentum than an SPP. To break this limitation, one of the methods is to replace the air by another medium with a higher dielectric index, which is shown in figure 1.10.[82]

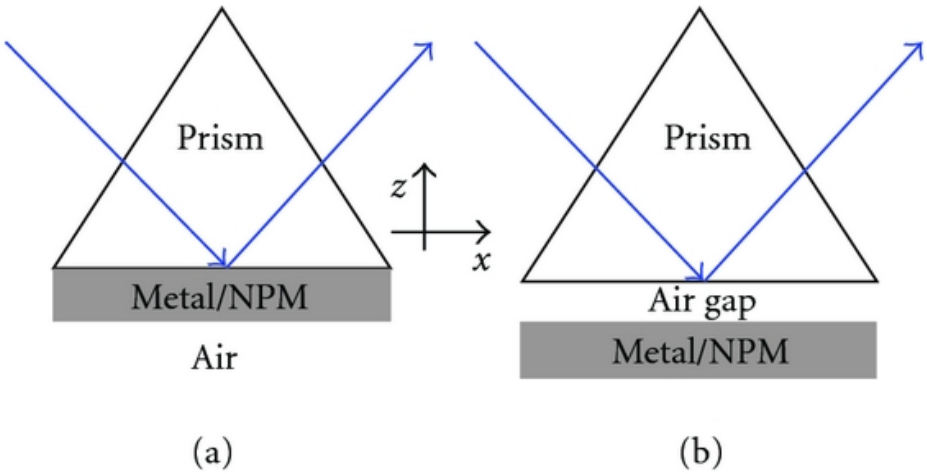

Figure 1.10 Schematic of Kretschmann (a) and Otto (b) configurations. Those two configurations provide the solutions to the limitations of the excitation of SPPs by photons.[83]

Different from the excitation of SPP, the excitation of LSP is quite simple. It can be excited directly by the plane wave because the total contribution of LSPs can be treat as a dipole, which could highly interact with propagating wave. Since the LSP is confined within the nanoparticle, when the scale of the oscillation amplitude matches the size of the nanoparticle, a strong resonance will take place. That kind of resonance is called localized surface plasmon resonance (LSPR). LSPRs existed in metallic nanoparticles have attracted many research interests in basic science study and applications. Most of the applications are based on the unique properties of LSPRs, such as the resistance

to corrosion or oxidation in air and the strong electromagnetic resonances at visible and near-infrared range. By these LSPRs, the optical properties of these metallic nanoparticles can be determined. When the incident photons to illuminate the nanoparticles are at the resonant wavelength, the plasmonic nanostructures will exhibit much stronger light-matter interactions. A strong electromagnetic field will be confined around the nanoparticles when the resonant oscillation occurs, which could be used for the enhancement of light-matter interactions. Besides, the nanoparticles will exhibit different colors which related to the plasmonic resonances when they are illuminated by the white light, which provide the potential applications in color printing and sensors. Since the LSPRs are closely related to the scale, geometry, composite and the surrounding environment of the nanoparticles, their optical properties can be modified easily by controlling the synthesis or fabrication process (Figure 1.11).

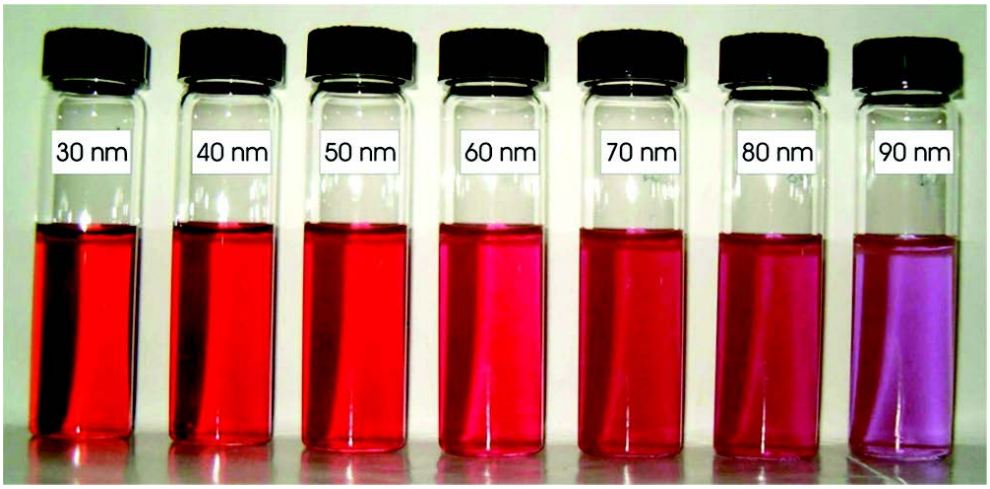

Figure 1.11 Photos of gold nanoparticles showing different colors. The labeled scales are the diameters of the certain gold nanoparticles.[84]

1.2.3 Plasmonic coupling and metal-film-coupled nanocavity

Previous parts have introduced the LSPRs sustained in single metallic nanoparticles. However, to achieve more suitable and desired properties, researchers use more than one nanoparticle to form plasmon coupling which can create the certain type of plasmon resonance through different methods, such as generating sub-radiant and super-radiant modes or creating plasmonic Fano resonances.[85,86] Therefore, many new types of metallic nanostructures, including nanoparticle clusters or oligomers can be synthesized by directly plotting more than one nanoparticles into a system which can be either symmetric or non-symmetric (Figure 1.12).[87]

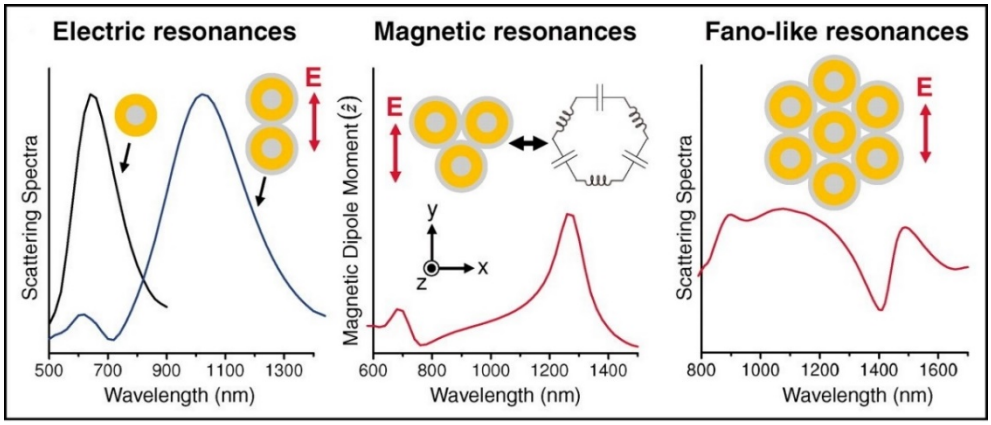

Figure 1.12 Simulated spectra of nanoshell clusters assembled by more than one nanoparticles. Different types of clusters can support tunable electric, magnetic, or fano-like resonances. Most of the electric dipole resonances can be observed in plasmonic nanostructures such as monomer (one single nanoparticle) or dimer (two nanoparticles). On the contrary, the magnetic resonances always exist in "ring" shaped nanostructures, such as packed trimer (three nanoparticles packed

as a closed ring). In addition, Fano-like resonances can be found in more complicated nanostructures, such as heptamers.[88]

Normally, one or more near-field hot spots can be observed at the gap regions between neighbor nanoparticles. These hot spots arise from the strong electromagnetic interactions between the individual nanoparticles in the plasmon coupling systems. With these unique properties, the plasmon coupling systems could have potential applications in both SERS and PL spectroscopy.[89–91] In addition, the coupling system without centrosymmetric could also provide a platform for second harmonic generation (SHG) due to the breaking of the selection rules.[92,93] The resonance and enhancement of the coupling system are very sensitive to the size of the gaps. Therefore, by changing the size and structure of nanoparticles, the plasmon resonances of these systems can be tuned, thus provide a possible solution for modification of the line-width and line-shape of the resonance.[94,95]

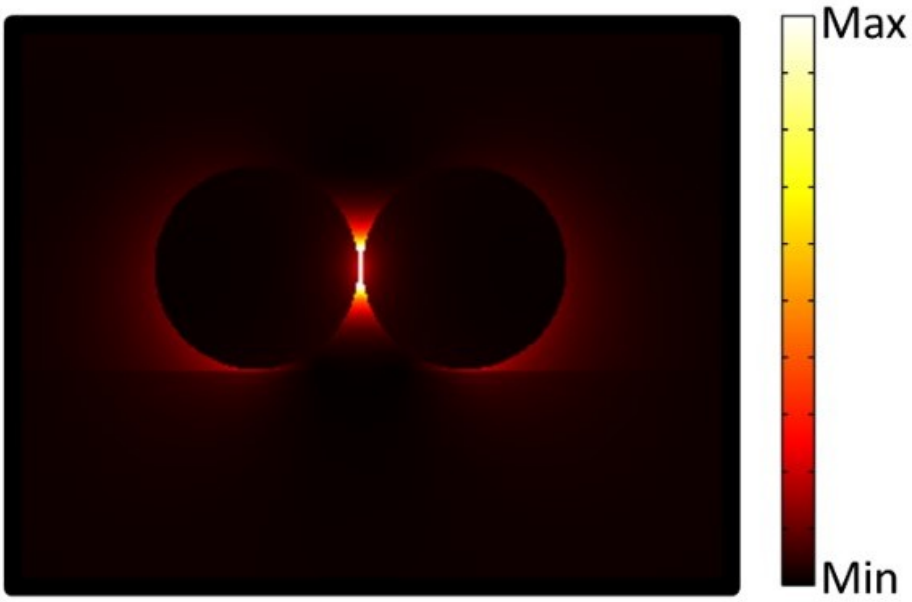

Figure 1.13 Simulation of the field intensity distribution of dimer consists of metallic nanoparticles (diameter: 100nm) at the plasmon resonance (wavelength: 650nm).

Nowadays, the most common synthesis methods for the plasmonic nanostructures are the lithographic method or the simple distribution of the nanoparticles in a plane substrate. However, these two methods both have limitations. The lithographic method suffers from the restriction of the resolution of the equipment which limits the size of the achieved gap region (>10nm). Although the latter method can achieve an ultra-small gap distance, tuning the optical response by controlling the gap distances between different nanoparticles is almost impossible. In addition, due to the difficulty of the in-plane arrangement, adding the monolayer molecules or 2D materials into these

nanoscale gap cavities seems to be impossible for these nanostructures. Therefore, the metal-film-coupled plasmonic nanostructures can be taken as a good candidate to break these limitations sinceand these nanostructures also have received many research interests in the past decades.[96–101]

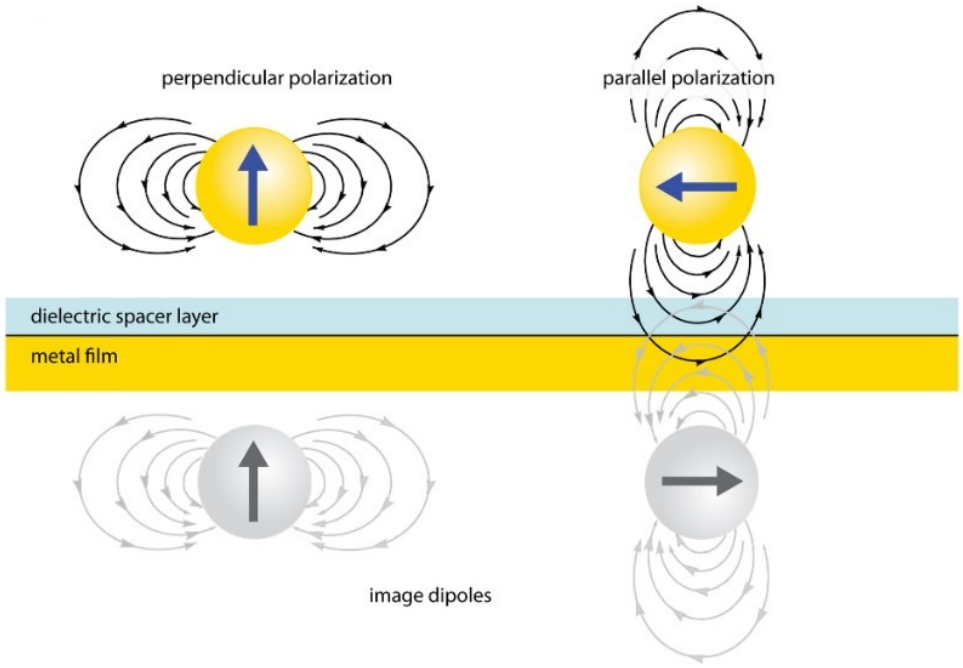

Figure 1.14 Schematics of the electromagnetic interaction between the metallic nanoparticle and the metal film. In this figure, the dipole-image model has been applied to simulate the optical response of the metal-film-coupled system by the electrostatic approximation. Therefore, the optical properties of the metal-film-coupled system equivalent to that of a metal nanoparticle dimer in the vertical orientation.[102]

Due to the development of the technologies in metal film deposition and fabrication of dielectric spacers, the gap distance between the particle and the

film can be easily controlled.[103,104] By tuning the gap distance, the optical properties of these nanostructures can be modified (Figure 1.15).[102] In addition, the gap distance can also be reduced down to the sub-nanometer scale, which provide the potential applications in nonlocal effect and quantum mechanics.[105,106] Moreover, the achieved ultra-small nanocavities can provide a good platform for adding various kinds of active monolayer molecules or 2D materials.[107] Therefore, the formed nanostructures could achieve a series of breakthroughs in studies of the added monolayer molecules, such as subwavelength plasmonic lasers, huge spontaneous emission enhancement and even realization of strong coupling between single molecule and at room temperature.[108–112]

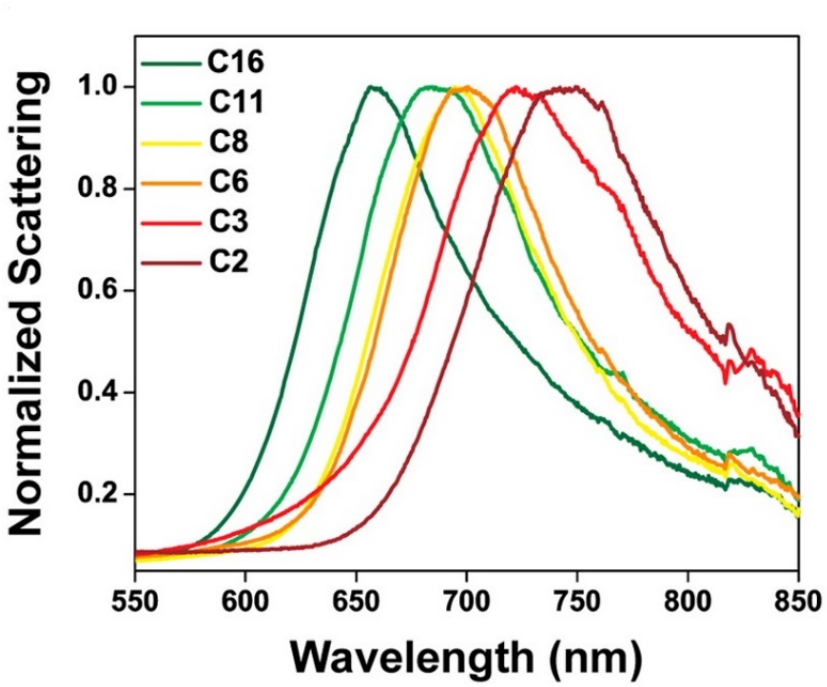

Figure 1.15 Normalized dark-field scattering spectra of single Au nanoparticles on Au film with different thicknesses of the spacers. The resonance peak

experiences a blue shift as thickness of the spacer increases.[104]

1.3 Introduction of excitons

This part will summarize the main properties of the excitons in TMD monolayers and their roles in optical response. In addition, the formation process of excitons will be demonstrated and excitonic effects in light-matter interactions will also be discussed.

1.3.1 Coulomb-bound electron-hole pairs and neutral excitons

When promoting an electron from the saturated valence band to the empty conduction band, an empty electron state will be left in the valence band. However, such a kind of multi-body system is too difficult to be analyzed. To simply this system, the description of the system can be regarded as a two-particle system in which the negatively charged electron in the conduction band will interact with a positively charged electron hole in the valence band. Therefore, to discuss the excitonic effects, the only matter that needs to be considered is the Coulomb interactions between the electron and hole pairs.

The consequences of the Coulomb electron-hole interaction can be separated into the direct and exchange contributions, both of which can be further separated into long-range and short-range coupling. The long-range coupling represents for the Coulomb interactions happens at the distances between the particles are larger than the bond lengths between atoms. On the

contrary, the short-range coupling occurs when the overlap of the electron and hole wave functions are at the same scale with the lattice constants ($a_0 \approx 0.33$nm for 2D-WSe_2), especially for the range of one or several unit cells.[113]

The direct Coulomb interactions play the important roles in the properties of the materials since they can determine the nature of the electronic excitations in materials. For example, the schematic demonstration of the optical absorption in an ideal 2D semiconductor is shown in figure 1.16. The presence of the strong Coulomb interactions results in the formation of the exciton resonances. In addition, the optical band gap is defined from this process, which is the lowest-energy excitonic feature in the optical absorption (the ground state of the exciton).

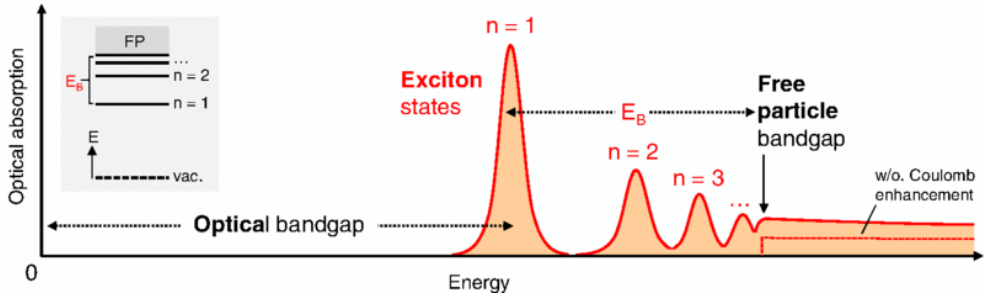

Figure 1.16 Schematic demonstration of the optical absorption in an ideal 2D semiconductor. This figure includes the series of bright exciton transitions below the renormalized quasiparticle band gap.[114]

In comparison to the direct contributions of Coulomb interactions, the exchange contributions are closely related to the Pauli exclusion principle. Based

on this principle, the wave function of the multi-electron system in which one carrier is promoted to the conduction band should have the different spin orientation of the particles. Therefore, the energy of the exciton depends on reciprocal orientation of electron and hole spins. Similarly, the energy of the exciton in TMD monolayers should depend on the quasiparticle valley states. As previously mentioned, the exchange contributions also have long-range and short-range parts. The long-range exchange interaction is related to the electrodynamic nature, which can be taken as the result of the interaction of an exciton with the induced electromagnetic field in the process of virtual electron-hole recombination.[115] For TMD monolayers, the long-range exchange part mainly determine the spin-valley depolarization of the excitons.[114] Different from the long-range part, at short range, the exchange interaction caused by Pauli exclusion will depend on the spin and valley states of the particles. Therefore, for monolayer TMDs, it causes the energy separation between the optically bright and dark excitons.[114]

Coulomb interaction type		Effects
Direct		**Exciton binding energy**
		Neutral excitons: around 500 meV
		Charged excitons, biexcitons: around 50 meV
		Quasiparticle band gap
		Self-energy: around 500 meV
Exchange		**Exciton fine structure**
	Long-range	Neutral exciton spin or valley depolarization
		~1–10 meV

Coulomb interaction type		Effects
	Short-range	Splitting of dark and bright excitons
		~10s of meV

Table 1.2 The effects of different types of electron-hole Coulomb interactions on optical and polarization properties of excitons in TMD monolayers.[114]

1.3.2 Dark and bright excitons

Normally, excitons exhibit optically bright when the incident photons are on resonance.[116,117] On the contrary, for a more complex process such as nonresonant photon excitation or electric injection, more than one exciton states can achieve. For optically bright exciton, the interaction process is radiative. If the optical transition for the exciton is nonradiative, or in other words, spin forbidden, this kind of exciton is called dark exciton.

In TMD monolayers, exciton-photon coupling is closely related to chiral optical selection rules. For normal incident photon, the direct interband transitions at the $K^{\pm}$ points of the Brillouin zone allow the incident photon with $\sigma^{\pm}$ circular polarization, respectively.[118] For the interband transitions, the spin and valley states of the electrons keep unchanged and the electron and hole pairs arise from the same unit cell. Therefore, the exciton states in which the electron and hole states have the same spins are bright and the ones with different spins are dark. The schematic demonstration of the bright and dark transitions which are related to the respective exciton states is shown in figure 1.17. For TMDs, these rules can be applied to A-exciton series. In addition, these rules can also be

applied to B-exciton series since the corresponding spins have the opposite signs.[119]

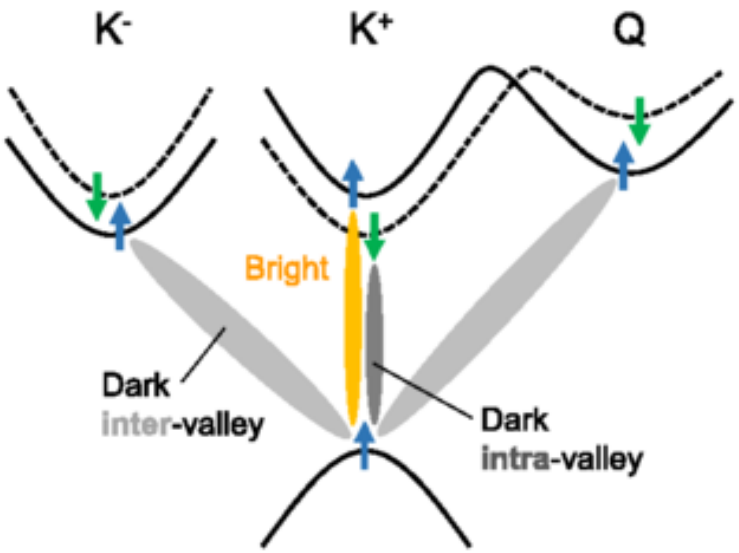

Figure 1.17 A schematic summary of the optically bright and dark (allowed and forbidden) electronic transitions for respectively bright and dark exciton states.[120]

For neutral 1s excitons, the energy differences between the bright and dark excitons is determined by both the previous mentioned short-range Coulomb-exchange interaction and the sign and amplitude of the spin splitting in the conduction band. For W-based TMDs (i.e. WS_2, WSe_2), the spin orientations of the electron in the lower conduction band and upper valence band are opposite. However, in Mo-based TMDs (i.e. MoS_2, $MoSe_2$), the electrons have the same spin orientations. Therefore, the energy of the dark excitons are lower than neutral bright excitons in WS_2 (figure 1.18).

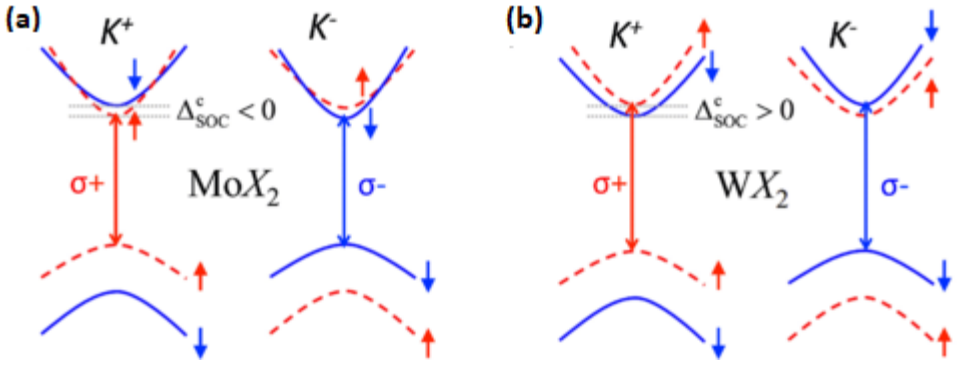

Figure 1.18 Schematic demonstration of the band structures and interband transitions of MoX_2 (a) and WX_2 (b) monolayers.[114]

1.4 Scope and Outline of the Thesis

This thesis consists of five chapters.

The current Chapter introduces the basic knowledge of 2D materials and surface plasmons. In addition, the properties of excitons and differences between bright and dark excitons will also be mentioned in this chapter.

Chapter 2 is about the experimental parts. The synthesis and fabrication methods of the samples will be demonstrated. Besides, the various techniques and instruments for the characterization of the 2D materials and plasmonic nanoparticles will also be introduced.

Chapter 3 is about the comprehensive comparison study of the vibrational and optical properties of thin WS_2 films prepared by both chemical vapor deposition (CVD) and mechanical exfoliation (ME) methods. The results show that the CVD-grown samples have more defects than ME-prepared samples and these defects mainly affect the optical properties of WS_2, especially the excitonic

effects and polarization dependence. However, the unexpected strong SHG response observed from CVD-grown WS_2 bilayers may provide a potential application of CVD-grown WS_2 thin films in nonlinear optoelectronic devices.

Chapter 4 is the main part of this thesis and demonstrates a novel method to detect the dark excitons under room temperature. The WS_2 monolayers are assembled into the nanocavities formed by Au nanospheres and Au films. These metal-film-coupled nanocavities could provide the localized electric field which can enhance radiation of the dark excitons. By applying the linear polarization resolved photoluminescence (PL) measurements, the PL arises from bright and dark excitons can be distinguished and separated. In addition, a fitting model is also established to study the difference of optical properties between bright excitons and dark excitons. The fitting results show good agreement with the experimental results and the dark excitons can be detected by this method under room temperature.

The last chapter, chapter 5, will summarize the main results of this thesis and discuss some possible future work based on this thesis.

Chapter 2 Sample fabrication and instruments for characterizations

The samples used in this thesis consist of two parts: the metal-film-coupled nanoparticle structure and thin WS_2 films. This chapter will introduce the details about synthesis of thin WS_2 films and demonstrate the fabrication methods for metal-film-coupled nanocavities. Furthermore, the optical system involved in this work will also be mentioned.

2.1 Synthesis of thin WS_2 films

2D-TMDs have many kinds of synthesis methods, such as chemical vapor deposition (CVD), physical vapor deposition (PVD), liquid exfoliation and mechanical exfoliation (ME). In this work, only CVD and ME methods are involved.

ME is a popular synthesis method for graphene and TMDs. The key step of this method is using the scotch tape to exfoliate the thin graphene or TMD films from their bulk crystals. After the exfoliation step, the scotch will be directly adhered onto the substrate and the exfoliated thin films will be transferred onto the substrate. Therefore, samples prepared by this method have an obvious disadvantage: the size and thickness of the achieved thin films are almost uncontrollable.

CVD method involves chemical reactions, in which the conditions and

environment of the reaction should be strictly controlled. For CVD-grown thin WS_2 films, the process consists of two steps, which are the reaction step and the deposition step, respectively (figure 2.1). The reaction step involves the main chemical reactions in the whole synthesis process. For example, to grow the thin WS_2 films, tungsten (W) powders or tungsten oxide (WO_3) powders will react with the sulfur (S) powder and form tungsten disulfide (WS_2). After the reaction, the Argon (Ar) or other kinds of gas will flow through the reactor and deposit the WS_2 onto the substrate (i.e. Si wafer). By controlling the conditions (i.e. temperature, pressure) of the reactions and the speed of gas flow, the size and thickness of CVD-grown sample can be roughly controlled. Normally, most of the thin WS_2 films prepared by this method are monolayers.

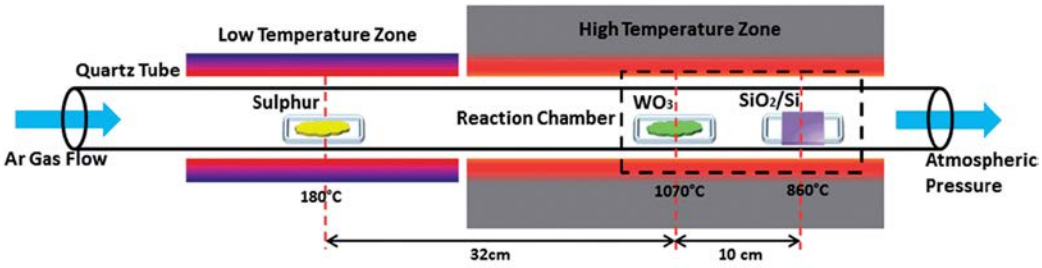

Figure 2.1 Schematic demonstration of the corresponding CVD growing process for WS_2.[121]

2.2 Fabrication of the Metal-film-coupled nanocavity

The fabrication of the metal-film-coupled nanocavity consists of two steps. The first step is about the deposition of the planar Au films and the second is

about how to assemble the Au nanoparticles onto the Au films.

2.2.1 Deposition of Au film

The planar Au film is deposited on a piece of ultraclean silicon wafer with a thermal evaporator (Denton, DV-502). The photo of the equipment and the basic mechanism of the deposition process are shown in figure 2.2. With the electrically heating, the bulk Au in the source container will be melted and vaporized into Au atoms under high temperature and the Au atoms will be deposit onto the surface of the silicon wafer hanging above. After the accumulation, the planar Au film will be achieved.

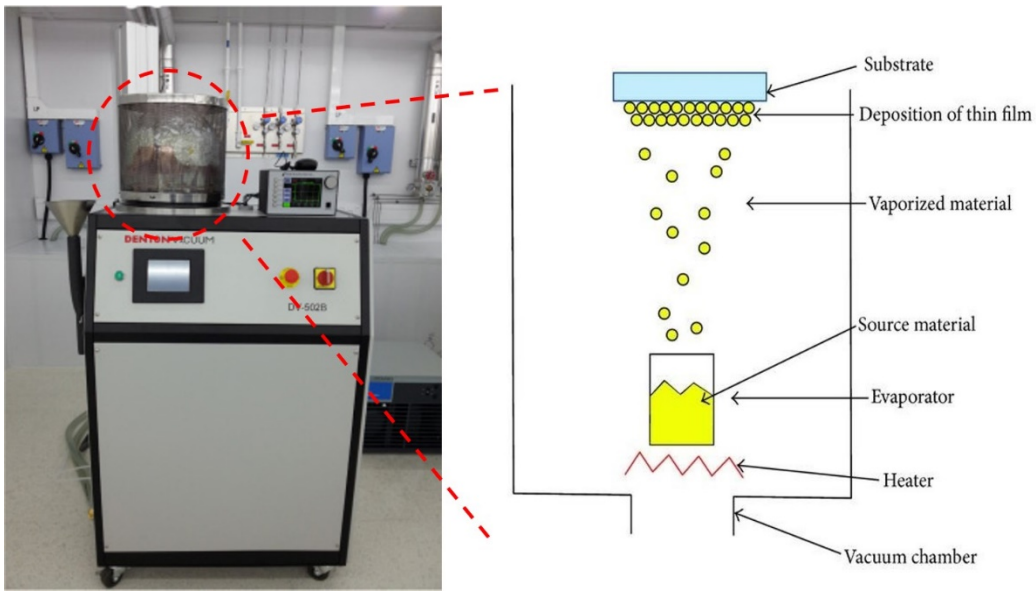

Figure 2.2 Photo of the thermal evaporator (left) and the schematic of the basic mechanism of the thermal evaporating process (right).

There are two main parameters which describe the characteristics of the deposited Au film: thickness of the film and roughness of the surface. The former

one can be controlled by the deposition time and the quantity of the source material. The latter one is mainly affected by the environmental conditions of the evaporating chamber, such as the pressure and vacuum level. In addition, the speed of the deposition can also affect both the thickness and the quality of the Au films.

2.2.2 Au nanoparticles

In this thesis, the Au nanoparticles used are nanospheres, which are purchased as the form of colloidal solution. However, the Au nanoparticles are not stable and easy to form a cluster. Therefore, to avoid those situations, the nanoparticles are all coated with a single layer of Cetyltrimethylammonium Bromide (CTAB) molecules which carry positive charge (figure 2.3).

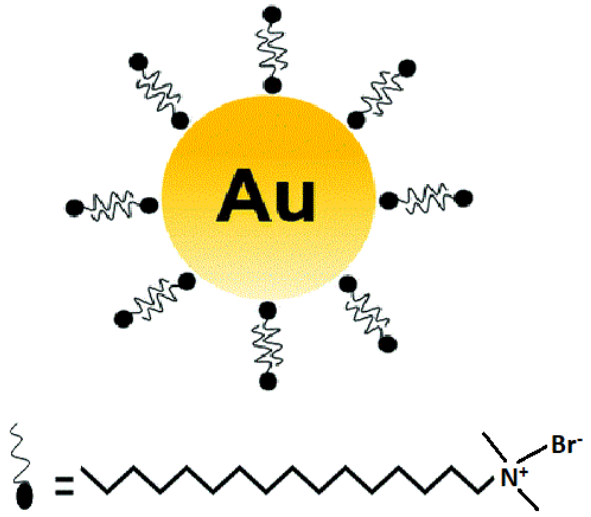

Figure 2.3 Schematic demonstration of the Au nanoparticles coated with CTAB molecules.

To build the metal-film-coupled nanocavity, the Au nanoparticle needs to

be dropped onto the surface of the planar Au film. Before the dropping step, the colloidal solution needs to be centrifuged for 15mins at the speed of 5500 *rpm.* The step aims to remove the excessive CTAB molecules in the solvent. After that, the colloidal solution needs to be diluted by deionized water to lower the concentration level. The last step is to drop the diluted solution onto the surface of the Au film. The surface of the Au film will be dried in air and the nanoparticles will be left.

2.3 Characterization techniques

This part will introduce the instruments for characterizations of the samples in this thesis.

2.3.1 Reflectance and dark-field scattering

The reflectance and dark-field scattering measurements are all carried out on a home-build optical system. The main part of this system is an Olympus BX51 optical microscope installed with a 100 W tungsten quartz halogen lamp as light source. The microscope is equipped with 4 different objective lens, which are 10x, 20x, 50x and 100x, respectively. The 50x and 100x objective lens have both bright-field and dark-field modes while the 10x and 20x lens only have bright-field mode (figure 2.4).

Both the reflectance and dark-field scattering signals are collected by a

TE-cooled CCD. The differential reflectance is calculated as $1-R_{sa}/R_s$, where R_{sa} and R_s are the reflected light intensities from the sample and the substrate, respectively. The dark field scattering intensity is calculated as $(I_p-I_b)/I_{source}$, where I_p and I_b are the dark-field scattering intensity collected from the particle (or sample), background and the I_{source} is the intensity collected from the light source. The photo of the optical system and the schematic illustration of the mechanisms for dark-field scattering measurements are shown in figure 2.5. For linear-polarization-dependent dark-field scattering measurements, the polarizer can be added in both the excitation path and the detection path.

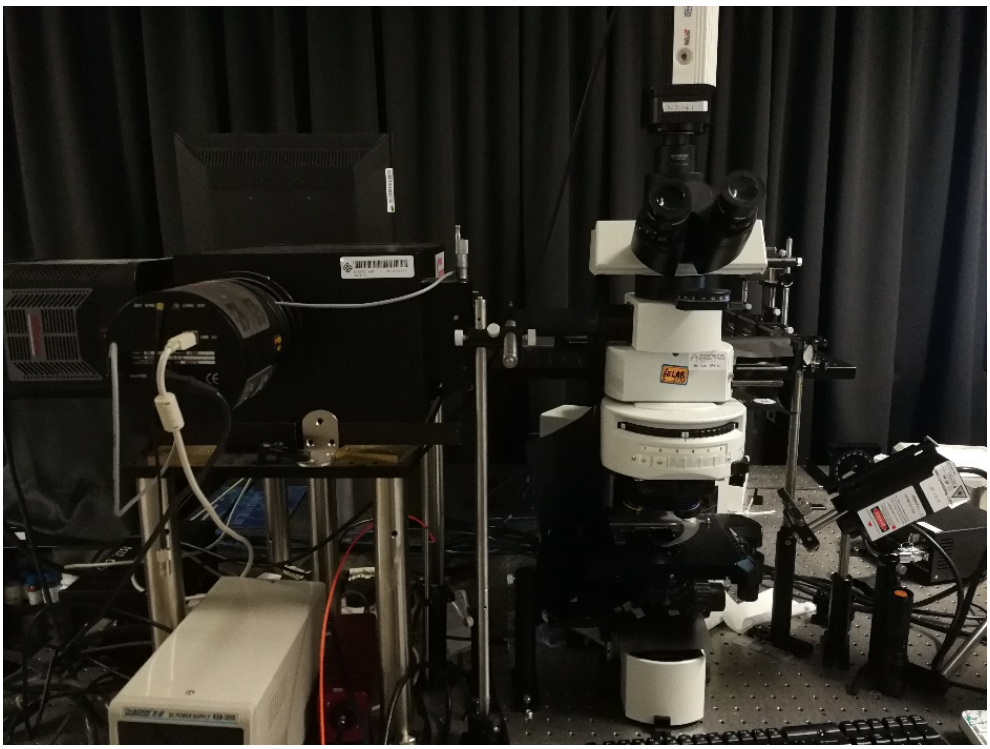

Figure 2.4 Photograph of the home-build optical system.

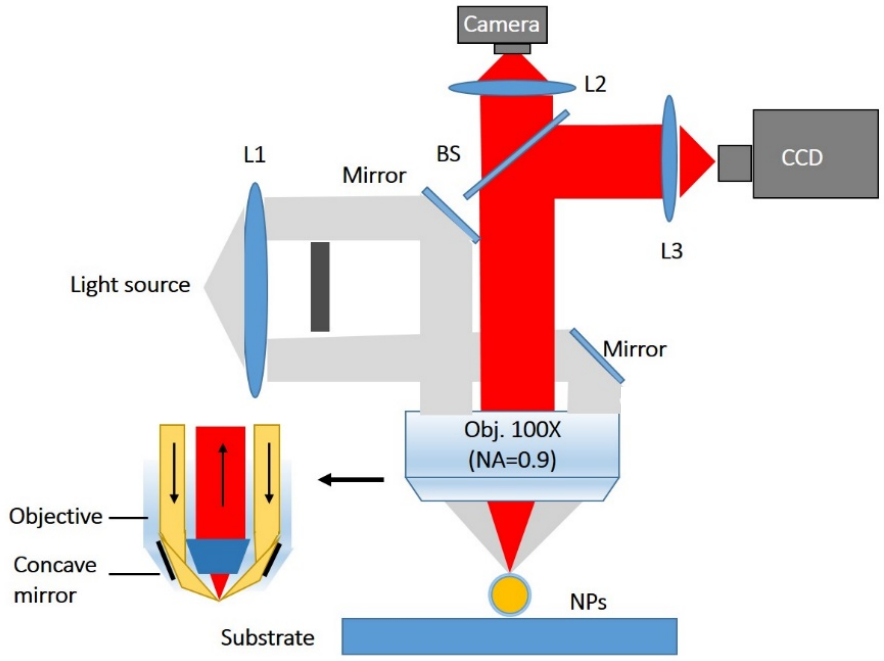

Figure 2.5 Schematic illustration of the mechanisms for dark-field scattering measurements. The BS represents beam splitter and L1, L2 and L3 represent lenses.

2.3.2 Raman scattering and PL

Raman scattering and PL measurements can both be carried out based on a modified confocal microscope system with a spectrometer. There are three systems (Horiba; WiTec; NT-MDT) involved in this thesis and all of them can perform Raman scattering and PL measurements, together with the polarization-resolved PL measurements and mapping tests.

To carry out the linear- and circular-polarization-resolved PL measurements, the excitation and detection paths should be modified. A half-wave plate (HWP) can be added into the excitation path to change the linear-polarized direction of

the incident laser and a polarizer can be added into the detection path to change the linear-polarized direction of the detection. To change the linear-polarized excitation laser into a circular polarized light source, a quarter-wave plate and a polarizer need to be added into excitation path. By adjusting the orientation of the quarter-wave plate to be +45° and -45° with respect to the polarization direction of the excitation laser, the generated laser beam can be either left- or right-handed circularly polarized (figure 2.6).

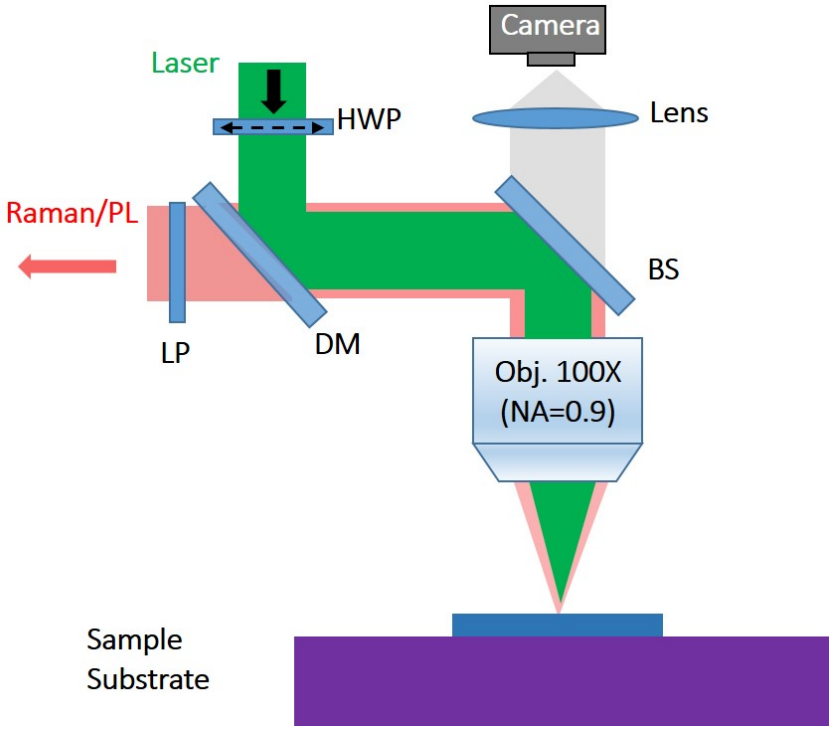

Figure 2.6 Schematic demonstration of the Raman scattering and PL measurements. HWP represents for half-wave plate, LP represents for linear polarizer, DM represents for dichroic mirror and BS represents for beam splitter. For circular-polarization-dependent PL measurements, the quarter-wave plate and the LP will take the position of the HWP. Meanwhile, the same combination (quarter-wave plate and LP) should also take the position of the LP in this figure.

2.3.3 Nonlinear optical spectroscopy

The measurements of nonlinear optics, especially SHG, are carried out on a commercial scanning confocal microscopy system (TCS SP8, Leica) installed with a Ti:sapphire femtosecond laser (Mai Tai HP, Spectra-Physics). Figure 2.7 demonstrate the schematic of the nonlinear optical spectroscopy system. The laser beam will scan on the focal plane which is controlled by the beam scanning resonator. The laser beam is focused by a dry 100x objective lens. To collect second order nonlinear-optical response, especially the SHG signal, the size of the pinholes between L1 and L2 needs to be set as fully opened. Therefore, the intensity of the background noise can be decreased and the signal-to-noise ratio will increase.

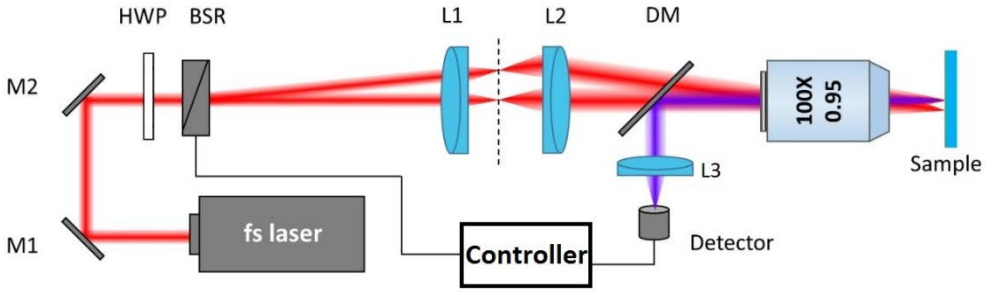

Figure 2.7 Schematic demonstration of the nonlinear optical spectroscopy system. The HWP represents for half-wave-plate, BSR represents for beam scanning resonator, DM represents for dichroic mirror and L1, L2 and L3 represent lens.

2.3.4 Atomic force microscope (AFM)

Atomic force microscope (AFM) can measure the surface characteristics of the sample. For example, by collecting the reflected signals from the AFM tips, the thickness of the sample can be observed. The AFM measurements in this thesis are carried out on a scanning probe microscope (Asylum MFP-3D infinity) with the help of a conductive tip (Si-based). This system can detect the magnetic field and electric field on the surface of the sample. Besides, it can also characterize the piezoelectric properties of a ferroelectric sample. Figure 2.8 demonstrate the schematic of the mechanisms for AFM.

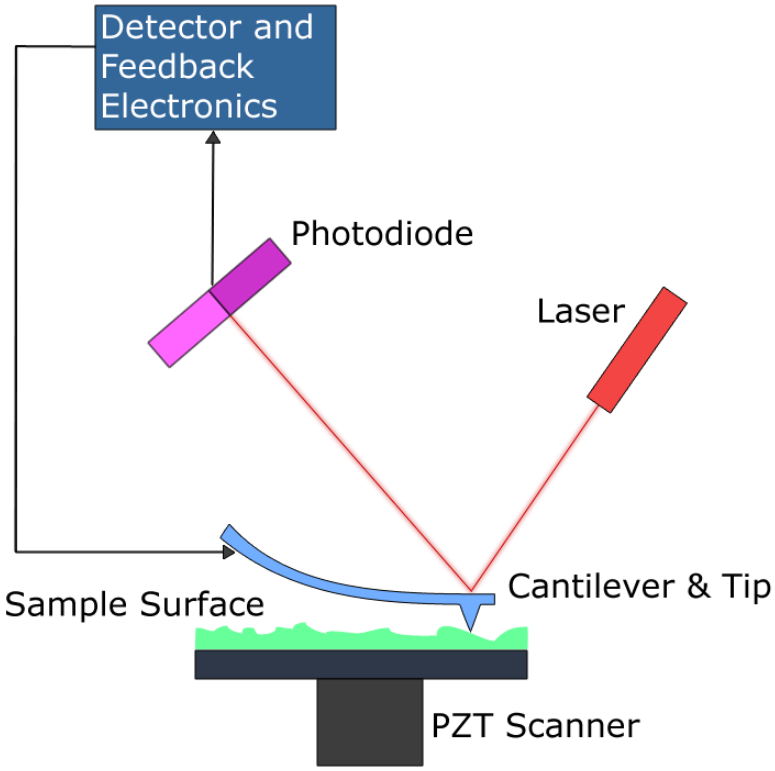

Figure 2.8 Schematic demonstration of the mechanisms for AFM.

Chapter 3 A comprehensive comparison study of CVD-grown and mechanically exfoliated few-layered WS_2: vibrational and optical properties

As a typical TMD material, WS_2 transits from indirect to direct bandgap when the thickness is reduced to monolayer, allowing for potential applications in transistors, photodetectors and electroluminescent devices. However, the optical and vibrational properties of WS_2 strongly depend on their fabrication methods, such as ME and CVD. This chapter will provide a comprehensive comparative study on the vibrational and optical properties of CVD-grown and ME-prepared thin WS_2 films by using several different optical spectroscopic techniques. Intense differences in their Raman response, differential reflectance, PL efficiency and SHG can be observed, which are all possibly related to the structural defects. In addition, the PL of the CVD-grown WS_2 bilayer is almost unpolarised-dependent and exhibits almost no significant difference in the two circularly polarized excitations, while these polarization dependences are much stronger for a ME-prepared bilayer sample. However, the CVD-grown WS_2 bilayer exhibits an unexpected stronger SHG signal than the both the ME-prepared and CVD-grown monolayer. The results not only point out the importance of improving current CVD-based growth methods to achieve large-area TMDs with optical, electrical and structural properties comparable to

small flakes prepared by ME methods, but also demonstrate the promise of using CVD-grown bilayer TMDs in general for nonlinear optoelectronics applications.

3.1 Introduction

Atomically-thin TMDs have become an important class of 2D semiconductors and attracted increasing interests due to their unique optical and electronic properties which are intensely different from their bulk crystals.[4,5,122] Similar to graphene, bulk WS_2 crystallizes in a layered structure which consists of groups of S-W-S branches.[24,25] In contrast to the most well-known 2D material – graphene, which has a zero-energy band gap, monolayer WS_2 has a direct band gap and the energy of the band gap is around 1.95eV, making its PL peak wavelength located in the visible range.[10] Therefore, monolayer WS_2 can be used as an active layer in making light emitting diodes (LEDs),[12] switchable transistors and photo detectors.[4,5,13]

In general, WS_2 samples prepared by CVD methods suffer from low quality, size inhomogeneity and structural defects, which are possibly caused by the unavoidable drawbacks associated with the fabrication procedure.[123–125] Large-area CVD growth of thin WS_2 layers has not yet been realized and the size of the CVD-grown sample is usually quite unsatisfied. In particular, structural defects, such as sulphur vacancies, anti-site defects and dislocations, could exist in CVD-grown WS_2 films.[126,127] These defects can cause localized states in the bandgap, leading to hopping transport behaviour which results in a large decrease

in the carrier mobility[125] and thus significant changes in the linear and nonlinear optical properties such as Raman, PL and second-harmonic generation (SHG). In contrast, WS_2 flakes prepared by mechanical exfoliation (ME) show less amount of defects comparing with CVD-grown samples.[26,128] For example, Ayse et. al found that the Raman intensity ratio of CVD-grown WS_2 films I(E_{2g}^1)/I(A_{1g}) has no obvious dependence on layer number.[26] However, the same ratio of ME-prepared WS_2 exhibits a significant decrease when the layer number increases from one to two, which is in good agreement with theoretic prediction.[129] In addition, a strong enhancement in PL intensity has been observed in ME-prepared WS_2 monolayers as reported by Zhao et al., which indicates that monolayer WS_2 is a direct bandgap semiconductor and the result is in good agreement with density function theory (DFT) calculations.[10] However, this PL enhancement was not distinctive for CVD-grown WS_2 films. Although it is well known that ME-prepared WS_2 thin films have less structural defects than CVD-grown samples, it lacks a directly comprehensive comparison study on the optical properties of samples prepared by both methods. In addition, it is not clear so far that whether the CVD samples still have some advantages over ME ones in the view of some particular optoelectronics applications.

In the chapter, the Raman, reflectance, PL and SHG response as a function of layer thickness varying from monolayer to bulk of the thin WS_2 films prepared by both ME and CVD methods are investigated. For both sets of samples, the Raman peak position is generally in agreement with previous reports but the

intensity ratio of two characteristic Raman modes is quite different. The spectral peaks in the measured reflectance and PL for both samples experience a redshift as the layer number increases because of the diminished quantum confinement of excitons, which agrees well with theoretic simulation. However, the PL intensity and the detection polarization dependence of both samples exhibit a large difference. More interestingly, the SHG of a CVD-grown WS_2 bilayer is even stronger than that of an ME-prepared monolayer. These dramatically different vibrational and optical properties observed in the two sets of samples are physically explained in terms of their different amounts of structural defects as demonstrated by SHG mapping.

3.2 Experimental Methodology

3.2.1 Sample preparation

Thin WS_2 films are prepared by both ME and CVD methods. The ME-prepared flakes are exfoliated from a commercially available WS_2 bulk crystal and deposited on a quartz wafer.[10] The CVD-grown flakes on quartz are purchased from SixCarbon Technology (Shenzhen). In the CVD growth process, WO_3 powder placed on a silicon substrate is placed in the centre of a furnace at 1000 °C (heating rate 15 °C/min). The heating process is conducted under a pressure of 50000 Pa and a continuous gas flow of Ar (100 sccm) and H_2 (15 sccm). After keeping the temperature for around 30 mins, sulfur powder is

evaporated to react with WO_3. The heater which is carried out to heat up the furnace is then turned off and the samples are left in the chamber until cooling down to room temperature. With this method, thin WS_2 flakes (especially WS_2 monolayers) can be prepared and could be easily observed under an optical microscope.

3.2.2 Raman, PL and reflectance imaging and spectroscopy

Raman imaging and spectroscopic measurements are carried out at room temperature on a Horiba confocal microscope coupled with a spectrometer. The wavelength of excitation laser is 488nm and the output power is around 25μw. The exposure time is 5s for Raman spectroscopy. PL spectroscopic measurements are carried out with an NT-MDT confocal microscope system. The wavelength of the excitation laser is 532nm and the output power is around 10μw. The exposure time is 1s for PL spectroscopy. Raman mapping is carried out with the same NT-MDT confocal microscopy system (excitation wavelength 633nm and output power 100μw). The exposure time for one pixel (corresponding to an area of 0.25 μm^2) is 1s. In both spectroscopic and mapping measurements, a 100x objective lens (NA = 0.8) is applied for both focusing the excitation laser beam to the sample plane (at a spot size of ~1μm diameter) and collecting the emission signals from excitation areas.

Reflectance imaging and spectroscopic measurements are carried out on an

Olympus bright-field microscope installed with a tungsten quartz halogen lamp as light source. A 100x objective lens (NA = 0.8) is applied for both focusing the incident white light to the sample plane and collecting reflected signals to a spectrometer installed with a TE-cooled CCD. Differential reflectance is calculated as $1-R_{sa}/R_s$, where R_{sa} and R_s are the reflected light intensities from samples and substrates, respectively.

3.2.3 Excitation- and detection-polarization-dependent PL spectroscopy

Polarization-resolved PL spectroscopic measurements are carried out at room temperature on the NT-MDT confocal microscopy system where a polarizer is inserted in the detection path to examine the linear polarization response of PL signals from samples. For the circularly polarized excitation, a quarter-wave plate is inserted in the excitation path to generate either a left- or right-handed circularly polarized beam by adjusting the orientation of the quarter-wave plate to be +45° and -45° with respect to the laser polarization direction, respectively. A combination of a quarter-wave plate and a polarizer is inserted in the detection path to collect either right- or left-handed circularly polarized PL signals. The measurements are conducted with a 100x objective lens (NA = 0.8). The laser output wavelength is 532nm and the output power is around 100μw. The exposure time is 1s.

3.2.4 SHG imaging and spectroscopy

SHG spectroscopic measurements are carried out on a commercial laser scanning confocal multiphoton system (Leica TCS SP8 MP Multiphoton Microscope), installed with a Ti:sapphire femtosecond laser. The pulse width and repetition rate of the laser are about 500 fs and 80 MHz, respectively. The power density at the sample plane is around 10^6 W/cm^2 after focused by a 100x objective lens (NA = 0.95). SHG signals are collected by the same objective lens and transferred to a HyD detector after dispersed by a prism. To measure the incidence polarization dependence, a broadband half-wave plate is inserted in the excitation optical path before the objective lens to control the polarization direction by rotating the wave plate mechanically. A change of θ in the half-wave plate results in a change of 2θ in the incident polarization direction.

3.3 Optical images and Raman mappings

The layer number of samples prepared by both CVD and ME methods is roughly determined by contrast of their reflectance image (Figure 3.1(a) and (c) and the mapping of Raman scattering spectra (Figure 3.1(b) and (d) for the A_{1g} Raman mode). As shown in Figure 3.1(a) and (c), the bright-field reflectance images of the two samples show obvious differences in colours and the reflectance intensity increases as layer number increases for both samples. Similarly, Figure 3.1(b) and (d) show that the intensity of the A_{1g} mode increases as the layer number of the samples increases, which can result from the increased

strength of interlayer interaction.[24] Therefore, the thickness of the WS_2 flakes can be roughly identified by contrast of their reflectance image and Raman mapping. Particularly, the monolayer regions in the Raman mapping of the CVD-grown WS_2 sample (Figure 3.1(b)) show light blue, the bilayer regions show light green and the tri-layer regions show light yellow. The multilayer regions in this image show orange and the bulk regions are in red colour. For the Raman image of the ME-prepared sample (Figure 3.1(d)), the monolayer regions are in blue, the bilayer regions are in light blue and the tri-layer regions are in light green. The multilayer regions in this image are in yellow mixed with orange and the bulk regions are in red. It can be observed that the thickness-dependent reflectance intensity contrast is consistent with the signal intensity mapping of the A_{1g} Raman mode.

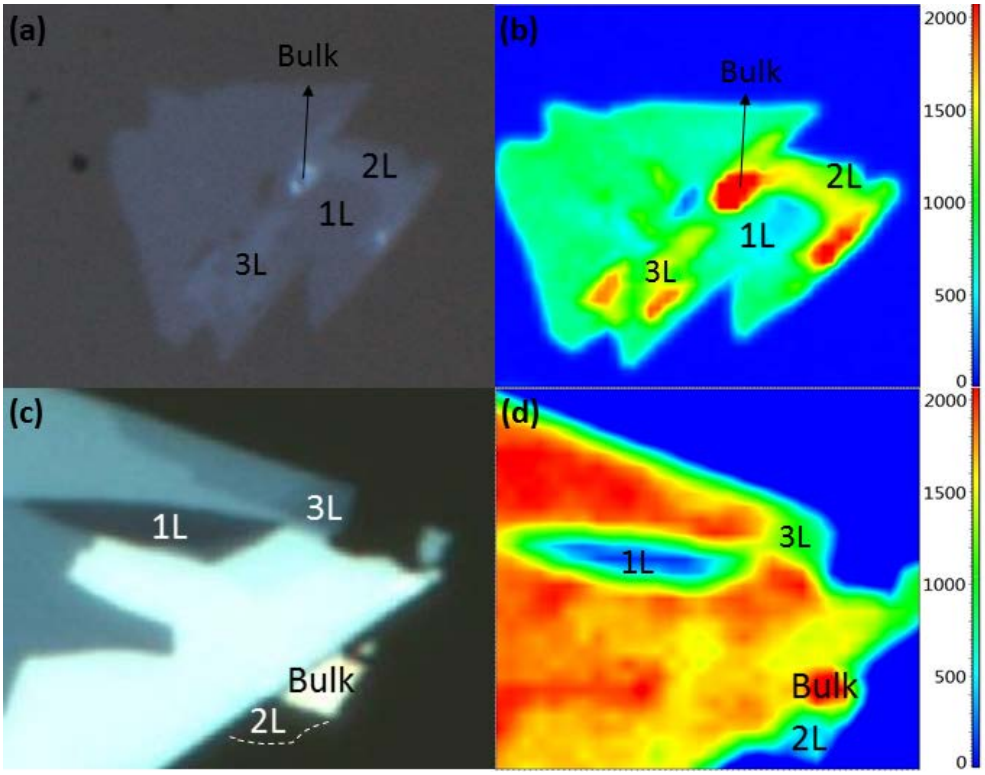

Figure 3.1 (a and c) Optical reflectance images of a CVD-grown WS_2 flake on quartz (a) and a ME-prepared one on quartz (c). The labeled layer numbers of different regions were roughly determined by optical contrast and precisely determined by Raman spectroscopy later. (b and d) Signal intensity mapping of the A_{1g} Raman mode for the same samples as in a and c. The size of the reflectance and Raman images is 20 x 20 μm^2 for the CVD-grown sample (a and b) and 10 x 10 μm^2 for the ME-prepared sample (c and d).[130]

3.4 Layer-dependent Raman scattering measurements

Figure 3.2(a) and (b) show the Raman spectra for different regions of the CVD-grown and ME-prepared samples, respectively. For both samples, two strong spectral peaks at 356 and 420 cm^{-1} can be observed, which are corresponding to the E_{2g}^1 (in-plane vibration) and A_{1g} (inter-layer vibration) Raman modes, respectively. It is noticed that the E_{2g}^1 Raman shift has a very slight change when the layer number increases from one to three (only around 0.5 cm^{-1}). However, the A_{1g} Raman shift has an intense redshift, which is up to 3 cm^{-1}. From monolayer to tri-layer, the corresponding Raman shift difference between the two peaks is around 62.6, 63.4 and 64.5 cm^{-1}, respectively, which are consistent with previous results.[26,131] With these results, it can be confirmed that the layer numbers labelled in Figure 1 are correct. In addition, Figure 3.2(c) shows that the difference between the Raman shift of the two modes for the CVD

and ME samples has little dependence on the synthesis methods. However, the intensity ratio of the two modes as a function of layer number is quite different for the two samples as shown in Figure 3.2(d). In general, due to the in-plane vibration nature, the E_{2g}^1 Raman mode has a stronger intensity than the A_{1g} Raman mode for monolayer WS_2. As the layer number increases, the intensity of the E_{2g}^1 Raman mode does not have an obvious change but that of the A_{1g} mode dramatically increases. This general behaviour can be observed for the ME-prepared sample but cannot be observed for the CVD-grown sample in Figure 3.2(d), pointing out possible existence of structural defects in the CVD sample.

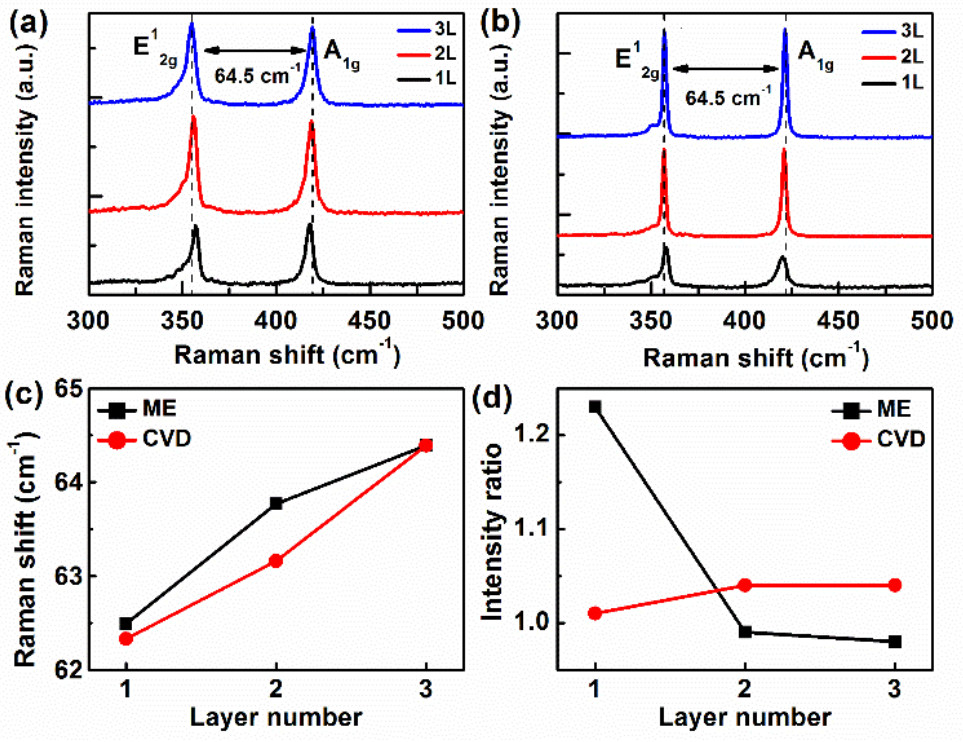

Figure 3.2 (a and b) Normalized Raman spectra for the CVD (a) and ME WS_2 (b) as a function of layer number. The peaks at the left represent Raman mode and the peaks on the right are the A_{1g} mode. (c) Raman shift difference between

the E_{2g}^1 and A_{1g} modes as a function of layer number for both samples. (d) Intensity ratio of the E_{2g}^1 and A_{1g} modes as a function of layer number for both samples.[130]

3.5 Layer-dependent differential reflectance measurements

Differential reflectance can be applied to determine absorbance of 2D materials on a transparent substrate (e.g. quartz) under weak absorption approximation of thin films. For this purpose, the thin WS_2 flakes are on the quartz substrate. The change in reflectance (δR) for a thin layer sample is closely related to the absorbance (A) of the material. The relationship between δR and A can be described by the following formula:

$$\delta_R(\lambda) = \frac{4}{n_{\text{sub}}^2 - 1} A(\lambda)$$

where n_{sub} represents for the refractive index of the substrate and we assume this index independent on the wavelength.[10] Figure 3.3(a) and (b) show the measured differential reflectance spectra for different areas in the two samples, respectively. Three sharp peaks labelled as A, B and C are observed in the spectra, demonstrating the appearance of the exciton states. For a single-photon absorption process, the s orbital states of different excitons induce resonant absorption of incident photons with particular energies, which result in the sharp peaks observed in the differential reflectance spectra at certain wavelengths.[132]

Based on conventional understanding of orbital states of excitons, the exciton state with the lowest quantum number has the highest transition probability.[32,133] This indicates that the three spectral peaks are most likely associated with the 1s orbital resonance absorption of different excitons.[134] The peaks A and B located at around 613 nm and 520 nm are generally recognized as the 1s exciton absorption of the excitons A and B at the *K* valley where they share the same excited state but with different initial ground states.[135] The difference in the excitation energy of the excitons A and B corresponds to the energy difference of two splitting valleys induced by spin-orbit coupling. The reflectance peak C is associated with the density of state peak in the conduction and valence bands of WS_2.[10]

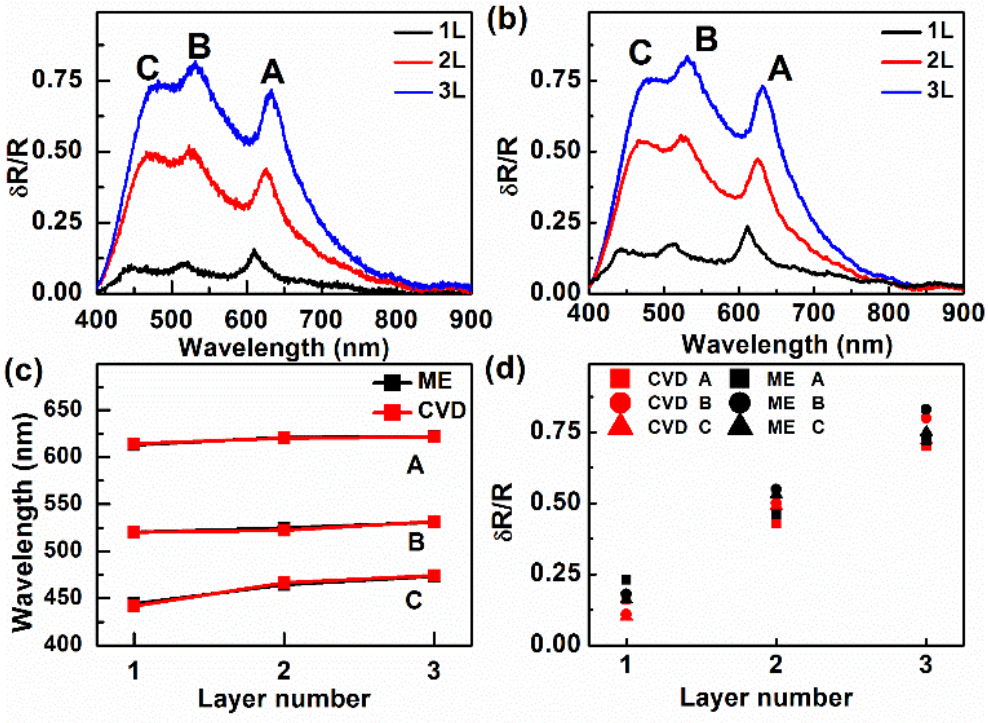

Figure 3.3 (a and b) Differential reflectance spectra of the CVD (a) and ME WS_2 (b) as a function of layer number. Both samples were on quartz. The y axis

represents the differential reflectance intensity defined as $1-R_{sa}/R_s$, where R_{sa} and R_s are the reflected light intensities from the sample area and the bare substrate, respectively.[6] (c and d) Spectral position (c) and intensity (d) of the differential reflectance peaks labelled as A, B and C in (a) and (b) as a function of layer number for the ME and CVD samples.[130]

As shown in Figure 3.3©, the reflectance peak positions as a function of layer number are nearly the same for the CVD and ME samples, agreeing well with the previously reported results.[10,136] All three sets of reflectance peaks exhibit a gradual redshift with increasing layer number, also consistent with the previous observation.[10,129] The amount of peak redshift from the monolayer to tri-layer WS_2 is around 10 nm for the reflectance peaks A and B and 30 nm for the peak C. This difference further signifies different physical origins of the excitons A, B and C as mentioned above. In addition, the layer number dependences of differential reflectance intensity for the two samples are quite similar with each other. Besides, the absolute intensity of differential reflectance for the ME-prepared thin WS_2 films is close to the CVD-grown counterparts. That small difference indicate the quality of the CVD-grown sample is close to that of the ME-prepared one, suggest this CVD method is comparable to the ME method.

3.6 Layer-dependent PL measurements

Different from the differential reflectance spectra, the PL spectra of the CVD-grown and ME-prepared WS_2 samples have notable dependence on the layer number. As shown in Figure 3.4(a), the most obvious PL peaks for the CVD-grown 1 to 3 layers are labelled as A, which is related to the direct band gap transition between the conduction band and valence band at the *K* point in the Brillouin zone.[6,137] The PL peak wavelength of the monolayer WS_2 is at around 633 nm (1.959 eV) from Figure 3.4(a), which is very close to the direct band gap energy of monolayer WS_2 (1.96 eV).[10] As the layer number increases from 1 to 2, the peak wavelength shows an intense redshift. However, a blueshift is observed when the layer number increases from 2 to 3, in good agreement with the previous result.[10,138] Such transition of PL peak wavelength from redshift to blueshift is related to the quantum confinement effect which is significantly enhanced at the thickness of WS_2 less than two layers. Such peak shift is accompanied with a dramatic decrease in the PL intensity when the layer number increases from 1 to 3. In particular, the PL intensity of the WS_2 monolayer is almost three times of the PL intensity of the WS_2 bilayer, which is simply due to the transition from the direct to indirect band gap. Therefore, the PL intensity in the tri-layer WS_2 should be much weaker than the monolayer and bilayer ones, which can also be directly observed in figure 3.4(a). Figure 3.4(b) shows similar results for the ME-prepared WS_2 with the results for CVD-grown WS_2 in figure 3.4(a). As expected, the PL intensity of the ME-prepared monolayer is much

larger than that of the CVD-grown monolayer, around three times increase. However, the PL intensity of the ME-prepared monolayer is nearly ten times that of the ME-prepared bilayer and tri-layer WS_2. This indicates the presence of a large amount of structural defects in the CVD-prepared WS_2 which significantly degrades the photoluminescence efficiency of monolayer WS_2 but slightly improves the efficiency of bilayer WS_2.

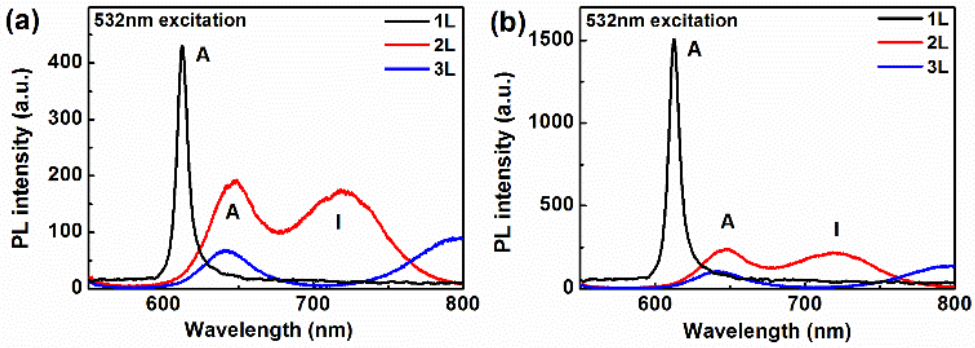

Figure 3.4 (a and b) Measured PL spectra of WS_2 flakes prepared by CVD method (a) ME method (b) both consisting of 1-3 layers. The peaks A in the graph represent the direct bandgap transitions and the peaks I the indirect bandgap transitions.[130]

3.7 Linear- and circular-polarization-dependent PL measurements

Polarization-resolved PL spectroscopic measurements are carried out on both ME and CVD samples to study the effects of fabrication processes on their valley polarization properties. Figure 3.5(a) and (b) show the PL intensity as a

function of detected linear polarization angle. For a bilayer 2H-WS_2, each layer can be taken as a 180° in plane rotation of the neighbouring layer and the locations of W atoms of one layer are just on the top of the S atoms of the other layer. This structural symmetry interchanges the *K* and *K'* valleys but keeps the respective spin state, which can consequently suppress the interlayer coupling. This feature of a bilayer WS_2 presents a more robust valley polarization than a monolayer WS_2.[16,27] A linearly polarized light can be regarded as the superposition of two circular polarized lights with a certain phase difference, which is directly related to the linear polarization direction of the polarized light. If the valley polarization of the bilayer WS_2 has been maintained, the phase difference between the two circular polarized emissions should be kept. Therefore, the PL should have the same polarization state as the excitation light which means the PL from WS_2 should also be a linear polarized light. For the ME-prepared bilayer WS_2, the detection-polarization-dependent PL can be well fit with $\sin^2(\theta)$ as shown in Figure 3.5(b), indicating that the generated PL has a good linear polarization. However, the generated PL from the CVD-grown bilayer is almost independent on the detection polarization angle as shown in Figure 3.5(a). The PL spectra with maximum and minimum intensity for both samples shown in Figure 3.5(c) and (d) further elaborate such direct comparison. To quantitatively characterize the polarization response of the generated PL, a degree of linear polarization is defined as $P = |(I_{max} - I_{min}) / (I_{max} + I_{min})|$, where I_{max} and I_{min} are the collected maximum and minimum PL intensities,

respectively.[27] For the ME-prepared WS_2 bilayer, the difference in the maximum and minimum PL intensities is quite large and the degree of linear polarization is around 40%. However, the difference in the PL intensity for CVD-grown bilayer between different linear polarized detection is quite small and the degree of linear polarization is around 8%. These results further demonstrate the different contents of structural defects present in two sets of samples.

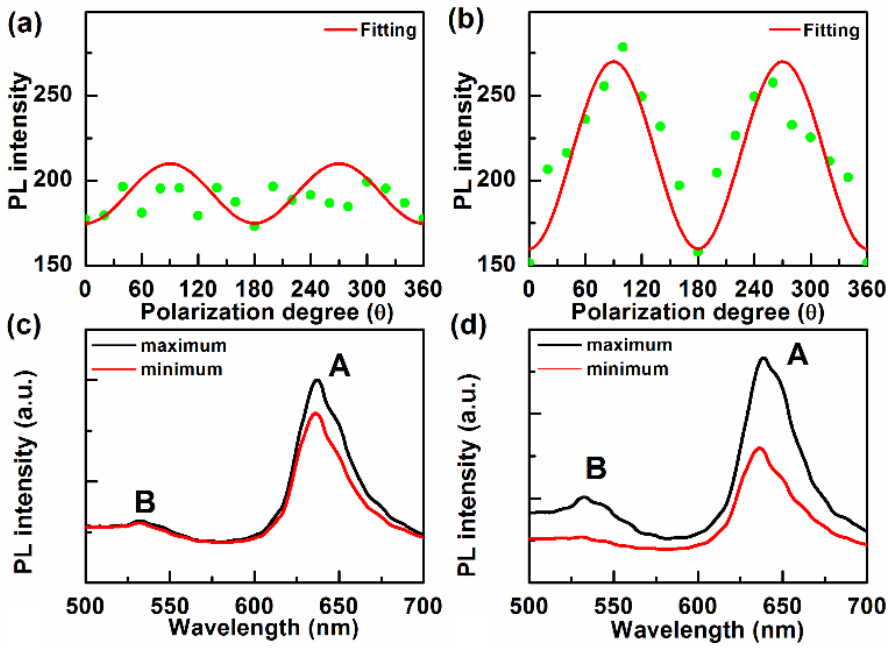

Figure 3.5 (a and b) Measured PL peak or integrated intensity as a function of detection polarization for a CVD-grown (a) and a ME-prepared (b) WS2 bilayer. The green dots are the experimental data and the red lines are the fit of $\sin^2(\theta)$. (c and d) Measured PL spectra of maximum and minimum intensities for the CVD bilayer (c) and ME bilayer (d).[130]

As mentioned above, monolayer WS_2 has a direct band gap where the band edge is located at the *K* and *K'* valleys of the first Brillouin zone.[128] Figure 3.6(a)

shows the detected right- and left-handed (σ+ and σ-) circularly polarized PL spectra of the CVD-grown bilayer WS_2 under a right-handed circularly polarized laser excitation, which exhibit almost no difference in the PL intensity. In sharp contrast, the PL spectra of the ME-prepared sample in Figure 3.6(b) show a huge difference in the intensity for the right- and left-handed detection. Since the PL intensity is dominated by the A exciton transition at the *K* and *K'* valleys, the generated PL should follow the same helicity of the circularly polarized excitation field according to the valley-selective optical selection rules.[139] Similar to the linear excitation polarization analysis, the circular detection polarization dependence can also be quantitatively evaluated by defining a degree of circular polarization, i.e. $P = |(I_{\sigma+} - I_{\sigma-}) / (I_{\sigma+} + I_{\sigma-})|$, where $I_{\sigma\pm}$ are the PL intensities measured from the right- and left-handed circularly polarized detection, respectively.[139] The degree of circular polarization is observed to be around 50% for the ME-prepared bilayer WS_2, which is consistent with the valley optical selection rule and in good agreement with the previous work.[139–141] However, this parameter for the CVD-grown bilayer is only around 7%.

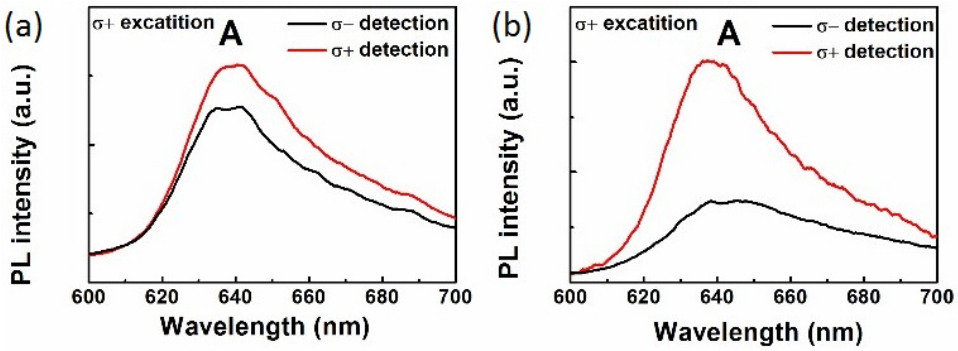

Figure 3.6 (a and b) Detected left- and right-handed circularly polarized PL spectra for the CVD (a) and ME bilayer (b) under a right-handed circularly polarized excitation.[130]

3.8 SHG measurements

Finally, the SHG responses of the two sets of samples are also explored, which in turn provides indirect evidence for the presence of grain boundaries and structural dislocations in the CVD-grown samples. Here large-area monolayers and bilayers are selected from the CVD-grown sample on the same substrate as the sample studied above to ensure the same quality and fair comparison. As shown in Figure 3.7(a), the ME-prepared monolayer WS_2 has a strong SHG at 450 nm under 900 nm femtosecond laser excitation, which is much stronger than that of the CVD-grown monolayer, simply due to the poor quality of the CVD-grown samples. In general, due to the lack of inversion symmetry, monolayer WS_2 exhibits an extraordinary second-order nonlinear susceptibility (origin of SHG), which is supposed to be absent in bilayer 2H-WS_2,[142–144] consistent with the measured negligible SHG signal for the ME-prepared bilayer (result which is not shown). Surprisingly, Figure 3.7(a) shows that the CVD-grown bilayer WS_2 has a much stronger SHG than both the ME-prepared and CVD-grown monolayers. This unexpected phenomenon indicates the presence of structural defects, such as dislocations and polycrystalline in the

CVD-grown sample. For an ideal bilayer 2H-WS_2, the SHG response of the first layer and the second layer would cancel with each other, leading to a negligible SHG response. When bilayer WS_2 samples are grown with typical CVD methods, however, the upper layer tends to nucleate on the grain boundaries of the first polycrystalline layer, which may form structural dislocations and make the CVD-grown bilayer become a non-ideal 2H structure. Such imperfect structure is expected to give rise to an unexpected strong SHG response because of the partial lack of the inversion symmetry. The second-order response of these samples is further verified by the quadratic dependence of measured SHG signals on the excitation power as shown in Figure 3.7(b).

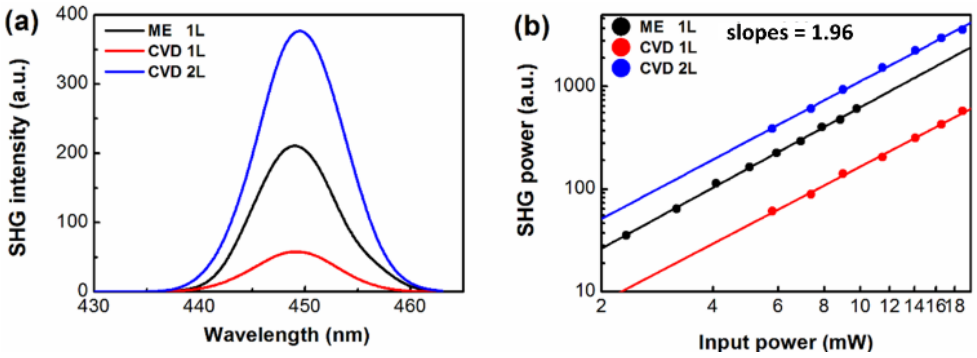

Figure 3.7 (a) Measured SHG spectra of a ME-prepared WS_2 monolayer and CVD-grown WS_2 monolayer and bilayer under 900 nm fs laser excitation. The angle between the incidence polarization direction and the crystal orientation is fixed to be the same for the three measurements. (b) Corresponding excitation power dependences of the SHG signals shown in (a) in log-log sale. Dots are experimental data and lines are linear fits.[130]

To further understand the unexpected SHG response of the CVD-grown samples, excitation-polarization-dependent SHG was measured. It is well known that monolayer WS_2 has a D_{6h} crystal symmetry,[145,146] which means the crystal orientation will be the same after every in-plane rotation of 60°. With this type of symmetry, the second-order nonlinear susceptibility tensor should have nonzero elements of $\chi^{(2)} = \chi^{(2)}_{x'x'y'} = \chi^{(2)}_{x'y'x'} = \chi^{(2)}_{y'x'x'} = -\chi^{(2)}_{y'y'y'}$, where *x'* and *y'* are crystalline coordinates.[147] Here, *x'* is along the armchair direction and *y'* should be perpendicular to the direction of *x'*. Due to this structural symmetry, the polarized SHG signal intensity is expected to have an angle dependence.[148,149] The previous result shows that when the incident laser beam is polarized along a horizontal direction (here we defined this direction as *x*), the parallel (*x*) and perpendicular (*y*) components of the SHG field should be proportional to $sin3\theta$ and $cos3\theta$, respectively, where θ is the angle between the direction of crystalline coordinates *x'* and the incident beam direction *x*. In physics, when the incident pump laser beam is polarized along a certain direction, the SHG emission power should follow $P_x \propto \sin^2(3\theta)$ and $P_y \propto \cos^2(3\theta)$ but the total power should be independent of θ.[150]

Normally, the broken inversion symmetry of the thin monolayer WS_2 shows a strong SHG signal. Due to that reason, the high-quality CVD-grown monolayer sample should exhibit a uniform SHG intensity result from the SHG mapping figures. However, some obvious edges (marked as yellow dash lines) can be clearly observed from Figure 3.8(a). The edges can be inferred as the places

where the translational symmetry is broken. In our experiments, the incident polarization of the laser beam is along either x or y axis and the total SHG signal is collected. The uniform SHG intensity within each grain regions (e.g. I, II, III) can indicate that the individual grain regions consist of single crystals but at the grain boundaries, the subsequently decrease of SHG intensity can be observed. This result is caused by the destructive interference and annihilation of the SHG signals generated from the neighbour grains with different orientations.[150] Even though the grain boundaries is quite thin (only a few atom sites in width), the crystal boundaries could be seen clearly. However, such kind of edges seems to be absent in figure 3.8(b). From the previous analysis, a strong decrease of SHG intensity could be observed at the grain boundaries. So the absent of such kind of edges in bilayer CVD-grown WS_2 can indicate that an individual grain region consists of single crystals in the second layer grown on the grain boundaries of the first layer. This kind of polycrystalline structure can further support the results of linearly and circularly polarized PL shown in Figure 5. Besides, the result shown in figure 3.8(b) could also further support the prediction that the upper layer tends to nucleate on the grain boundaries of the first polycrystalline layer.

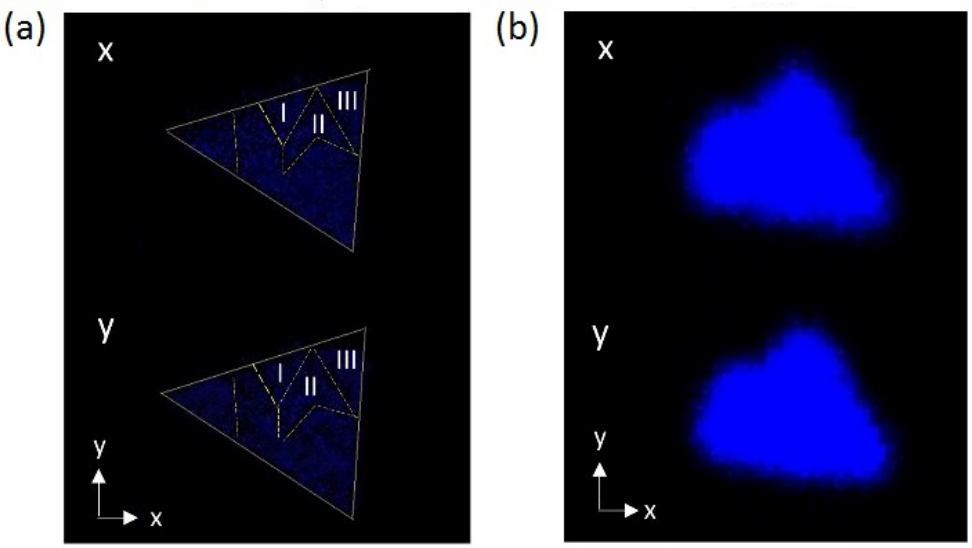

Figure 3.8 (a and b) Excitation-polarization-resolved total SHG images for a CVD-grown monolayer (a) and bilayer (b) with incident polarization along axis *x* and *y*.[130]

3.9 Conclusion

In summary, the optical and vibrational properties of monolayer and few-layered WS_2 flakes prepared by typical CVD and ME methods have been comprehensively investigated and compared. The results in this chapeter collectively point out that although both un-polarized differential reflectance and photoluminescence spectroscopies seem incapable of distinguishing the structural quality of CVD-grown and ME-prepared samples, polarization-resolved photoluminescence imaging and spectroscopy reveal dramatic differences in the two sets of samples because of their high sensitivity to crystal structural symmetry. In contrast to the optical properties, the spectral

positions of Raman modes of the samples prepared by both methods have almost no difference yet their layer number dependent intensity ratio depends on the synthesis methods. We conclude that the nonlinear optical response of CVD-grown samples such as second-harmonic generation seems superior to that of ME-prepared samples because the crystal structure of CVD-grown bilayer WS_2 undergoes significant breaking of the spatial inversion symmetry due mainly to the presence of polycrystalline domains and structural dislocations, pointing out the promise of using CVD-grown bilayer TMDCs in general for nonlinear optoelectronics.

	CVD-grown	**ME-prepared**	**Analysis**
Reflectance	Good	Good	Quality comparable
PL	Low-efficiency	High-efficiency	ME > CVD
Circular-Polarized PL	More Depolarization	Less Depolarization	Choose ME
Linear-Polarized PL	More Depolarization	Less Depolarization	Choose ME
SHG	Strong in even	Only in odd	Large-area devices - CVD

Table 3.1 Summary about the performance of samples prepared by two different methods.

Chapter 4 Probing dark excitons in atomically thin TMDs through plasmonic gap modes in metal film-coupled nanostructures by polarization resolved Photoluminescence spectroscopy

Excitons in TMDs have attracted much attention because of their close relations with exchange interaction between the electron-hole pairs and light emissions. Depending on the spin configuration of the electron-hole pairs, the excitons of TMD monolayers can be either bright or dark through optical transition. Limited by the selection rules, radiative emission through dark excitons is generally forbidden due to their anti-parallel spin configuration. Dark excitons have potential applications in quantum computing and optoelectronic due to their long lifetimes. However, the method to brighten and control the dark excitons has remained challenging because dark excitons are difficult to couple with light. In addition, previous methods to optically excite the dark excitons also suffer from low-temperature experimental conditions or complication of the experimental set up. This chapter introduces a novel method for probing the dark excitons of TMDs through plasmon-exciton coupling. Using a 2H-WS_2 monolayer on the gold substrate and plotting a gold nanosphere on its surface, the radiation of dark excitons at room temperature can be observed by applying

the polarization-resolved photoluminescence (PL) detection. To further analyze the spectra, a fitting model which can directly demonstrate the optical properties and polarization dependence of PL from dark and bright excitons has been established. This approach provides a novel way to optically detect the dark exciton and analyze the excitonic characteristics directly in low-dimensional materials under room temperature, offering many potential applications in optoelectronics.

4.1 Introduction

Recently, two-dimensional transition metal dichalcogenides (TMDs) have attracted much attention due to their unique optical and electronic properties.[53,151] These 2D TMDs exhibit a direct bandgap when their thickness reduces to monolayer, which creates tightly bound excitons with strong Coulomb interaction and particularly large binding energy.[130,152,153] With these unique excitonic properties and strong light-matter interactions, 2D TMDs suggest a wide range of applications in optoelectronics.[12,154] In monolayer TMDs, due to the broken inversion symmetry and strong spin–orbit coupling effects, a spin- and energy-splitting in the conduction band will occur.[155,156] The electrons in the two respective states of the spin-split conduction bands have spins with anti-parallel orientations.[157] These electrons, combining with the holes in the related valence band, could give rise to the bright and dark excitons.[158] Besides, depending on the spin configuration, the transition dipole orientations of these

two distinct states of excitons are perpendicular to each other, which have been demonstrated recently both theoretically and experimentally.[159–161] Different from the bright excitons, dark excitons (X_D) have longer lifetimes due to merely non-radiative decay channels and spin flip processes.[162,163] This unique nature of dark excitons in TMDs has attracted many research interests for potential applications, such as coherent two-level systems for quantum information processing[164] and Bose–Einstein condensation.[165] Protected by the optical selection rules, the optical transitions in semiconductors only occur intensely when the spins of the electrons do not change. As a result, when the orientations of the electron spins are perpendicular to the plane (z direction), excitons with zero spin ($S_z = 0$, arise from the bands with the same electron spin) are bright, while excitons with non-zero spin ($S_z = \pm 1$, arise from the bands with opposite electron spin) are dark, thus the dark excitons are quite difficult to be accessed optically.[166]

In order to enhance the optical emission of dark excitons in atomically thin TMDs, different approaches can be applied by either enhancing the efficiency of the excitation procedures or increasing the emission intensity. By putting an absorber at the local hotspot, the field around the absorber can be enhanced and this thus enhances the absorption process.[167] By applying the Purcell effect of cavity systems, the optical local density of state around the emitter can be increased to enhance the emission process.[168] Both of them can be achieved by the structure with ultra-small gap[169] or localized surface plasmon resonances

(LSPRs).[170] The gap structure can increase the optical density of state in the gap by concentrating the field from the environment into the gap. This thus induces a strong field enhancement at the gap position and at the same time enhances the Purcell effect.[171] The enhancement from the gap structure always occurs at a wide wavelength range. On the contrary, LSPR can enhance the field at a certain wavelength through the resonance effect, leading to several orders of local field enhancement.[172] Recently, Park et. al demonstrate an approach to brighten the dark exciton through tip-enhanced PL spectroscopy under room temperature by using the gap mode between the gold tips and the gold film.[173] Apart from the field enhancement from gap mode, the Purcell effect arising from the plasmonic resonance of single nanoparticle has also been demonstrated.[174] By exciting the out-of-plane polarized surface plasmon polaritons (SPP), the radiative emission of dark excitons can be induced by the coupling between SPP and dark excitons.[174] To further enhance the emission efficiency of dark excitons, the novel plasmonic nanocavity formed by metal-film-coupled nanoparticle could be a good candidate since it could provide both a gap mode and the Purcell effect by plasmonic resonance.[101,175]

This chapter demonstrates a novel method to detect the dark excitons based on the resonant field enhancement from the gap mode of metal-film-coupled nanocavity. The gap mode in a metal-film-coupled nanocavity provides a z-axis dipole which can be easily coupled with the dark excitons due to the coincidence of the orientations. The exfoliated WS_2 monolayers are mechanically transferred

onto the gold metal film and gold nanospheres are assembled onto the top surface of the monolayer WS_2. By applying the polarization resolved PL spectroscopy, a blue shift of the PL peaks can be observed when the detected polarization angle is changed from the 0° (parallel to the incidence polarization) to 90° (perpendicular to the incidence polarization). Such a blue shift is a strong evidence for the emission of dark excitons since it has a different energy and emitting polarization. The collected PL spectra are well fitted by a fitting model incorporating both bright and dark exactions, further confirming the observation of dark excitons at room temperature. Moreover, based on such fitting model, the different characteristics of dark and bright excitons including their energies, emission intensities, linewidths and especially the polarization orientations have been analyzed. Therefore, this chapter presents a novel and efficient approach to study the property of dark excitons in TMD monolayers at room temperature, which undoubtedly can be applied to many plexciton systems.

4.2 Experimental Methodology

4.2.1 Sample preparation

Monolayer WS_2 flakes are mechanically exfoliated from a bulk crystal onto a scotch tape (3M Scotch, 18mm*50mm). Then the thin WS_2 flakes are adhered onto a thermal-released tape (REXPAN) by directly adhering the thermal released tape onto the WS_2 film on the scotch tape and mechanically lifted the thermal released tape up. After that, the tape with WS_2 films is adhered onto the

metal film and heated up to 125°C for 5mins. The tape can be easily removed after the heating process and the WS_2 flakes will be left on the metal film. The thickness of the thin WS_2 flakes are initially determined by optical contrast and then confirmed by AFM. The metal film is prepared on an ultra-clean Si wafer using a thermal evaporator (Denton, DV-502B). The metal film consists of two layers. The lower layer is Chromium (Cr) with the thickness of 5nm ± 0.5nm and the upper layer is gold (Au) with a thickness of 100nm ± 5nm. The heating process is conducted under a vacuum of 5×10^{-6} torr. Nanoparticles (60nm Au with 1nm CTAB, Nanoseeds) are assembled directly onto the Au substrates covered with thinWS_2 flakes by spin coating.

4.2.2 Dark-field scattering measurements

The dark-field scattering image and spectroscopy, together with optical microscopy and spectroscopy are carried out on an Olympus BX-51 upright microscope equipped with a standard dark-field optical module using a 100× dark-field objective (LMPlan, Olympus). A dark field condenser (NA=0.93) in the objective is used for focusing the incident white light to the sample plane and the main lens (NA=0.8) of the objective is applied for collecting signals to a spectrometer coupled with a TE-cooled CCD. The dark-field scattering intensity is regarded as $(I_s-I_b)/I_{ls}$, where I_s and I_b are the collected light intensity from the samples and backgrounds, respectively while the I_{ls} is the light source intensity, which is collected by the scattering intensity of the light source from the standard

diffused reflection white board. The detection-polarization-resolved dark-field scattering measurements are carried out on the same system and linear polarizers have been added to both the excitation optical path and detection optical path.

4.2.3 Detection-polarization-resolved PL measurements

The detection-polarization-resolved PL measurements are carried out on the WiTec confocal microscopy system with a TE-cooled CCD (UHTS 600, VIS). A linear polarizer is inserted into the detection path to examine the linear polarization response of the PL from the samples at room temperature. The measurements are conducted with a 100x objective lens (NA = 0.9). The laser output wavelength is 532nm and the output power is 0.5mw. The exposure time is 3s.

4.2.4 AFM

The Atomic Force Microscopy (AFM) characterizations are carried out on a Scanning Probe Microscope (Asylum MFP-3D Infinity) under AC mode. The experiment is conducted by a Si N-type SPM probe (AppNano ACTA-50).

4.3 Characterization of structural properties

Figure 4.1(a) shows a schematic diagram of the microscopy systems that have been applied in this chapter. The WS_2 monolayers are exfoliated from a commercial bulk crystal onto a scotch tape and then transferred onto the gold metal film by a thermal release tape. After the transfer procedure, the AuNS

solution is dropped onto the surface of the WS_2 by spin coating. The monolayer regions are roughly identified by the optical contrast from the bright field optical image and the position of the AuNS can be located under the dark-field optical images (Figure 4.1(b)). To further confirm the thickness of the sample, AFM measurements are conducted. The height profile in Figure 4.1(c) and (d) shows that the thickness of the identified monolayer region is 0.97 nm, which shows that the observed region has WS_2 monolayer.

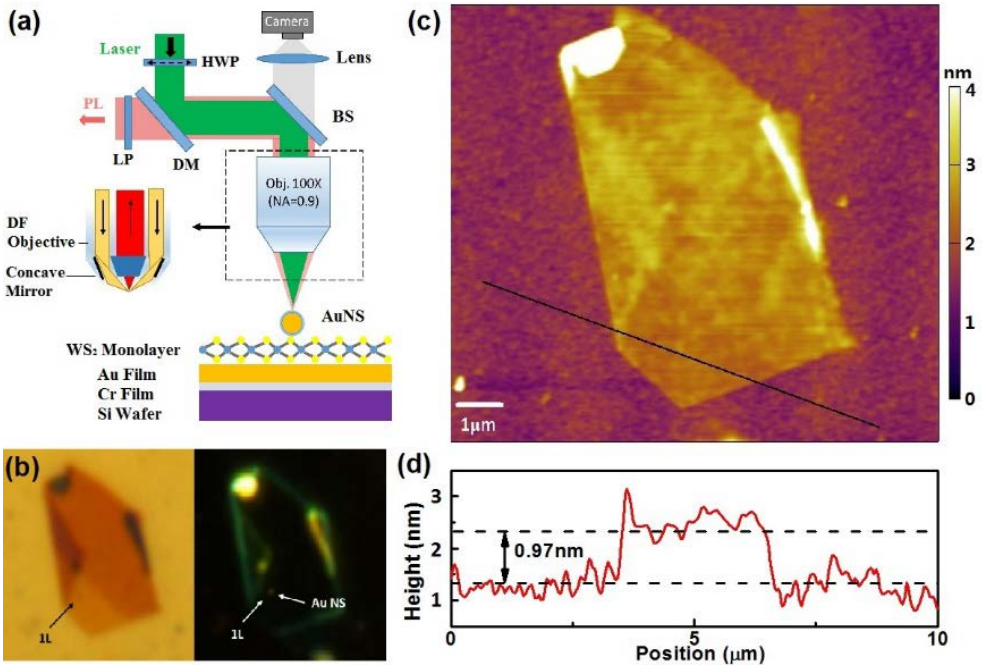

Figure 4.1 (a) Schematic of the experimental setup for dark-field scattering and polarized-resolved photoluminescence (PL). HWP: half-wave plate, DM: dichroic mirror, BS: beam splitter, LP: linear polarizer. (b) Bright- (left) and dark- (right) field images of a gold nanosphere (AuNS) on WS_2 supported by a Au film. The monolayer region and AuNS are labeled in the images. (c) A typical AFM image of the sample containing monolayer region. (d) Measured sample height as a function of position of the black line in figure 4.1(c). The

height profile shows a thickness of around 0.97nm in the monolayer region identified from bright field optical image.

4.4 Dark-field scattering and detection-polarization-resolved PL measurements.

To further examine the plasmonic properties of film coupled nanoparticles, the dark-field scattering spectra of the AuNS on the metal film with and without the monolayer WS_2 are examined. Figure 4.2(a) shows the dark field scattering spectrum of a single AuNS on the metal film with and without WS_2. The scattering spectra of the AuNS on Au film without the monolayer WS_2 exhibits two resonance modes, which are at wavelengths around 530nm and 710nm, respectively. To distinguish these two modes, linear polarizers are added into both the excitation and collection paths to control the polarization of the incident white light and collect the polarization dependent dark field scattering signal. The peak intensity at wavelength around 530nm shows a $cos^2\theta$ dependence on the detecting polarization angle, indicating a horizontally oscillating mode. In sharp contrast, the peak intensity at wavelength around 710nm shows almost no dependence on the detecting polarization angle since it is attributed to a vertically oscillating mode. As a matter of fact, the previous studies have identified these two modes at lower and longer wavelengths correspond to a horizontal and a vertical dipolar mode of the cavity, respectively.[101,175,176] Similarly, the dark field scattering spectrum of the AuNS on Au film with WS_2 also exhibits two peaks,

one at around 530nm and another at around 660nm. The blue shift of the vertical gap mode results from the increased gap distance between the AuNS and Au film by inserting the monolayer WS_2. However, no sign of peak splitting can be observed from the spectra, implying no plasmon-exciton coupling. This is reasonable since the vertical gap mode (out-of-plane) is orthogonal to the bright excitons (in-plane). The results in Figure 4.2(a) clearly show that there are two LSPRs which have different resonance frequency and polarization dependence in the system, which can be distinguished by the polarization resolved optical measurements.[175,177]

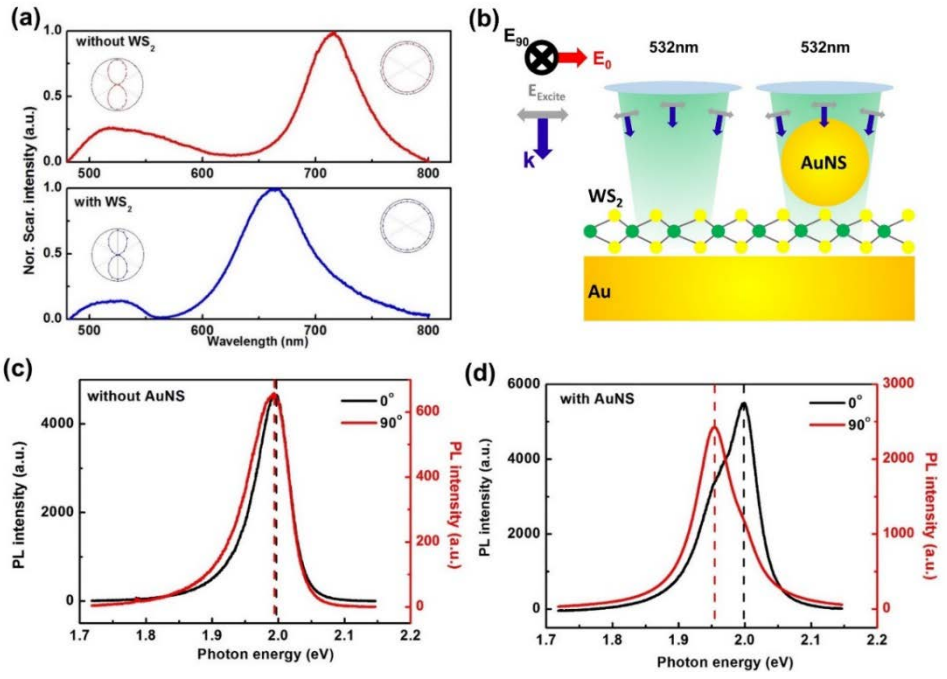

Figure 4.2 (a) Normalized dark field scattering spectra of AuNS on Au film with and without WS_2. The benched figures are detected linear polarization dependent peak intensities of different modes in the spectra. The incident light in the polarization test is linear polarized light and 0 degree means the detected polarization angle is same with the linear polarization direction of the incident

light. (b) Schematic diagram of PL measurement with detection polarization analysis. (c and d) PL spectrum at 0^o and 90^o degree polarization of WS_2 without (c) and with (d) AuNS. The left y-axis shows the PL intensity with detected polarization at 0° and the right y-axis shows the PL intensity with detected polarization at 90°. The dotted line indicates the photon energy of the PL peak.

To examine the coupling effects of the dark excitons and plasmons, this thesis further performed the detection polarization-dependent PL measurement as sketched in Figure 4.2(b). Here, 0^o degree and 90^o degree mean the detecting polarization is parallel and perpendicular to the polarization of the excitation laser, respectively. Figure 4.2(c) and (d) show the PL spectra of WS_2 with and without AuNS detected by different linear polarization angle. Interestingly, the PL spectra of 0^o and 90^o degree in the system with (Figure 4.2(c)) and without (Figure 4.2(d)) AuNS exhibit distinct features. In detail, an obvious blue shift of the peak in the PL spectra of 90 degrees with respect to that of 0 degree is observed in the system with AuNS (figure 4.2(d)) while in the system without AuNS (figure 4.2(c)) the PL spectra show no sensitive to the polarization of detection. This phenomenon implies that there are two PL emission modes with different photon energies and polarizations in this system. However, comparing the PL spectra with the dark field scattering result of the nanoparticles, these two modes are not related to the LSPR, which means both of them should arise from

the material only.

4.5 Fitting model

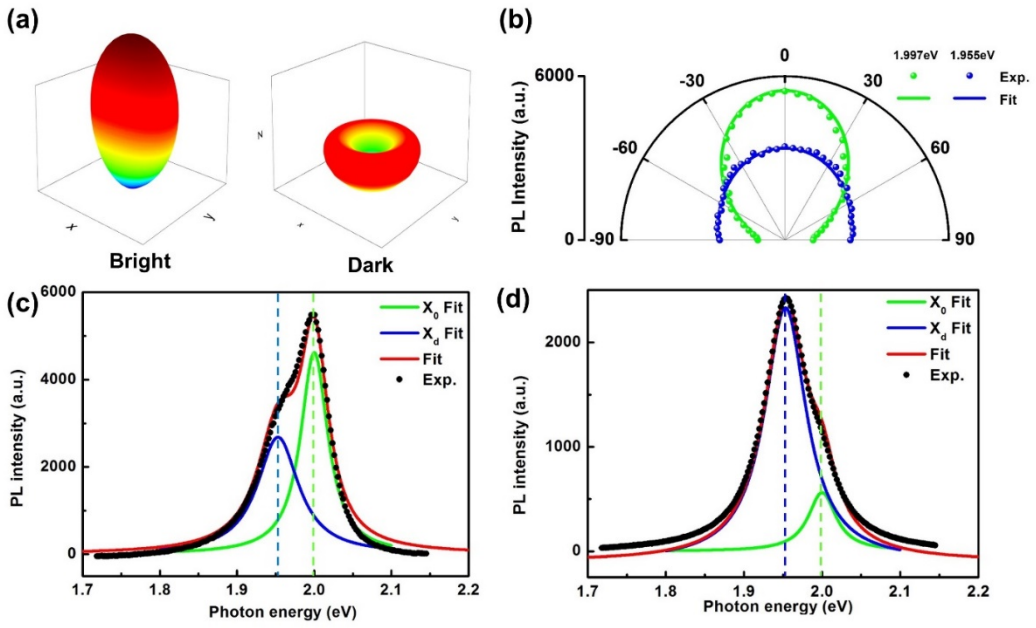

Figure 4.3 (a) Simulation of far-field radiation of horizontal (bright) and vertical (dark) dipoles in nanogap. (b) Fitted and experimental result of PL intensities with the dependence of different polarization angle. The selected data are at different photon energy which related to the fitted bright (1.997eV) and dark (1.955eV) photon energy, respectively. (c and d) The experimental and fitted result of PL spectra at detected polarization degree of 0 (c) and 90 (d), respectively. The dashed line shows the photon energy of the selected lines in figure 4.3(b). Figure 4.3(b) (c) and (d) show the fitted result.

To further understand the blue-shift of the PL peak in Figure 4.2(d), this thesis analyzes the whole detection-polarization dependent PL spectra by

establishing a physical model. In elemental or binary semiconductors, because the bound exciton has almost no kinetic energy, the line width of the bound exciton is smaller than kT.[178] Therefore, the theoretical line shape of bound excitonic optical transitions in binary semiconductors can be approximately fitted by a Lorentzian function, which is

$$L(E) = \frac{\Gamma^2}{\Gamma^2+(E-E_0)^2} \quad (1)$$

where E_0 is the energy center and Γ is a parameter specifying the width. The PL arises from bright exciton is dominated by the emission from so-called 'A' exciton at K and K' valleys. The excitons carry a clear circular dichroism under the excitation with circularly polarized light due to the valley optical selection rule, which means the PL follows the same helicity as the incident optical field.[139] A linearly polarized light can be considered as the coherent superposition of two circularly polarized light with opposite-helicity and a certain phase difference which determines the polarization direction.[139] So in semiconductors, a linearly polarized photon excites the excitons with energy transfer and emits a photon retaining the same polarization as the incident light. As a result, the detected PL intensity as a function of the detecting polarization angle should follow a $cos^2\theta$ dependence. However, due to the thermal effects and existence of relaxation time, the degree of polarization will decrease in experimental conditions. In all, the PL intensity arises from bright excitons could be fitted by

$$\chi_{bright}(\theta) = \alpha_0 cos^2\theta + \alpha_1 \quad (2)$$

where θ is the detected polarization angle with respect to the excited linear polarization angle and α_0, α_1 are constant parameters.

Different from the bright exciton, the dark exciton has an out-of-plane transition dipole moment which mismatches the in-plane polarization of the incident light. However, the excitation of the vertical gap mode in the metal-film coupled AuNS system provides a strong z-direction field in the gap region, which can be easily coupled with the dark excitons. Besides, this plasmonic nanocavity also has a large Purcell effect at around this gap mode. Both of these two factors make it possible to brighten the dark excitons emission in this system. Since the transition dipole moments of dark excitons are out-of-plane (z-direction), the corresponding PL should show no dependence on the detecting polarization angle, with an intensity following

$$\chi_{dark}(\theta) = \beta_1 \tag{3}$$

where β_1 is a constant parameter.

Due to the thermal effects at room temperature, it is reasonable to consider the emission of bright excitons and dark excitons as two independent processes, which means their total PL intensity can be taken as the direct summation of each. In this regard, the polarization and energy dependent total PL intensity of the system can be written as follows:

$$\chi_{total}(\theta, E) = \chi_{bright}(\theta) \cdot \ L_{bright}(E) + \chi_{dark}(\theta) \cdot \ L_{dark}(E)$$
$$= \frac{{\Gamma_{bright}}^2}{{\Gamma_{bright}}^2 + (E - E_{bright})^2} (\alpha_0 cos^2\theta + \alpha_1) + \frac{{\Gamma_{dark}}^2}{{\Gamma_{dark}}^2 + (E - E_{dark})^2} \beta_1 \tag{4}$$

In this function, seven independent parameters Γ_{bright} ,

Γ_{dark}, E_{bright}, E_{dark}, α_0, α_1, β_1 need to be determined. Therefore, a fit on all the experimental data by this function for various photon energy (E) and detecting polarization angle (θ) can determine the best fitted parameters with the least error. The details about the fitting conditions are shown in figure 4.4. Upon varying E, the PL spectrum of a certain θ can be taken as the sum of two Lorentzian peak with the center at E_{bright} and E_{dark}, respectively. When varying θ, the PL intensities can be taken as the sum of functions (1) and (2), respectively. Figure 4.3(a) shows the far-field radiation of a horizontal (representing the bright exciton) and a vertical dipole (representing the dark exciton) in an ultra-small gap, which indicates the different linear-polarization dependences of bright and dark excitons. To further examine the accuracy, the fitted result needs to be compared with the experimental data. Figure 4.3(b), (c) and (d) show the fitting. Figure 4.3(c) and (d) show the fitted PL spectra as a function of the photon energy at 0 and 90 degree, respectively. It is clearly seen that the fitting results agree quite well with the experimental measurements, which also shows that the total PL spectra can be decomposed into two separated Lorentzian peaks at photon energies of dark and) excitons at 1.955eV and 1.997eV, respectively. Those two Lorentzian peaks have different intensities and widths due to different optical properties of bright and dark excitons. The energy difference between the bright and dark excitons is obtained as 42meV from the fit, which is also in good agreement with the previous experimental and theoretical results.[114,179]

In addition, in figure 4.3(b), the fitted and experimental PL intensities are compared as a function of the detecting polarization angle at the separated bright and dark photon energies marked by the dash lines in figure 4.3(c) and (d), respectively. Based on equations 2 and 3, it can be concluded that the total PL intensity at a certain photon energy should follow $\chi_{total} = a + bcos^2\theta$, where a and b are constants. The good agreement between the fitted and experimental results in Figure 4.3(b) further confirms the validity of the proposed model. In this regard, the characteristics (e.g. linear polarization dependence, emission peak width and intensity) of dark and bright excitons based on this fitting model can be analyzed by changing the polarization angle. In addition, the proportion of the contributions from bright and dark excitons into the measured PL intensity can be controlled by tuning the polarization angle of detection.

4.6 Fitting results

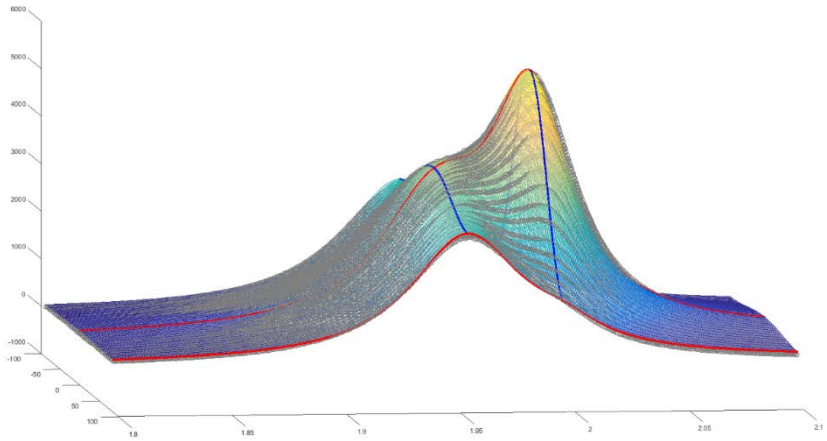

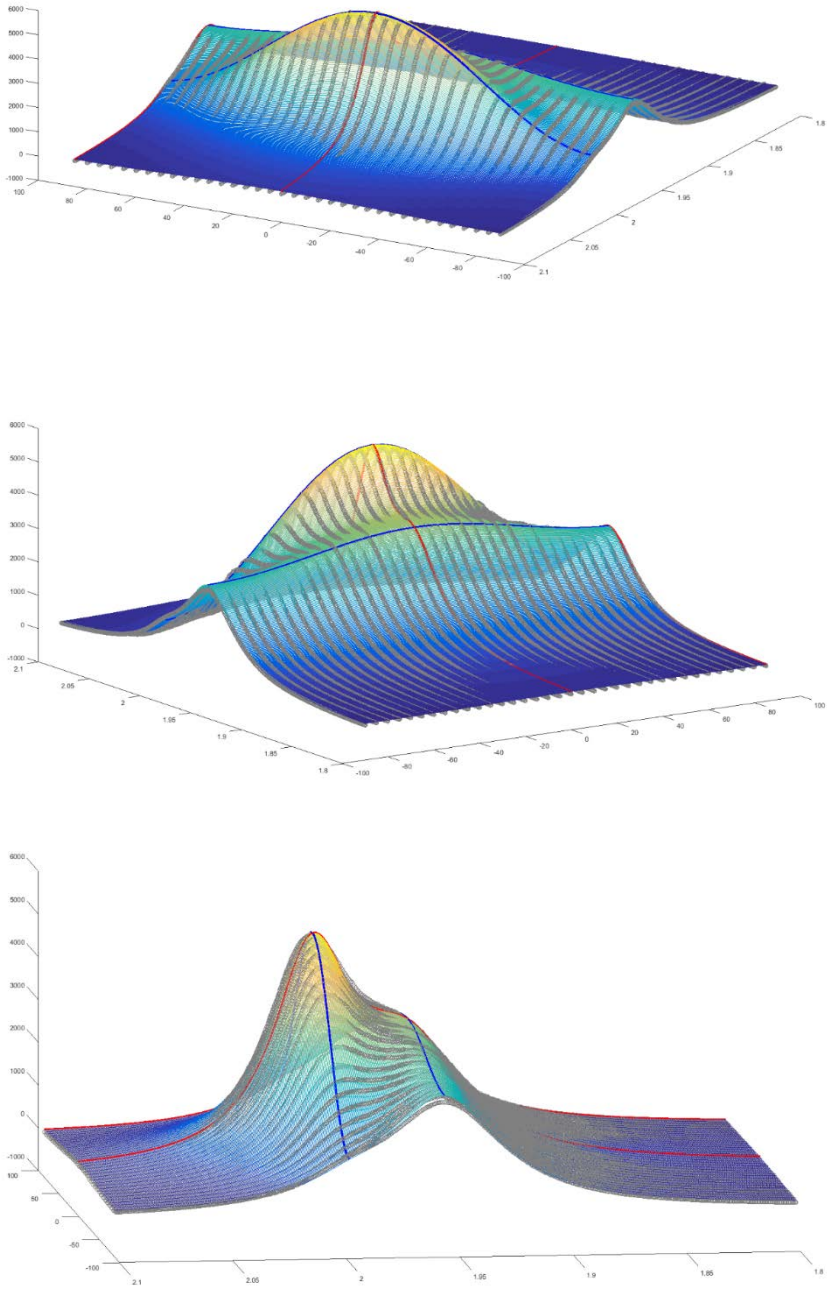

Figures 4.4 Demonstration of the fitting result in 3D plots. The figures are captured from different directions of view. The blue lines are related to the result in figure 4.3(b) and the red lines related to the result in figure 4.3(c) and (d). The surface shows the fitting result and the grey dots represent the experimental data.

4.7 Conclusion

This chapter demonstrates a novel method to brighten the dark exciton emission in monolayer TMDs by utilizing the plasmonic gap mode in a metallic particle-on-film system at room temperature. In comparison with tip on film cavity, the resonance feather of such gap mode greatly enhances the PL emission of dark excitons, which makes it detectable even by commercial confocal microscopy. High valley polarization of bright exciton in TMDC has been utilized to distinguish between bright and dark excitons. By changing the detected polarization angle from 0 degree to 90 degree, an obvious peak shift occurs indicating the existence of emission of dark excitons. To further analyze the bright and dark excitons in the PL spectra, a simplified model of superposing polarized and unpolarized Lorentz emissions have been built to fit all of the experimental data. The fitted results show a good agreement with the experimental data verifying the reliability of the model. In addition, the different characteristics (i.e. polarization dependence, intensity and peak width) of bright and dark excitons can be directly examined by applying this model. The PL arises from both bright and dark excitons can be observed through this method and by controlling the detected polarization angle, the proportion of bright and dark excitons in PL can be controlled. The collected PL signal from this method could contain more information about the fine structure of the energy levels of the TMD monolayers and find potential applications in plexciton systems, optoelectronic devices, quantum communications, etc.

Chapter 5 Conclusions and outlooks

5.1 Conclusions

This thesis reports studies on 2D TMDs, especially WS_2. The whole thesis focuses on two topics. One is the comparison of the optical and vibrational properties of 2D WS_2 prepared by two different methods and the other is an approach to detect the dark excitons under room temperature.

For the first topic, the optical and vibrational properties of thin WS_2 flakes prepared by CVD and ME methods have been comprehensively compared and studied. The differential reflectance measurements of these two samples show that the quality of the CVD-grown sample is comparable to that of the ME-prepared sample. However, the PL measurements of two samples indicate that structural defects existing in the CVD-grown sample could affect the PL efficiency. In addition, the polarization-resolved photoluminescence imaging and spectroscopy reveal dramatic differences in the two sets of samples because of their high sensitivity to crystal structural symmetry. Different from the optical properties, the peak positions of Raman modes for the samples prepared by both methods show almost no difference. In addition, the nonlinear optical response of CVD-grown samples, especially second-harmonic generation, seems stronger than that of ME-prepared samples because the crystal structure of CVD-grown bilayer WS_2 is not an ideal central symmetric structure due to the existence of polycrystalline domains and structural dislocations. This provides the promise of

using CVD-grown bilayer TMDs for nonlinear optoelectronic devices, such as bio-imaging sensors.

The second topic demonstrates a novel approach to brighten the emission of dark excitons in TMD monolayers (especially WS_2) by using the plasmonic gap mode in a metallic particle-on-film system under room temperature. Different from a previous work using tip on film cavities, the resonance feather of the plasmonic gap mode in this thesis greatly enhances the PL emission of dark excitons. This enhancement makes it possible for detection by commercial confocal microscopy. By changing the detected polarization angle from 0 degree to 90 degrees, an obvious peak shift occurs, which can indicate the existence of emission from dark excitons. To further analyze the reasons for peak shift, a model was established to fit all the experimental results. The model is based on the different detection-linear-polarization dependence of the PL emission from dark and bright excitons and the fitted results show a good agreement with the experimental data, which can indicate the reliability of the model. In addition, the different characteristics (i.e. polarization dependence, intensity and peak width) of bright and dark excitons can be directly observed by analyzing the fitting results from this model. The PL arises from both bright and dark excitons can be observed through this method and the proportion of bright and dark excitons in PL can be controlled by changing the detected linear polarization angle. The detected dark excitons from this method could provide potential applications in plexciton systems, optoelectronic devices, quantum

communications, etc.

5.2 Outlooks

The results shown in this thesis provide a comprehensive comparison study about thin TMD films synthesized by CVD and ME methods and demonstrate a novel approach to detect the emission of dark excitons under room temperature with commercial confocal microscopy system. However, the study on the synthesis methods and dark excitons in TMDs is still quite attractive. For the future work, there are several topics worth to be investigated.

The first topic is about the synthesis methods of thin TMD films. although it is generally agreed that the ME-prepared samples have higher quality than CVD-grown ones, which is also examined in this thesis, CVD method still have its importance which cannot be replaced by the ME method. For example, the shape of CVD-grown samples is controllable and the sample sizes of CVD-grown thin TMD flakes are always quite large, which makes the characterizations more convenient. Therefore, future works should focus more on how to improve the quality of the CVD-grown samples. Besides, several techniques such as high-resolution transmitted electron microscopy (TEM) measurements need to be carried out for studies of structural defects and based on these measurements, further studies on how to ‘fix’ the defects also deserved to be explored.

The second one is about the detection of the PL emission of dark excitons.

This thesis provides a simple and novel approach to detect the radiation of the dark excitons under room temperature. However, the emission from dark and bright excitons is too difficult to be distinguished. Even though the different characteristics could be observed from the fitting result, the direct observation of the radiation from dark excitons is not achieved in this work. Therefore, the characterization methods to directly detect the emission from only dark excitons deserve to be explored in the future.

At last, this thesis studies the plasmon-exciton coupling effects through WS_2 monolayers sandwiched into the metal-film-coupled nanocavities. This work mainly focuses on the PL emissions of dark excitons enhanced by this nanostructure. However, other optical properties induced from the plasmon-exciton coupling effects are also deserved to be explored. For example, the study about whether the metal-film-coupled nanocavities can enhance the SHG response of TMDs is quite fascinating.

Reference

(1) Low, T.; Chaves, A.; Caldwell, J. D.; Kumar, A.; Fang, N. X.; Avouris, P.; Heinz, T. F.; Guinea, F.; Martin-Moreno, L.; Koppens, F. Polaritons in Layered Two-Dimensional Materials. *Nat. Mater.* **2017**, *16* (2), 182–194.

(2) Butler, S. Z.; Hollen, S. M.; Cao, L.; Cui, Y.; Gupta, J. A.; Gutiérrez, H. R.; Heinz, T. F.; Hong, S. S.; Huang, J.; Ismach, A. F.; et al. Progress, Challenges, and Opportunities in Two-Dimensional Materials beyond Graphene. *ACS Nano* **2013**, *7* (4), 2898–2926.

(3) Bhimanapati, G. R.; Lin, Z.; Meunier, V.; Jung, Y.; Cha, J.; Das, S.; Xiao, D.; Son, Y.; Strano, M. S.; Cooper, V. R.; et al. Recent Advances in Two-Dimensional Materials beyond Graphene. *ACS Nano* **2015**, *9* (12), 11509–11539.

(4) Radisavljevic, B.; Radenovic, A.; Brivio, J.; Giacometti, V.; Kis, A. Single-Layer MoS2 Transistors. *Nat. Nanotechnol.* **2011**, *6* (3), 147–150.

(5) Lembke, D.; Kis, A. Breakdown of High-Performance Monolayer MoS2 Transistors. *ACS Nano* **2012**, *6* (11), 10070–10075.

(6) Liu, G.-B.; Xiao, D.; Yao, Y.; Xu, X.; Yao, W. Electronic Structures and Theoretical Modelling of Two-Dimensional Group-VIB Transition Metal Dichalcogenides. *Chem. Soc. Rev.* **2015**, *44* (9), 2643–2663.

(7) Kutorasinski, K.; Wiendlocha, B.; Kaprzyk, S.; Tobola, J. Electronic Structure and Thermoelectric Properties of N- and p-Type SnSe from First

Principles Calculations. *Phys. Rev. B* **2015**, *91* (20), 205201.

(8) Mattheiss, L. F. Band Structures of Transition Metal Dichalcogenide Layer Compounds. *Phys. Rev. B* **1973**, *8* (8), 3719–3739.

(9) Boeker, T.; Severin, R.; Mueller, A.; Janowitz, C.; Manzke, R.; Voss, D.; Krueger, P.; Mazur, A.; Pollmann, J. Band Structure of MoS_2, MoSe_2, and Alpha-MoTe_2: Angle-Resolved Photoelectron Spectroscopy and Ab-Initio Calculations. *Phys. Rev. B* **2001**, *64* (23), 235305.

(10) Zhao, W.; Ghorannevis, Z.; Chu, L.; Toh, M.; Kloc, C.; Tan, P.-H.; Eda, G. Evolution of Electronic Structure in Atomically Thin Sheets of WS_2 and WSe_2. *ACS Nano* **2013**, *7* (1), 791–797.

(11) Das, S.; Robinson, J. A.; Dubey, M.; Terrones, H.; Terrones, M. Beyond Graphene: Progress in Novel Two-Dimensional Materials and van Der Waals Solids. *Annu. Rev. Mater. Res.* **2015**, *45* (1), 1–27.

(12) Yang, W.; Shang, J.; Wang, J.; Shen, X.; Cao, B.; Peimyoo, N.; Zou, C.; Chen, Y.; Wang, Y.; Cong, C.; et al. Electrically Tunable Valley-Light Emitting Diode (VLED) Based on CVD-Grown Monolayer WS2. *Nano Lett.* **2016**, *16* (3), 1560–1567.

(13) McCreary, K. M.; Hanbicki, A. T.; Jernigan, G. G.; Culbertson, J. C.; Jonker, B. T. Synthesis of Large-Area WS2 Monolayers with Exceptional Photoluminescence. *Sci. Rep.* **2016**, *6* (August 2015), 19159.

(14) Manzeli, S.; Ovchinnikov, D.; Pasquier, D.; Yazyev, O. V.; Kis, A. 2D Transition Metal Dichalcogenides. *Nat. Rev. Mater.* **2017**, *2* (8), 17033.

(15) Toh, R. J.; Sofer, Z.; Luxa, J.; Sedmidubský, D.; Pumera, M. 3R Phase of MoS $_2$ and WS $_2$ Outperforms the Corresponding 2H Phase for Hydrogen Evolution. *Chem. Commun.* **2017**, *53* (21), 3054–3057.

(16) Jiang, T.; Liu, H.; Huang, D.; Zhang, S.; Li, Y.; Gong, X.; Shen, Y. R.; Liu, W. T.; Wu, S. Valley and Band Structure Engineering of Folded MoS 2 Bilayers. *Nat. Nanotechnol.* **2014**, *9* (10), 825–829.

(17) Suzuki, R.; Sakano, M.; Zhang, Y. J.; Akashi, R.; Morikawa, D.; Harasawa, A.; Yaji, K.; Kuroda, K.; Miyamoto, K.; Okuda, T.; et al. Valley-Dependent Spin Polarization in Bulk MoS 2 with Broken Inversion Symmetry. *Nat. Nanotechnol.* **2014**, *9* (8), 611–617.

(18) Jiang, T.; Liu, H.; Huang, D.; Zhang, S.; Li, Y.; Gong, X.; Shen, Y. R.; Liu, W. T.; Wu, S. Valley and Band Structure Engineering of Folded MoS 2 Bilayers. *Nat. Nanotechnol.* **2014**, *9* (10), 825–829.

(19) Chance, K. V.; Spurr, R. J. D. Ring Effect Studies: Rayleigh Scattering, Including Molecular Parameters for Rotational Raman Scattering, and the Fraunhofer Spectrum. *Appl. Opt.* **1997**, *36* (21), 5224.

(20) Zhang, X.; Qiao, X.-F.; Shi, W.; Wu, J.-B.; Jiang, D.-S.; Tan, P.-H. Phonon and Raman Scattering of Two-Dimensional Transition Metal Dichalcogenides from Monolayer, Multilayer to Bulk Material. *Chem. Soc. Rev.* **2015**, *44* (9), 2757–2785.

(21) Molina-Sánchez, A.; Wirtz, L. Phonons in Single-Layer and Few-Layer MoS2 and WS2. *Phys. Rev. B - Condens. Matter Mater. Phys.* **2011**, *84*

(15), 1–8.

(22) Wakabayashi, N.; Smith, H. G.; Nicklow, R. M. Lattice Dynamics of Hexagonal MoS2 Studied by Neutron Scattering. *Phys. Rev. B* **1975**, *12* (2), 659–663.

(23) Wolfram, G.; Jaswal, S. S.; Sharma, T. P. Raman Scattering Due to Localized Lattice Vibrations in LiD : H. *Phys. Rev. Lett.* **1972**, *29* (3), 160–162.

(24) Lucovsky, G.; White, R. M.; Benda, J. A.; Revelli, J. F. Infrared-Reflectance Spectra of Layered Group-IV and Group-VI Transition-Metal Dichalcogenides. *Phys. Rev. B* **1973**, *7* (8), 3859–3870.

(25) Verble, J. L.; Wieting, T. J. Lattice Mode Degeneracy in MoS2 and Other Layer Compounds. *Phys. Rev. Lett.* **1970**, *25* (6), 362–365.

(26) Berkdemir, A.; Gutiérrez, H. R.; Botello-Méndez, A. R.; Perea-López, N.; Elías, A. L.; Chia, C.-I.; Wang, B.; Crespi, V. H.; López-Urías, F.; Charlier, J.-C.; et al. Identification of Individual and Few Layers of WS2 Using Raman Spectroscopy. *Sci. Rep.* **2013**, *3*, 1755.

(27) Li, T.; Galli, G. Electronic Properties of MoS 2 Nanoparticles. *J. Phys. Chem. C* **2007**, *111* (44), 16192–16196.

(28) Voß, D.; Krüger, P.; Mazur, A.; Pollmann, J. Atomic and Electronic Structure of WSe2 from Ab Initio Theory: Bulk Crystal and Thin Film Systems. *Phys. Rev. B* **1999**, *60* (20), 14311–14317.

(29) Splendiani, A.; Sun, L.; Zhang, Y.; Li, T.; Kim, J.; Chim, C. Y.; Galli, G.;

Wang, F. Emerging Photoluminescence in Monolayer MoS2. *Nano Lett.* **2010**, *10* (4), 1271–1275.

(30) Radisavljevic, B.; Radenovic, A.; Brivio, J.; Giacometti, V.; Kis, A. Single-Layer MoS2transistors. *Nat. Nanotechnol.* **2011**, *6* (3), 147–150.

(31) Ugeda, M. M.; Bradley, A. J.; Shi, S. F.; Da Jornada, F. H.; Zhang, Y.; Qiu, D. Y.; Ruan, W.; Mo, S. K.; Hussain, Z.; Shen, Z. X.; et al. Giant Bandgap Renormalization and Excitonic Effects in a Monolayer Transition Metal Dichalcogenide Semiconductor. *Nat. Mater.* **2014**, *13* (12), 1091–1095.

(32) Jones, A. M.; Yu, H.; Ghimire, N. J.; Wu, S.; Aivazian, G.; Ross, J. S.; Zhao, B.; Yan, J.; Mandrus, D. G.; Xiao, D.; et al. Optical Generation of Excitonic Valley Coherence in Monolayer WSe2. *Nat. Nanotechnol.* **2013**, *8* (9), 634–638.

(33) Vega-Mayoral, V.; Backes, C.; Hanlon, D.; Khan, U.; Gholamvand, Z.; O'Brien, M.; Duesberg, G. S.; Gadermaier, C.; Coleman, J. N. Photoluminescence from Liquid-Exfoliated WS2 Monomers in Poly(Vinyl Alcohol) Polymer Composites. *Adv. Funct. Mater.* **2016**, *26* (7), 1028–1039.

(34) Fontana, M.; Deppe, T.; Boyd, A. K.; Rinzan, M.; Liu, A. Y.; Paranjape, M.; Barbara, P. Electron-Hole Transport and Photovoltaic Effect in Gated MoS2 Schottky Junctions. *Sci. Rep.* **2013**, *3*.

(35) Mak, K. F.; Lee, C.; Hone, J.; Shan, J.; Heinz, T. F. Atomically Thin

MoS2: A New Direct-Gap Semiconductor. *Phys. Rev. Lett.* **2010**, *105* (13), 2–5.

(36) Ugeda, M. M.; Bradley, A. J.; Shi, S. F.; Da Jornada, F. H.; Zhang, Y.; Qiu, D. Y.; Ruan, W.; Mo, S. K.; Hussain, Z.; Shen, Z. X.; et al. Giant Bandgap Renormalization and Excitonic Effects in a Monolayer Transition Metal Dichalcogenide Semiconductor. *Nat. Mater.* **2014**, *13* (12), 1091–1095.

(37) Boyd, R. *Nonlinear Optics*; Academic Press, 2008.

(38) Sutherland, R. L.; McLean, D. G.; Kirkpatrick, S. *Handbook of Nonlinear Optics.*; Marcel Dekker, 2003.

(39) Pantazis, P.; Maloney, J.; Wu, D.; Fraser, S. E. Second Harmonic Generating (SHG) Nanoprobes for in Vivo Imaging. *Proc. Natl. Acad. Sci.* **2010**, *107* (33), 14535–14540.

(40) Pantazis, P.; Maloney, J.; Wu, D.; Fraser, S. E. Second Harmonic Generating (SHG) Nanoprobes for in Vivo Imaging. *Proc. Natl. Acad. Sci.* **2010**, *107* (33), 14535–14540.

(41) Franken, P. A.; Hill, A. E.; Peters, C. W.; Weinreich, G. Generation of Optical Harmonics. *Phys. Rev. Lett.* **1961**, *7* (4), 118–119.

(42) Bloembergen, N.; Pershan, P. S. Light Waves at the Boundary of Nonlinear Media. *Phys. Rev.* **1962**, *128* (2), 606–622.

(43) Campagnola, P. J.; Loew, L. M. Second-Harmonic Imaging Microscopy for Visualizing Biomolecular Arrays in Cells, Tissues and Organisms. *Nat.*

Biotechnol. **2003**, *21* (11), 1356–1360.

(44) Lin, X.; Liu, Y.; Wang, K.; Wei, C.; Zhang, W.; Yan, Y.; Li, Y. J.; Yao, J.; Zhao, Y. S. Two-Dimensional Pyramid-like WS2Layered Structures for Highly Efficient Edge Second-Harmonic Generation. *ACS Nano* **2018**, *12* (1), 689–696.

(45) Radisavljevic, B.; Radenovic, A.; Brivio, J.; Giacometti, V.; Kis, A. Single-Layer MoS2transistors. *Nat. Nanotechnol.* **2011**, *6* (3), 147–150.

(46) Elias, D. C.; Nair, R. R.; Mohiuddin, T. M. G.; Morozov, S. V.; Blake, P.; Halsall, M. P.; Ferrari, A. C.; Boukhvalov, D. W.; Katsnelson, M. I.; Geim, A. K.; et al. Control of Graphene's Properties by Reversible Hydrogenation: Evidence for Graphane. *Science (80-.).* **2009**, *323* (5914), 610–613.

(47) Yu, W. J.; Li, Z.; Zhou, H.; Chen, Y.; Wang, Y.; Huang, Y.; Duan, X. Vertically Stacked Multi-Heterostructures of Layered Materials for Logic Transistors and Complementary Inverters. *Nat. Mater.* **2013**, *12* (3), 246–252.

(48) Lopez-Sanchez, O.; Alarcon Llado, E.; Koman, V.; Fontcuberta I Morral, A.; Radenovic, A.; Kis, A. Light Generation and Harvesting in a van Der Waals Heterostructure. *ACS Nano* **2014**, *8* (3), 3042–3048.

(49) Lee, C. H.; Lee, G. H.; Van Der Zande, A. M.; Chen, W.; Li, Y.; Han, M.; Cui, X.; Arefe, G.; Nuckolls, C.; Heinz, T. F.; et al. Atomically Thin P-n Junctions with van Der Waals Heterointerfaces. *Nat. Nanotechnol.* **2014**, *9*

(9), 676–681.

(50) Cheng, R.; Li, D.; Zhou, H.; Wang, C.; Yin, A.; Jiang, S.; Liu, Y.; Chen, Y.; Huang, Y.; Duan, X. Electroluminescence and Photocurrent Generation from Atomically Sharp WSe2/MoS2heterojunction p-n Diodes. *Nano Lett.* **2014**, *14* (10), 5590–5597.

(51) Baugher, B. W. H.; Churchill, H. O. H.; Yang, Y.; Jarillo-Herrero, P. Optoelectronic Devices Based on Electrically Tunable P-n Diodes in a Monolayer Dichalcogenide. *Nat. Nanotechnol.* **2014**, *9* (4), 262–267.

(52) Pospischil, A.; Furchi, M. M.; Mueller, T. Solar-Energy Conversion and Light Emission in an Atomic Monolayer p-n Diode. *Nat. Nanotechnol.* **2014**, *9* (4), 257–261.

(53) Splendiani, A.; Sun, L.; Zhang, Y.; Li, T.; Kim, J.; Chim, C. Y.; Galli, G.; Wang, F. Emerging Photoluminescence in Monolayer MoS2. *Nano Lett.* **2010**, *10* (4), 1271–1275.

(54) Yu, L.; Lee, Y. H.; Ling, X.; Santos, E. J. G.; Shin, Y. C.; Lin, Y.; Dubey, M.; Kaxiras, E.; Kong, J.; Wang, H.; et al. Graphene/MoS2 Hybrid Technology for Large-Scale Two-Dimensional Electronics. *Nano Lett.* **2014**, *14* (6), 3055–3063.

(55) Haigh, S. J.; Gholinia, A.; Jalil, R.; Romani, S.; Britnell, L.; Elias, D. C.; Novoselov, K. S.; Ponomarenko, L. A.; Geim, A. K.; Gorbachev, R. Cross-Sectional Imaging of Individual Layers and Buried Interfaces of Graphene-Based Heterostructures and Superlattices. *Nat. Mater.* **2012**, *11*

(9), 764–767.

(56) Fang, H.; Battaglia, C.; Carraro, C.; Nemsak, S.; Ozdol, B.; Kang, J. S.; Bechtel, H. A.; Desai, S. B.; Kronast, F.; Unal, A. A.; et al. Strong Interlayer Coupling in van Der Waals Heterostructures Built from Single-Layer Chalcogenides. *Proc. Natl. Acad. Sci.* **2014**, *111* (17), 6198–6202.

(57) Fang, H.; Battaglia, C.; Carraro, C.; Nemsak, S.; Ozdol, B.; Kang, J. S.; Bechtel, H. A.; Desai, S. B.; Kronast, F.; Unal, A. A.; et al. Strong Interlayer Coupling in van Der Waals Heterostructures Built from Single-Layer Chalcogenides. *Proc. Natl. Acad. Sci.* **2014**, *111* (17), 6198–6202.

(58) Jiang, N.; Zhuo, X.; Wang, J. Active Plasmonics: Principles, Structures, and Applications. *Chem. Rev.* **2018**, *118* (6), 3054–3099.

(59) Curto, A. G.; Volpe, G.; Taminiau, T. H.; Kreuzer, M. P.; Quidant, R.; Van Hulst, N. F. Unidirectional Emission of a Quantum Dot Coupled to a Nanoantenna. *Science (80-.).* **2010**, *329* (5994), 930–933.

(60) Dregely, D.; Taubert, R.; Dorfmüller, J.; Vogelgesang, R.; Kern, K.; Giessen, H. 3D Optical Yagi-Uda Nanoantenna Array. *Nat. Commun.* **2011**, *2* (1), 267.

(61) Wang, F.; Li, C.; Chen, H.; Jiang, R.; Sun, L. D.; Li, Q.; Wang, J.; Yu, J. C.; Yan, C. H. Plasmonic Harvesting of Light Energy for Suzuki Coupling Reactions. *J. Am. Chem. Soc.* **2013**, *135* (15), 5588–5601.

(62) Xiao, M.; Jiang, R.; Wang, F.; Fang, C.; Wang, J.; Yu, J. C. Plasmon-Enhanced Chemical Reactions. *J. Mater. Chem. A* **2013**, *1* (19), 5790.

(63) Warren, S. C.; Thimsen, E. Plasmonic Solar Water Splitting. *Energy Environ. Sci.* **2012**, *5* (1), 5133–5146.

(64) Park, J.-H.; von Maltzahn, G.; Xu, M. J.; Fogal, V.; Kotamraju, V. R.; Ruoslahti, E.; Bhatia, S. N.; Sailor, M. J. Cooperative Nanomaterial System to Sensitize, Target, and Treat Tumors. *Proc. Natl. Acad. Sci.* **2010**, *107* (3), 981–986.

(65) Yang, X.; Liu, X.; Liu, Z.; Pu, F.; Ren, J.; Qu, X. Near-Infrared Light-Triggered, Targeted Drug Delivery to Cancer Cells by Aptamer Gated Nanovehicles. *Adv. Mater.* **2012**, *24* (21), 2890–2895.

(66) Tokel, O.; Inci, F.; Demirci, U. Advances in Plasmonic Technologies for Point of Care Applications. *Chem. Rev.* **2014**, *114* (11), 5728–5752.

(67) Bethe, H. A. Theory of Diffraction by Small Holes. *Phys. Rev.* **1944**, *66* (7–8), 163–182.

(68) Roberts, A. Electromagnetic Theory of Diffraction by a Circular Aperture in a Thick, Perfectly Conducting Screen. *J. Opt. Soc. Am. A* **1987**, *4* (10), 1970.

(69) Kneipp, K.; Moskovits, M.; Kneipp, H. *Surface-Enhanced Raman Scattering*; Kneipp, K., Moskovits, M., Kneipp, H., Eds.; Topics in Applied Physics; Springer Berlin Heidelberg, 2006; Vol. 103.

(70) Aoki, T. Photoluminescence Spectroscopy. In *Characterization of Materials*; Kaufmann, E. N., Ed.; John Wiley & Sons, Inc.: Hoboken, NJ, USA, 2012.

(71) Raether, H. *Surface Plasmons on Smooth and Rough Surfaces and on Gratings*; Springer Tracts in Modern Physics; Springer Berlin Heidelberg, 1988; Vol. 111.

(72) Li, J. F.; Huang, Y. F.; Ding, Y.; Yang, Z. L.; Li, S. B.; Zhou, X. S.; Fan, F. R.; Zhang, W.; Zhou, Z. Y.; Wu, D. Y.; et al. Shell-Isolated Nanoparticle-Enhanced Raman Spectroscopy. *Nature* **2010**, *464* (7287), 392–395.

(73) Qian, X.-M.; Nie, S. M. Single-Molecule and Single-Nanoparticle SERS: From Fundamental Mechanisms to Biomedical Applications. *Chem. Soc. Rev.* **2008**, *37* (5), 912–920.

(74) Nie, S. Probing Single Molecules and Single Nanoparticles by Surface-Enhanced Raman Scattering. *Science (80-.).* **1997**, *275* (5303), 1102–1106.

(75) Huang, X.; Jain, P. K.; El-Sayed, I. H.; El-Sayed, M. A. Plasmonic Photothermal Therapy (PPTT) Using Gold Nanoparticles. *Lasers Med. Sci.* **2008**, *23* (3), 217–228.

(76) Huang, X.; El-Sayed, I. H.; Qian, W.; El-Sayed, M. A. Cancer Cell Imaging and Photothermal Therapy in the Near-Infrared Region by Using Gold Nanorods. *J. Am. Chem. Soc.* **2006**, *128* (6), 2115–2120.

(77) Qian, X.; Peng, X.-H.; Ansari, D. O.; Yin-Goen, Q.; Chen, G. Z.; Shin, D. M.; Yang, L.; Young, A. N.; Wang, M. D.; Nie, S. In Vivo Tumor Targeting and Spectroscopic Detection with Surface-Enhanced Raman Nanoparticle Tags. *Nat. Biotechnol.* **2008**, *26* (1), 83–90.

(78) Atwater, H. A.; Polman, A. Plasmonics for Improved Photovoltaic Devices. *Nat. Mater.* **2010**, *9* (3), 205–213.

(79) Clavero, C. Plasmon-Induced Hot-Electron Generation at Nanoparticle/Metal-Oxide Interfaces for Photovoltaic and Photocatalytic Devices. *Nat. Photonics* **2014**, *8* (2), 95–103.

(80) Furube, A.; Du, L.; Hara, K.; Katoh, R.; Tachiya, M. Ultrafast Plasmon-Induced Electron Transfer from Gold Nanodots into TiO2 Nanoparticles. *J. Am. Chem. Soc.* **2007**, *129* (48), 14852–14853.

(81) Willets, K. A.; Van Duyne, R. P. Localized Surface Plasmon Resonance Spectroscopy and Sensing. *Annu. Rev. Phys. Chem.* **2007**, *58* (1), 267–297.

(82) Maier, S. A. *Plasmonics: Fundamentals and Applications*; Springer US: Boston, MA, 2007.

(83) Estroff, A.; Smith, B. W. Tuning Metamaterials for Applications at DUV Wavelengths. *Int. J. Opt.* **2012**, *2012*, 1–7.

(84) Njoki, P. N.; Lim, I.-I. S.; Mott, D.; Park, H.-Y.; Khan, B.; Mishra, S.; Sujakumar, R.; Luo, J.; Zhong, C.-J. Size Correlation of Optical and Spectroscopic Properties for Gold Nanoparticles. *J. Phys. Chem. C* **2007**,

111 (40), 14664–14669.

(85) Hao, F.; Nordlander, P.; Sonnefraud, Y.; Van Dorpe, P.; Maier, S. A. Tunability of Subradiant Dipolar and Fano-Type Plasmon Resonances in Metallic Ring/Disk Cavities: Implications for Nanoscale Optical Sensing. *ACS Nano* **2009**, *3* (3), 643–652.

(86) Zhou, W.; Odom, T. W. Tunable Subradiant Lattice Plasmons by Out-of-Plane Dipolar Interactions. *Nat. Nanotechnol.* **2011**, *6* (7), 423–427.

(87) Fan, J. A.; Wu, C.; Bao, K.; Bao, J.; Bardhan, R.; Halas, N. J.; Manoharan, V. N.; Nordlander, P.; Shvets, G.; Capasso, F. Self-Assembled Plasmonic Nanoparticle Clusters. *Science (80-.).* **2010**, *328* (5982), 1135–1138.

(88) Fan, J. A.; Wu, C.; Bao, K.; Bao, J.; Bardhan, R.; Halas, N. J.; Manoharan, V. N.; Nordlander, P.; Shvets, G.; Capasso, F. Self-Assembled Plasmonic Nanoparticle Clusters. *Science (80-.).* **2010**, *328* (5982), 1135–1138.

(89) Wadell, C.; Syrenova, S.; Langhammer, C. Plasmonic Hydrogen Sensing with Nanostructured Metal Hydrides. *ACS Nano*. 2014, pp 11925–11940.

(90) Ou, F. S.; Hu, M.; Naumov, I.; Kim, A.; Wu, W.; Bratkovsky, A. M.; Li, X.; Williams, R. S.; Li, Z. Hot-Spot Engineering in Polygonal Nanofinger Assemblies for Surface Enhanced Raman Spectroscopy. *Nano Lett.* **2011**, *11* (6), 2538–2542.

(91) Feuz, L.; Jonsson, M. P.; Höök, F. Material-Selective Surface Chemistry for Nanoplasmonic Sensors: Optimizing Sensitivity and Controlling

Binding to Local Hot Spots. *Nano Lett.* **2012**, *12* (2), 873–879.

(92) Wang, H.; Wu, Y.; Lassiter, B.; Nehl, C. L.; Hafner, J. H.; Nordlander, P.; Halas, N. J. Symmetry Breaking in Individual Plasmonic Nanoparticles. *Proc. Natl. Acad. Sci. U. S. A.* **2006**, *103* (29), 10856–10860.

(93) Bachelier, G.; Russier-Antoine, I.; Benichou, E.; Jonin, C.; Del Fatti, N.; Vallée, F.; Brevet, P. F. Fano Profiles Induced by Near-Field Coupling in Heterogeneous Dimers of Gold and Silver Nanoparticles. *Phys. Rev. Lett.* **2008**, *101* (19).

(94) Fedotov, V. A.; Rose, M.; Prosvirnin, S. L.; Papasimakis, N.; Zheludev, N. I. Sharp Trapped-Mode Resonances in Planar Metamaterials with a Broken Structural Symmetry. *Phys. Rev. Lett.* **2007**, *99* (14).

(95) Zhang, S.; Genov, D. A.; Wang, Y.; Liu, M.; Zhang, X. Plasmon-Induced Transparency in Metamaterials. *Phys. Rev. Lett.* **2008**, *101* (4).

(96) Lévêque, G.; Martin, O. J. F. Optical Interactions in a Plasmonic Particle Coupled to a Metallic Film. *Opt. Express* **2006**, *14* (21), 9971–9981.

(97) Lumdee, C.; Yun, B.; Kik, P. G. Effect of Surface Roughness on Substrate-Tuned Gold Nanoparticle Gap Plasmon Resonances. *Nanoscale* **2015**, *7* (9), 4250–4255.

(98) Schertz, F.; Schmelzeisen, M.; Mohammadi, R.; Kreiter, M.; Elmers, H. J.; Schönhense, G. Near Field of Strongly Coupled Plasmons: Uncovering Dark Modes. *Nano Lett.* **2012**, *12* (4), 1885–1890.

(99) Lassiter, J. B.; McGuire, F.; Mock, J. J.; Ciracì, C.; Hill, R. T.; Wiley, B.

J.; Chilkoti, A.; Smith, D. R. Plasmonic Waveguide Modes of Film-Coupled Metallic Nanocubes. *Nano Lett.* **2013**, *13* (12), 5866–5872.

(100) Lei, D. Y.; Fernández-Domínguez, A. I.; Sonnefraud, Y.; Appavoo, K.; Haglund, R. F.; Pendry, J. B.; Maier, S. a. Revealing Plasmonic Gap Modes in Particle-on-Film Systems Using Dark-Field Spectroscopy. *ACS Nano* **2012**, *6* (2), 1380–1386.

(101) Li, G.-C.; Zhang, Y.-L.; Lei, D. Y. Hybrid Plasmonic Gap Modes in Metal Film-Coupled Dimers and Their Physical Origins Revealed by Polarization Resolved Dark Field Spectroscopy. *Nanoscale* **2016**, *8* (13), 7119–7126.

(102) Mock, J. J.; Hill, R. T.; Degiron, A.; Zauscher, S.; Chilkoti, A.; Smith, D. R. Distance-Dependent Plasmon Resonant Coupling between a Gold Nanoparticle and Gold Film. *Nano Lett.* **2008**, *8* (8), 2245–2252.

(103) Mubeen, S.; Zhang, S.; Kim, N.; Lee, S.; Krämer, S.; Xu, H.; Moskovits, M. Plasmonic Properties of Gold Nanoparticles Separated from a Gold Mirror by an Ultrathin Oxide. *Nano Lett.* **2012**, *12* (4), 2088–2094.

(104) Hill, R. T.; Mock, J. J.; Hucknall, A.; Wolter, S. D.; Jokerst, N. M.; Smith, D. R.; Chilkoti, A. Plasmon Ruler with Angstrom Length Resolution. *ACS Nano* **2012**, *6* (10), 9237–9246.

(105) Ciraci, C.; Hill, R. T.; Mock, J. J.; Urzhumov, Y.; Fernandez-Dominguez, a. I.; Maier, S. a.; Pendry, J. B.; Chilkoti, a.; Smith, D. R. Probing the Ultimate Limits of Plasmonic Enhancement. *Science (80-.).* **2012**, *337*

(6098), 1072–1074.

(106) Hajisalem, G.; Nezami, M. S.; Gordon, R. Probing the Quantum Tunneling Limit of Plasmonic Enhancement by Third Harmonic Generation. *Nano Lett.* **2014**, *14* (11), 6651–6654.

(107) Mertens, J.; Eiden, A. L.; Sigle, D. O.; Huang, F.; Lombardo, A.; Sun, Z.; Sundaram, R. S.; Colli, A.; Tserkezis, C.; Aizpurua, J.; et al. Controlling Subnanometer Gaps in Plasmonic Dimers Using Graphene. *Nano Lett.* **2013**, *13* (11), 5033–5038.

(108) Oulton, R. F.; Sorger, V. J.; Zentgraf, T.; Ma, R.-M.; Gladden, C.; Dai, L.; Bartal, G.; Zhang, X. Plasmon Lasers at Deep Subwavelength Scale. *Nature* **2009**, *461* (7264), 629–632.

(109) Russell, K. J.; Liu, T.-L.; Cui, S.; Hu, E. L. Large Spontaneous Emission Enhancement in Plasmonic Nanocavities. *Nat. Photonics* **2012**, *6* (7), 459–462.

(110) Akselrod, G. M.; Argyropoulos, C.; Hoang, T. B.; Ciracì, C.; Fang, C.; Huang, J.; Smith, D. R.; Mikkelsen, M. H. Probing the Mechanisms of Large Purcell Enhancement in Plasmonic Nanoantennas. *Nat. Photonics* **2014**, *8* (11), 835–840.

(111) Chikkaraddy, R.; De Nijs, B.; Benz, F.; Barrow, S. J.; Scherman, O. A.; Rosta, E.; Demetriadou, A.; Fox, P.; Hess, O.; Baumberg, J. J. Single-Molecule Strong Coupling at Room Temperature in Plasmonic Nanocavities. *Nature* **2016**, *535* (7610), 127–130.

(112) Benz, F.; Schmidt, M. K.; Dreismann, A.; Chikkaraddy, R.; Zhang, Y.; Demetriadou, A.; Carnegie, C.; Ohadi, H.; de Nijs, B.; Esteban, R.; et al. Single-Molecule Optomechanics in “Picocavities.” *Science (80-.).* **2016**, *354* (6313), 726–729.

(113) Wang, G.; Chernikov, A.; Glazov, M. M.; Heinz, T. F.; Marie, X.; Amand, T.; Urbaszek, B. Excitons in Atomically Thin Transition Metal Dichalcogenides. *Rev. Mod. Phys.* **2017**, *90* (2), 021001.

(114) Wang, G.; Chernikov, A.; Glazov, M. M.; Heinz, T. F.; Marie, X.; Amand, T.; Urbaszek, B. Excitons in Atomically Thin Transition Metal Dichalcogenides. *Rev. Mod. Phys.* **2017**, *90* (2), 021001.

(115) Gupalov, S. V.; Ivchenko, E. L.; Kavokin, a. V. Fine Structure of Localized Exciton Levels in Quantum Wells. *J. Exp. Theor. Phys.* **1998**, *86* (2), 388–394.

(116) Yao, W.; Xiao, D.; Niu, Q. Valley-Dependent Optoelectronics from Inversion Symmetry Breaking. *Phys. Rev. B - Condens. Matter Mater. Phys.* **2008**, *77* (23), 235406.

(117) Mak, K. F.; He, K.; Shan, J.; Heinz, T. F. Control of Valley Polarization in Monolayer MoS2 by Optical Helicity. *Nat. Nanotechnol.* **2012**, *7* (8), 494–498.

(118) Yao, W.; Xiao, D.; Niu, Q. Valley-Dependent Optoelectronics from Inversion Symmetry Breaking. *Phys. Rev. B - Condens. Matter Mater. Phys.* **2008**, *77* (23), 235406.

(119) Gong, P.; Yu, H.; Wang, Y.; Yao, W. Optical Selection Rules for Excitonic Rydberg Series in the Massive Dirac Cones of Hexagonal Two-Dimensional Materials. *Phys. Rev. B* **2017**, *95* (12), 125420.

(120) Liu, G. Bin; Shan, W. Y.; Yao, Y.; Yao, W.; Xiao, D. Three-Band Tight-Binding Model for Monolayers of Group-VIB Transition Metal Dichalcogenides. *Phys. Rev. B - Condens. Matter Mater. Phys.* **2013**, *88* (8), 085433.

(121) Rong, Y.; Fan, Y.; Leen Koh, A.; Robertson, A. W.; He, K.; Wang, S.; Tan, H.; Sinclair, R.; Warner, J. H. Controlling Sulphur Precursor Addition for Large Single Crystal Domains of WS2. *Nanoscale* **2014**, *6* (20), 12096–12103.

(122) McDonnell, S. J.; Wallace, R. M. Atomically-Thin Layered Films for Device Applications Based upon 2D TMDC Materials. *Thin Solid Films* **2016**, *616*, 482–501.

(123) Hong, J.; Hu, Z.; Probert, M.; Li, K.; Lv, D.; Yang, X.; Gu, L.; Mao, N.; Feng, Q.; Xie, L.; et al. Exploring Atomic Defects in Molybdenum Disulphide Monolayers. *Nat. Commun.* **2015**, *6*, 6293.

(124) Liu, Z.; Suenaga, K.; Wang, Z.; Shi, Z.; Okunishi, E.; Iijima, S. Identification of Active Atomic Defects in a Monolayered Tungsten Disulphide Nanoribbon. *Nat Commun* **2011**, *2*, 213.

(125) Gao, Y.; Liu, Z.; Sun, D.-M.; Huang, L.; Ma, L.-P.; Yin, L.-C.; Ma, T.; Zhang, Z.; Ma, X.-L.; Peng, L.-M.; et al. Large-Area Synthesis of

High-Quality and Uniform Monolayer WS2 on Reusable Au Foils. *Nat. Commun.* **2015**, *6*, 8569.

(126) Sim, D. M.; Kim, M.; Yim, S.; Choi, M. J.; Choi, J.; Yoo, S.; Jung, Y. S. Controlled Doping of Vacancy-Containing Few-Layer MoS2via Highly Stable Thiol-Based Molecular Chemisorption. *ACS Nano* **2015**, *9* (12), 12115–12123.

(127) Cho, K.; Min, M.; Kim, T. Y.; Jeong, H.; Pak, J.; Kim, J. K.; Jang, J.; Yun, S. J.; Lee, Y. H.; Hong, W. K.; et al. Electrical and Optical Characterization of MoS<inf>2</Inf> with Sulfur Vacancy Passivation by Treatment with Alkanethiol Molecules. *ACS Nano* **2015**, *9* (8), 8044–8053.

(128) Gutiérrez, H. R.; Perea-López, N.; Elías, A. L.; Berkdemir, A.; Wang, B.; Lv, R.; López-Urías, F.; Crespi, V. H.; Terrones, H.; Terrones, M. Extraordinary Room-Temperature Photoluminescence in Triangular WS 2 Monolayers. *Nano Lett.* **2013**, *13* (8), 3447–3454.

(129) Zeng, H.; Liu, G.-B.; Dai, J.; Yan, Y.; Zhu, B.; He, R.; Xie, L.; Xu, S.; Chen, X.; Yao, W.; et al. Optical Signature of Symmetry Variations and Spin-Valley Coupling in Atomically Thin Tungsten Dichalcogenides. *Sci. Rep.* **2013**, *3*, 1608.

(130) Liu, J.; Lo, T. W.; Sun, J.; Yip, C. T.; Lam, C. H.; Lei, D. Y. A Comprehensive Comparison Study on the Vibrational and Optical Properties of CVD-Grown and Mechanically Exfoliated Few-Layered WS

$_2$. *J. Mater. Chem. C* **2017**, *5* (43), 11239–11245.

(131) Berkdemir, A.; Gutiérrez, H. R.; Botello-Méndez, A. R.; Perea-López, N.; Elías, A. L.; Chia, C. I.; Wang, B.; Crespi, V. H.; López-Urías, F.; Charlier, J. C.; et al. Identification of Individual and Few Layers of WS2 Using Raman Spectroscopy. *Sci. Rep.* **2013**, *3* (1), 1755.

(132) Yang, J.; Xu, R.; Pei, J.; Myint, Y. W.; Wang, F.; Wang, Z.; Zhang, S.; Yu, Z.; Lu, Y. Optical Tuning of Exciton and Trion Emissions in Monolayer Phosphorene. *Light Sci. Appl.* **2015**, *4* (7), e312.

(133) Sun, J.; Gu, Y. J.; Lei, D. Y.; Lau, S. P.; Wong, W. T.; Wong, K. Y.; Chan, H. L. W. Mechanistic Understanding of Excitation-Correlated Nonlinear Optical Properties in MoS2Nanosheets and Nanodots: The Role of Exciton Resonance. *ACS Photonics* **2016**, *3* (12), 2434–2444.

(134) Jia, G. Y.; Liu, Y.; Gong, J. Y.; Lei, D. Y.; Wang, D. L.; Huang, Z. X. Excitonic Quantum Confinement Modified Optical Conductivity of Monolayer and Few-Layered MoS $_2$. *J. Mater. Chem. C* **2016**, *4* (37), 8822–8828.

(135) Xiao, D.; Liu, G. Bin; Feng, W.; Xu, X.; Yao, W. Coupled Spin and Valley Physics in Monolayers of MoS 2 and Other Group-VI Dichalcogenides. *Phys. Rev. Lett.* **2012**, *108* (19), 1–5.

(136) Zeng, H.; Cui, X. An Optical Spectroscopic Study on Two-Dimensional Group-VI Transition Metal Dichalcogenides. *Chem. Soc. Rev.* **2015**, *44* (9), 2629–2642.

(137) Ahuja, U.; Dashora, A.; Tiwari, H.; Kothari, D. C.; Venugopalan, K. Electronic and Optical Properties of MoS2-WS2multi-Layers: First Principles Study. *Comput. Mater. Sci.* **2014**, *92*, 451–456.

(138) Zeng, H.; Liu, G.-B.; Dai, J.; Yan, Y.; Zhu, B.; He, R.; Xie, L.; Xu, S.; Chen, X.; Yao, W.; et al. Optical Signature of Symmetry Variations and Spin-Valley Coupling in Atomically Thin Tungsten Dichalcogenides. *Sci. Rep.* **2013**, *3* (4), 1608.

(139) Zhu, B.; Zeng, H.; Dai, J.; Gong, Z.; Cui, X. Anomalously Robust Valley Polarization and Valley Coherence in Bilayer WS2. *Proc. Natl. Acad. Sci.* **2014**, *111* (32), 11606–11611.

(140) Ye, Y.; Xiao, J.; Wang, H.; Ye, Z.; Zhu, H.; Zhao, M.; Wang, Y.; Zhao, J.; Yin, X.; Zhang, X. Electrical Generation and Control of the Valley Carriers in a Monolayer Transition Metal Dichalcogenide. *Nat. Nanotechnol.* **2016**, *11* (7), 598–602.

(141) Nayak, P. K.; Lin, F.-C.; Yeh, C.-H.; Huang, J.-S.; Chiu, P.-W. Robust Room Temperature Valley Polarization in Monolayer and Bilayer WS_2. *Nanoscale* **2016**, *8* (11), 6035–6042.

(142) Xiao, J.; Ye, Z. L.; Wang, Y.; Zhu, H. Y.; Wang, Y.; Zhang, X. Nonlinear Optical Selection Rule Based on Valley-Exciton Locking in Monolayer Ws(2). *Light. Appl.* **2015**, *4* (August), 6.

(143) Trolle, M. L.; Seifert, G.; Pedersen, T. G. Theory of Excitonic Second-Harmonic Generation in Monolayer MoS2. *Phys. Rev. B* -

Condens. Matter Mater. Phys. **2014**, *89* (23), 1–8.

(144) Dadap, J. I.; Shan, J.; Heinz, T. F. Theory of Optical Second-Harmonic Generation from a Sphere of Centrosymmetric Material: Small-Particle Limit. *J. Opt. Soc. Am. B* **2004**, *21* (7), 1328–1347.

(145) Janisch, C.; Wang, Y.; Ma, D.; Mehta, N.; Elías, A. L.; Perea-López, N.; Terrones, M.; Crespi, V.; Liu, Z. Extraordinary Second Harmonic Generation in Tungsten Disulfide Monolayers. *Sci. Rep.* **2014**, *4* (c), 5530.

(146) Zhao, M.; Ye, Z.; Suzuki, R.; Ye, Y.; Zhu, H.; Xiao, J.; Wang, Y.; Iwasa, Y.; Zhang, X. Atomically Phase-Matched Second-Harmonic Generation in a 2D Crystal. *Light Sci. Appl.* **2016**, *5* (8), e16131.

(147) Kumar, N.; Najmaei, S.; Cui, Q.; Ceballos, F.; Ajayan, P. M.; Lou, J.; Zhao, H. Second Harmonic Microscopy of Monolayer MoS2. *Phys. Rev. B - Condens. Matter Mater. Phys.* **2013**, *87* (16), 161403.

(148) Yu, H.; Talukdar, D.; Xu, W.; Khurgin, J. B.; Xiong, Q. Charge-Induced Second-Harmonic Generation in Bilayer WSe<inf>2</Inf>. *Nano Lett.* **2015**, *15* (8), 5653–5657.

(149) Janisch, C.; Mehta, N.; Ma, D.; Elías, A. L.; Perea-López, N.; Terrones, M.; Liu, Z. Ultrashort Optical Pulse Characterization Using WS_2 Monolayers. *Opt. Lett.* **2014**, *39* (2), 383–385.

(150) Yin, X.; Ye, Z.; Chenet, D. A.; Ye, Y.; O'Brien, K.; Hone, J. C.; Zhang, X. Edge Nonlinear Optics on a MoS2 Atomic Monolayer. *Science (80-.).* **2014**, *344* (6183), 488–490.

(151) Wang, Q. H.; Kalantar-Zadeh, K.; Kis, A.; Coleman, J. N.; Strano, M. S. Electronics and Optoelectronics of Two-Dimensional Transition Metal Dichalcogenides. *Nat. Nanotechnol.* **2012**, *7* (11), 699–712.

(152) Sun, J.; Gu, Y. J.; Lei, D. Y.; Lau, S. P.; Wong, W. T.; Wong, K. Y.; Chan, H. L. W. Mechanistic Understanding of Excitation-Correlated Nonlinear Optical Properties in MoS2Nanosheets and Nanodots: The Role of Exciton Resonance. *ACS Photonics* **2016**, *3* (12), 2434–2444.

(153) Jia, G. Y.; Liu, Y.; Gong, J. Y.; Lei, D. Y.; Wang, D. L.; Huang, Z. X. Excitonic Quantum Confinement Modified Optical Conductivity of Monolayer and Few-Layered MoS $_2$. *J. Mater. Chem. C* **2016**, *4* (37), 8822–8828.

(154) Koppens, F. H.; Mueller, T.; Avouris, P.; Ferrari, a C.; Vitiello, M. S.; Polini, M. Photodetectors Based on Graphene, Other Two-Dimensional Materials and Hybrid Systems. *Nat Nanotechnol* **2014**, *9* (10), 780–793.

(155) Komider, K.; González, J. W.; Fernández-Rossier, J. Large Spin Splitting in the Conduction Band of Transition Metal Dichalcogenide Monolayers. *Phys. Rev. B - Condens. Matter Mater. Phys.* **2013**, *88* (24), 245436.

(156) Liu, G. Bin; Shan, W. Y.; Yao, Y.; Yao, W.; Xiao, D. Three-Band Tight-Binding Model for Monolayers of Group-VIB Transition Metal Dichalcogenides. *Phys. Rev. B - Condens. Matter Mater. Phys.* **2013**, *88* (8), 085433.

(157) Echeverry, J. P.; Urbaszek, B.; Amand, T.; Marie, X.; Gerber, I. C.

Splitting between Bright and Dark Excitons in Transition Metal Dichalcogenide Monolayers. *Phys. Rev. B* **2016**, *93* (12), 121107.

(158) Echeverry, J. P.; Urbaszek, B.; Amand, T.; Marie, X.; Gerber, I. C. Splitting between Bright and Dark Excitons in Transition Metal Dichalcogenide Monolayers. *Phys. Rev. B* **2016**, *93* (12), 121107.

(159) Zhang, X. X.; You, Y.; Zhao, S. Y. F.; Heinz, T. F. Experimental Evidence for Dark Excitons in Monolayer WSe2. *Phys. Rev. Lett.* **2015**, *115* (25), 1–6.

(160) Slobodeniuk, A. O.; Basko, D. M. Spin-Flip Processes and Radiative Decay of Dark Intravalley Excitons in Transition Metal Dichalcogenide Monolayers. *2D Mater.* **2016**, *3* (3), 035009.

(161) Molas, M. R.; Faugeras, C.; Slobodeniuk, A. O.; Nogajewski, K.; Bartos, M.; Basko, D. M.; Potemski, M. Brightening of Dark Excitons in Monolayers of Semiconducting Transition Metal Dichalcogenides. *2D Mater.* **2017**, *4* (2), 021003.

(162) Smoleński, T.; Kazimierczuk, T.; Goryca, M.; Wojnar, P.; Kossacki, P. Mechanism and Dynamics of Biexciton Formation from a Long-Lived Dark Exciton in a CdTe Quantum Dot. *Phys. Rev. B - Condens. Matter Mater. Phys.* **2015**, *91* (15), 155430.

(163) Park, K. D.; Jiang, T.; Clark, G.; Xu, X.; Raschke, M. B. Radiative Control of Dark Excitons at Room Temperature by Nano-Optical Antenna-Tip Purcell Effect. *Nat. Nanotechnol.* **2018**, *13* (1), 59–64.

(164) Poem, E.; Kodriano, Y.; Tradonsky, C.; Lindner, N. H.; Gerardot, B. D.; Petroff, P. M.; Gershoni, D. Accessing the Dark Exciton with Light. *Nat. Phys.* **2010**, *6* (12), 993–997.

(165) Combescot, M.; Betbeder-Matibet, O.; Combescot, R. Bose-Einstein Condensation in Semiconductors: The Key Role of Dark Excitons. *Phys. Rev. Lett.* **2007**, *99* (17), 176403.

(166) Zhang, X. X.; Cao, T.; Lu, Z.; Lin, Y. C.; Zhang, F.; Wang, Y.; Li, Z.; Hone, J. C.; Robinson, J. A.; Smirnov, D.; et al. Magnetic Brightening and Control of Dark Excitons in Monolayer WSe 2. *Nat. Nanotechnol.* **2017**, *12* (9), 883–888.

(167) Ding, S.-Y.; Yi, J.; Li, J.-F.; Ren, B.; Wu, D.-Y.; Panneerselvam, R.; Tian, Z.-Q. Nanostructure-Based Plasmon-Enhanced Raman Spectroscopy for Surface Analysis of Materials. *Nat. Rev. Mater.* **2016**, *1* (6), 16021.

(168) Ginzburg, P.; Roth, D. J.; Nasir, M. E.; Segovia, P.; Krasavin, A. V.; Levitt, J.; Hirvonen, L. M.; Wells, B.; Suhling, K.; Richards, D.; et al. Spontaneous Emission in Non-Local Materials. *Light Sci. Appl.* **2017**, *6* (6), e16273.

(169) Chen, X.; Park, H. R.; Pelton, M.; Piao, X.; Lindquist, N. C.; Im, H.; Kim, Y. J.; Ahn, J. S.; Ahn, K. J.; Park, N.; et al. Atomic Layer Lithography of Wafer-Scale Nanogap Arrays for Extreme Confinement of Electromagnetic Waves. *Nat. Commun.* **2013**, *4*, 2361.

(170) Li, D.-B.; Sun, X.-J.; Jia, Y.-P.; Stockman, M. I.; Paudel, H. P.; Song, H.;

Jiang, H.; Li, Z.-M. Direct Observation of Localized Surface Plasmon Field Enhancement by Kelvin Probe Force Microscopy. *Light Sci. Appl.* **2017**, *6* (8), e17038.

(171) Chen, X.; Chen, Y. H.; Qin, J.; Zhao, D.; Ding, B.; Blaikie, R. J.; Qiu, M. Mode Modification of Plasmonic Gap Resonances Induced by Strong Coupling with Molecular Excitons. *Nano Lett.* **2017**, *17* (5), 3246–3251.

(172) Liaw, J.-W.; Chen, J.-H.; Chen, C.-S.; Kuo, M.-K. Purcell Effect of Nanoshell Dimer on Single Molecule's Fluorescence. *Opt. Express* **2009**, *17* (16), 13532–13540.

(173) Park, K. D.; Jiang, T.; Clark, G.; Xu, X.; Raschke, M. B. Radiative Control of Dark Excitons at Room Temperature by Nano-Optical Antenna-Tip Purcell Effect. *Nat. Nanotechnol.* **2018**, *13* (1), 59–64.

(174) Zhou, Y.; Scuri, G.; Wild, D. S.; High, A. A.; Dibos, A.; Jauregui, L. A.; Shu, C.; De Greve, K.; Pistunova, K.; Joe, A. Y.; et al. Probing Dark Excitons in Atomically Thin Semiconductors via Near-Field Coupling to Surface Plasmon Polaritons. *Nat. Nanotechnol.* **2017**, *12* (9), 856–860.

(175) Li, G. C.; Zhang, Y. L.; Jiang, J.; Luo, Y.; Lei, D. Y. Metal-Substrate-Mediated Plasmon Hybridization in a Nanoparticle Dimer for Photoluminescence Line-Width Shrinking and Intensity Enhancement. *ACS Nano* **2017**, *11* (3), 3067–3080.

(176) Zhang, Q.; Li, G. C.; Lo, T. W.; Lei, D. Y. Polarization-Resolved Optical Response of Plasmonic Particle-on-Film Nanocavities. *J. Opt. (United*

Kingdom) **2018**, *20* (2), 024010.

(177) Li, G.-C.; Zhang, Y.-L.; Lei, D. Y. Hybrid Plasmonic Gap Modes in Metal Film-Coupled Dimers and Their Physical Origins Revealed by Polarization Resolved Dark Field Spectroscopy. *Nanoscale* **2016**, *8* (13), 7119–7126.

(178) Schubert, E. F.; Göbel, E. O.; Horikoshi, Y.; Ploog, K.; Queisser, H. J. Alloy Broadening in Photoluminescence Spectra of AlxGa1-XAs. *Phys. Rev. B* **1984**, *30* (2), 813–820.

(179) Wang, G.; Robert, C.; Glazov, M. M.; Cadiz, F.; Courtade, E.; Amand, T.; Lagarde, D.; Taniguchi, T.; Watanabe, K.; Urbaszek, B.; et al. In-Plane Propagation of Light in Transition Metal Dichalcogenide Monolayers: Optical Selection Rules. *Phys. Rev. Lett.* **2017**, *119* (4), 047401.